

Optofluidic Devices for Cell, Microparticle, and Nanoparticle Manipulation

Aaron Takami Ohta



Electrical Engineering and Computer Sciences
University of California at Berkeley

Technical Report No. UCB/EECS-2008-148

<http://www.eecs.berkeley.edu/Pubs/TechRpts/2008/EECS-2008-148.html>

December 2, 2008

Copyright 2008, by the author(s).
All rights reserved.

Permission to make digital or hard copies of all or part of this work for personal or classroom use is granted without fee provided that copies are not made or distributed for profit or commercial advantage and that copies bear this notice and the full citation on the first page. To copy otherwise, to republish, to post on servers or to redistribute to lists, requires prior specific permission.

Acknowledgement

My research advisor, Prof. Ming C. Wu, for valuable mentorship and resources. My colleagues Prof. P.-Y. Chiou, M.-C. Tien, H.-Y. Hsu, A. Jamshidi, J.K. Valley, and Dr. S.L. Neale, and my other colleagues in the Integrated Photonics Laboratory.

Collaborators outside of our research group: Drs. A.N.K. Lau and H.L. Phan; Prof. C.-M. Ho's and Prof. C.-J. Kim's groups from UCLA, Prof. P. Yang's, Prof. A. Javey's, and Prof. E. Isacoff's groups at UC Berkeley, and Prof. T. Lue's group from UCSF.

Optofluidic Devices for Cell, Microparticle, and Nanoparticle Manipulation

by

Aaron Takami Ohta

B.S. (University of Hawai'i at Manoa) 2003
M.S. (University of California, Los Angeles) 2004

A dissertation submitted in partial satisfaction of the
requirements for the degree of

Doctor of Philosophy

in

Engineering - Electrical Engineering and Computer Sciences

in the

Graduate Division

of the

University of California, Berkeley

Committee in charge:

Professor Ming C. Wu, Chair
Professor Constance Chang-Hasnain
Professor Albert Pisano
Professor Kevin Healy

Fall 2008

The dissertation of Aaron Takami Ohta is approved:

Chair	_____	Date	_____
	_____	Date	_____
	_____	Date	_____
	_____	Date	_____

University of California, Berkeley

Fall 2008

Optofluidic Devices for Cell, Microparticle, and Nanoparticle Manipulation

© 2008

by Aaron Takami Ohta

ABSTRACT

Optofluidic Devices for Cell, Microparticle, and Nanoparticle Manipulation

by

Aaron Takami Ohta

Doctor of Philosophy in Engineering - Electrical Engineering and Computer Sciences

University of California, Berkeley

Professor Ming C. Wu, Chair

Research in the micro- to nanoscale regimes is facilitated by technologies that enable the addressing of these tiny particles. In biological research, manipulation enables the study of single-cell behavior, as well as the sorting of specific target cells from a mixed population. In engineering applications, micro- and nanoparticles can be assembled to form electronic and optoelectronic devices. Several types of forces can be used to manipulate micro- and nanoscale objects, including optical and electrical forces.

A device is presented that integrates the advantages of optical and electrical manipulation, called optoelectronic tweezers (OET). The OET device combines the advantages of both optical and electrical trapping. Optical patterns are used to create manipulation patterns and particle traps in an amorphous-silicon-based semiconductor device. The optical patterns create dielectrophoretic force in the OET device, via light-induced dielectrophoresis. Thus, OET does not directly use optical energy for trapping, allowing the use of much lower optical intensities than direct optical manipulation. These low optical intensities can be achieved by a computer projector or an LED, allowing the creation of complex optical manipulation patterns. Furthermore, unlike electrical traps, OET is capable of trapping a *specific* single microparticle from a larger population.

In this dissertation, the optoelectronic tweezers device is discussed in detail, including the operating principle, design considerations, and fabrication processes. OET manipulation is presented in the context of three major applications: sperm sorting for improving current *in vitro* fertilization techniques, microdisk laser assembly for CMOS-integrated optoelectronic devices, and nanowire assembly for nanowire-based displays.

Professor Ming C. Wu, Chair

TABLE OF CONTENTS

TABLE OF CONTENTS.....	i
LIST OF FIGURES	iv
LIST OF TABLES.....	xiii
ACKNOWLEDGEMENT	xiv
CHAPTER 1 INTRODUCTION	1
1.1 METHODS OF MICRO- AND NANOPARTICLE MANIPULATION.....	1
1.2 OPTOELECTRONIC TWEEZERS (OET)	5
1.3 CAPABILITIES OF OPTOELECTRONIC TWEEZERS	8
1.3.1 Massively Parallel Manipulation	8
1.3.2 Size-Based Particle Sorting.....	11
1.3.3 Image-Based Automated Cell Manipulation.....	14
CHAPTER 2 OPTOELECTRONIC TWEEZERS DESIGN AND FABRICATION 20	
2.1 INTRODUCTION	20
2.2 DESCRIPTION OF OPTOELECTRONIC TWEEZERS DEVICE.....	20
2.3 OPERATING PRINCIPLE OF OPTOELECTRONIC TWEEZERS	22
2.4 DIELECTROPHORESIS (DEP)	25
2.5 DESIGN OF OPTOELECTRONIC TWEEZERS	28
2.6 FINITE-ELEMENT MODELING.....	30
2.7 FABRICATION OF OPTOELECTRONIC TWEEZERS	37
2.8 CHARACTERIZATION OF OPTOELECTRONIC TWEEZERS PERFORMANCE	38
2.8.1 Photoconductivity Measurements	39
2.8.2 Particle Velocity	40
2.9 OTHER EFFECTS IN OPTOELECTRONIC TWEEZERS DEVICES	44
2.9.1 Electrolysis.....	44
2.9.2 Electrothermal Heating	45
2.9.3 Buoyancy Effects	45
2.9.4 Light-induced AC Electro-osmosis (LACE).....	46
2.9.5 Figure-of-Merit for OET Forces	47
CHAPTER 3 MANIPULATION OF CELLS.....	49
3.1 MOTIVATION.....	49
3.2 ISSUES WITH CELLULAR MANIPULATION	49
3.2.1 Media Conductivity and Osmotic Pressure.....	50
3.2.2 Non-Specific Cell Adhesion	52
3.3 SURFACE TREATMENTS FOR OPTOELECTRONIC TWEEZERS.....	52
3.4 TEFLON / BOVINE SERUM ALBUMIN SURFACE TREATMENT.....	54
3.5 POLY(ETHYLENE GLYCOL) SURFACE TREATMENT.....	55
3.6 CELL PATTERNING.....	61
3.7 SEPARATION OF LIVE AND DEAD WHITE BLOOD CELLS.....	63
3.8 SEPARATION OF LIVE JURKAT AND HELA CELLS	66

CHAPTER 4	SPERM SORTING FOR <i>IN VITRO</i> FERTILIZATION	71
4.1	MOTIVATION.....	71
4.2	EXPERIMENTAL SETUP	73
4.3	OET RESPONSE OF LIVE NON-MOTILE SPERM AND DEAD SPERM	75
4.4	CHARACTERIZATION OF DNA DAMAGE ON SPERM	76
4.5	FUTURE WORK.....	78
CHAPTER 5	LATERAL-FIELD OPTOELECTRONIC TWEEZERS (LOET).....	79
5.1	MOTIVATION.....	79
5.2	OPERATING PRINCIPLE OF LOET	82
5.3	DESIGN OF LOET.....	83
5.4	FABRICATION OF LOET	86
5.5	EXPERIMENTAL RESULTS	88
CHAPTER 6	III-V MICRODISK LASER ASSEMBLY ON SILICON USING LATERAL-FIELD OPTOELECTRONIC TWEEZERS	91
6.1	MOTIVATION.....	91
6.2	INP-BASED MICRODISK LASERS	93
6.3	LOET DEVICE FOR MICRODISK ASSEMBLY	96
6.4	III-V MICRODISK LASER ASSEMBLY ON A SILICON PLATFORM	99
6.5	OPTICAL MEASUREMENTS OF ASSEMBLED MICRODISKS	103
CHAPTER 7	NANOWIRE ASSEMBLY USING LATERAL-FIELD OPTOELECTRONIC TWEEZERS	107
7.1	MOTIVATION.....	107
7.2	NANOWIRE TRAPPING USING LATERAL-FIELD OPTOELECTRONIC TWEEZERS.....	108
7.3	NANOWIRE ROTATION AND TRAPPING USING PLANAR LATERAL-FIELD OPTOELECTRONIC TWEEZERS	110
7.3.1	Planar Lateral-Field Optoelectronic Tweezers	110
7.3.2	Nanowire Rotation and Assembly	113
CHAPTER 8	INTEGRATION OF OPTOELECTRONIC TWEEZERS AND ELECTROWETTING-ON-DIELECTRIC DEVICES.....	117
8.1	MOTIVATION.....	117
8.2	ELECTROWETTING-ON-DIELECTRIC (EWOD).....	119
8.3	INTEGRATED OET / EWOD DEVICE.....	120
8.3.2	Experimental Setup.....	123
8.3.3	Experimental Results	123
8.3.4	Design Issues	125
8.4	INTEGRATED PLANAR LOET / EWOD DEVICE.....	128
8.4.1	Fabrication	128
8.4.2	Experimental Setup.....	129
8.4.3	Experimental Results	130
8.4.4	Future Improvements.....	134
CHAPTER 9	OPTICALLY-ACTUATED THERMOCAPILLARY FORCES IN OPTOELECTRONIC TWEEZERS DEVICES	135
9.1	MOTIVATION.....	135
9.2	THEORY	137

9.3 EXPERIMENTAL SETUP	137
9.4 EXPERIMENTAL RESULTS	139
9.5 DISCUSSION	142
CHAPTER 10 CONCLUSION.....	143
APPENDIX 1 FABRICATION PROCESS OF OPTOELECTRONIC TWEEZERS	147
A1.1 UCLA FABRICATION PROCESS	147
A1.2 SILICON DISPLAY TECHNOLOGIES FABRICATION PROCESS.....	150
A1.3 UC BERKELEY FABRICATION PROCESS	153
APPENDIX 2 PEG COATING PROCESS.....	155
A2.1 PEG COATING ON A-SI ELECTRODES	155
A2.2 PEG COATING ON ITO-COATED ELECTRODES.....	157
BIBLIOGRAPHY.....	158

LIST OF FIGURES

Figure 1.1 Schematic of the optoelectronic tweezers device. The OET device uses optically-induced dielectrophoretic force to manipulate micro- and nanoscale objects. The illuminated areas create optically-defined electrodes on the photosensitive surface, creating electric field gradients that generate dielectrophoretic force.	6
Figure 1.2 Massively parallel manipulation of single particles [50]. (a) 15,000 particle traps are created across a 1.3 mm x 1.0 mm area. The 4.5- μm -diameter polystyrene beads experience negative OET forces and are trapped in the darker circular areas. Each trap has a diameter of 4.5 μm , which is adjusted to fit a single particle. (b) Parallel transportation of single particles. Three video images show the particle motion in a section of the overall manipulation area. The trapped particles in two adjacent columns move in opposite directions, as indicated by the blue and yellow arrows.	10
Figure 1.3 Optical setup for the generation of optical patterns using the DMD spatial light modulator.	11
Figure 1.4 An example of an integrated virtual optical machine [50]. (a) Integration of virtual components, including an optical sorter path, conveyors, joints and a wedge. The motion of different components is synchronized. (b) Fractionation of particles by size occurs in the z -direction due to differences in the OET force. (c, d) Two polystyrene particles with diameters of 10 and 24 μm pass through the sorter path and are fractionated in the z -direction. The particle trajectories can be switched at the end of the sorter path by the optical wedge.	13
Figure 1.5 Optical sorting repeatability test [50]. The white and black loops in Figure 1.4c and Figure 1.4d represent the particle trajectories after 43 cycles. The trace broadening at the white bar has a standard deviation of 0.5 μm for the 10- μm bead and 0.15 μm for the 24- μm bead.	14
Figure 1.6 (a) Automated OET system for real-time image-analysis feedback control. (b) Schematic of chip-scale sorting using OET.	16
Figure 1.7 Automated manipulation of HeLa cells. (a, b) HeLa cells are transported to the lower region of the field-of-view. (c) Trajectories of the HeLa cells entering the OET manipulation area from the left side of the image.	17
Figure 1.8 Automated particle sorting. (a, b) Continuous sorting of 15- and 20- μm -diameter polystyrene beads. The dashed lines indicated the edges of the OET manipulation area. (c) Trajectories of the beads entering the active area from the lower edge of the field-of-view ($y = 0$).	19
Figure 2.1 Cross-section of the OET device.	21
Figure 2.2 OET setup. A spatial light modulator is used to pattern a light source. The patterned light is focused onto the OET device using either (a) an additional objective lens or (b) the viewing objective lens.	22

Figure 2.3 Measured photoconductivity of amorphous silicon as a function of optical intensity. The light source is a 635-nm diode laser.	24
Figure 2.4 Simplified equivalent circuit model of the OET device.	25
Figure 2.5 Dielectrophoresis (DEP). (a) Positive DEP, where particles are attracted towards regions of high electric field. (b) Negative DEP, where particles are repelled from regions of high electric field. (c) The single-shell model for approximating the DEP response of biological shells. The cell membrane is represented by a permittivity and conductivity represented by ϵ_{mem} and σ_{mem} , respectively. The cell interior is represented by a separate permittivity and conductivity, represented by ϵ_{int} and σ_{int} , respectively.	27
Figure 2.6 Real part of the Clausius-Mossotti factor for red blood cells (RBC), B cells (a type of white blood cell), and yeast cells.	28
Figure 2.7 Absorption in amorphous silicon as a function of wavelength [75].	29
Figure 2.8 Force induced in the OET device as a function of the gap between the upper and lower electrodes.	30
Figure 2.9 Finite-element simulation showing the electric field strength in the liquid layer of the OET device. The highest electric fields occur in the center of the optical pattern, corresponding to the areas of highest electrical conductivity in the a-Si layer.	33
Figure 2.10 Finite-element simulation device showing $ \nabla E^2 $ in the liquid layer.	33
Figure 2.11 Finite-element simulation showing the x - and y -components of $ \nabla E^2 $	34
Figure 2.12 Finite-element simulation showing the z -component of $ \nabla E^2 $	34
Figure 2.13 Finite-element simulation of the electric field strength in the liquid layer for a ring trap pattern. The highest electric fields occur at the borders of the ring, corresponding to the areas of highest electrical conductivity in the a-Si layer.	36
Figure 2.14 Finite-element simulation of $ \nabla E^2 $ for a ring trap. Note the intensity scale is different between the top view and cross-sectional view.	36
Figure 2.15 Finite-element simulation showing the x - and y -components of $ \nabla E^2 $ for a ring trap. Note the intensity scale is different between the top view and cross-sectional view.	37
Figure 2.16 Finite-element simulation showing the z -component of $ \nabla E^2 $ for a ring trap. Note the intensity scale is different between the top view and cross-sectional view.	37
Figure 2.17 Fabrication of ITO-coated glass electrodes.	38
Figure 2.18 Amorphous silicon conductivity test structure.	40
Figure 2.19 Simulation of the real part of the Clausius-Mossotti factor for polystyrene beads in solutions of varying conductivities. The polystyrene beads experience	

negative OET for typical OET operating frequencies (real part of the Clausius-Mossotti factor < 0).....	41
Figure 2.20 Induced velocity of 20- μ m-diameter polystyrene beads as a function of applied voltage at 100 kHz for several illumination pattern widths [51].	43
Figure 2.21 Induced velocity of 20- μ m-diameter polystyrene beads as a function of the illuminated linewidth of the manipulation pattern [51]. The lower curve is for an applied bias of 10 Vpp at 100 kHz; the top curve is for a bias of 15 Vpp at 100 kHz.....	44
Figure 2.22 Dominant effects in the OET device [77]. Theoretical simulations are shown as dashed lines, and empirically-determined effects are shown as data points. The liquid solution has a conductivity of 1 mS/m. The applied voltage is at a frequency of 100 kHz, with amplitudes of (a) 20 Vpp and (b) 10 Vpp.	48
Figure 3.1 Percentage of live HeLa cells that can be transported under OET manipulation in standard OET devices. Non-specific cell adhesion limits the reliability of OET manipulation of mammalian cells. The error bars indicate the standard deviation of the measurements.	53
Figure 3.2 Percentage of live HeLa cells that can be transported under OET manipulation in BSA-coated OET devices. Non-specific cell adhesion is greatly reduced by using this passivation technique. However, rinsing the devices results in increased non-specific adhesion. The error bars indicate the standard deviation of the measurements.	55
Figure 3.3 Poly(ethylene glycol) (PEG) polymer chains resist cell and protein adhesion via entropic repulsion and osmotic pressure.....	56
Figure 3.4 XPS measurements of laminin adsorption on the a-Si electrode of an OET device. (a) Standard a-Si electrode. (b) PEG-coated a-Si electrode. The absence of an N 1s peak in this spectrum is an indicator of the resistance to protein adsorption.....	58
Figure 3.5 XPS measurements of laminin adsorption on the ITO electrode of an OET device. (a) Standard ITO electrode. (b) PEG-coated ITO electrode. The absence of an N 1s peak in this spectrum is an indicator of the resistance to protein adsorption.....	59
Figure 3.6 Percentage of live HeLa cells that can be transported under OET manipulation in PEG-coated OET devices. Non-specific cell adhesion is reduced 30 times by this passivation technique. The error bars indicate the standard deviation of the measurements.....	60
Figure 3.7 Comparison of the percentage of live HeLa cells that can be transported under OET manipulation in various OET devices. The PEG coating provides the most robust coating, and the most reliable OET manipulation. The error bars indicate the standard deviation of the measurements.	61
Figure 3.8 Formation of an array of live Jurkat cells on a PEG-coated OET device. (a, b) The original randomly-distributed cells are trapped and transported using OET	

manipulation patterns. (c) A 5 x 5 individually-addressable cell array is formed. (d) The same array, with the the OET manipulation pattern temporarily shut off for cell imaging clarity.....	62
Figure 3.9 OET spatial manipulation of multiple cell types. (a) The fluorescent-labeled Jurkat cells are distinguished from the unlabeled HeLa cells (composite image). (b) The Jurkat cells are arranged in a triangular pattern. (c) The HeLa cells are arranged in a square pattern. (d) Fluorescent imaging verifies that the cell types are segregated (composite image).	63
Figure 3.10 Real part of the Clausius-Mossotti factor for live and dead B cells.....	64
Figure 3.11 Selective concentration of live B cells from dead B cells [50]. (a) Initial positions of live (clear) and dead (dark) B cells. (b, c) A broken concentric ring pattern is used to transport the live cells to the center of the field-of-view while leaving the dead cells behind. (d) Live cells have been concentrated to the central region of the optical pattern.	65
Figure 3.12 OET-induced manipulation velocity of different cell types as a function of the frequency of the electric field [52]. Cells are manipulated using a 15- μ m-wide scanning line pattern.	67
Figure 3.13 Optical pattern for OET-enabled cell discrimination [52]. (a) Cells before the lines are scanned in the negative x -direction. The thin leading line produces a weaker OET force than the thicker trailing line. (b) As the pattern is scanned, the Jurkat cells have a sufficiently OET strong force to be retained by the leading line, while the HeLa cells do not experience sufficient force. (c) The trailing line provides enough force to transport the HeLa cells, while the Jurkat cells continue to be retained by the leading line, achieving spatial discrimination.	68
Figure 3.14 The OET manipulation velocity of Jurkat and HeLa cells as a function of the width of the optical pattern [52].....	68
Figure 3.15 OET-enabled spatial discrimination of live Jurkat and HeLa cells [52]. (a) Initial cell positions before the optical pattern is scanned from right to left across the field-of-view. (b) Cells are attracted to the leading line. The HeLa cell is starting to lag the scanning line. (c) Cells showing spatial separation after the scan is completed. An additional HeLa cell has moved into the field-of-view during the scan. (d) Fluorescent image of the cells in (c), verifying that the leading cells are the fluorescent-labeled Jurkat cells.	70
Figure 4.1 Setup of the OET device for sperm manipulation.	73
Figure 4.2 Sperm samples for OET manipulation.	74
Figure 4.3 OET-induced velocities of live non-motile sperm and dead sperm. The error bars indicate the standard deviation of the measurements. "All" refers to sperm velocities averaged across all 6 donors.	76
Figure 4.4 Comet assay on OET-manipulated sperm under different conditions. Similar levels of DNA fragmentation is evident in the pure control sample and the	

samples manipulated using OET (low dose and high dose). DNA fragmentation is present in sperm that was heated to 50°C for 5 minutes (inset).....	77
Figure 5.1 Electric field in the OET device. The color gradient shows the conductivity gradient in the a-Si layer, generated by illuminating the photoconductor. Note that the primary direction of the electric field is normal to the plane of the photosensitive electrode.....	80
Figure 5.2 (a) Microdisks, nanowires, and other anisotropic objects align normal to the plane of the electrodes of the OET device. (b) Torque exerted on a dipole in an electric field.....	80
Figure 5.3 Lateral-field optoelectronic tweezers device. The LOET device consists of an interdigitated array of photosensitive a-Si electrodes.	81
Figure 5.4 Simplified equivalent circuit model of the LOET device.	82
Figure 5.5 Electric field in the LOET device. The direction of the electric field is primarily parallel to the surface of the device.	83
Figure 5.6 Optimizing LOET dimension for particle dimensions. (a) Particles experiencing negative OET should be equal to or larger than the electrode dimensions w and g to ensure 2-D manipulation. (b) Particles experiencing positive OET should be equal to or larger than $2w + g$ to ensure 2-D manipulation.	84
Figure 5.7 Leakage fields in the LOET device. (a) An LOET device with ITO directly exposed to the liquid, with no undercut, shows significant leakage fields. White areas represent electric field strengths that are higher than the range of the scale bar. (b) An LOET device with a 2- μm undercut of the ITO beneath a 10- μm -wide a-Si electrode. The leakage fields are significantly reduced. (c) A further reduction of the leakage fields can be obtained by encapsulating the ITO electrodes with the a-Si layer.	86
Figure 5.8 Fabrication process of LOET devices.	88
Figure 5.9 Movement of 25- μm -diameter polystyrene beads in the LOET device. (a) The initial positions of the beads. (b) A laser is used to transport a single bead in the transverse direction, while simultaneously moving other beads in the longitudinal directions. Arrows indicate the direction of motion. (c) The final position of the polystyrene beads.....	89
Figure 5.10 Experimental induced velocities of polystyrene beads in the LOET device [52]. Longitudinal velocity refers to movement along an electrode, while transverse velocity refers to movement across electrode fingers. (a) Particle velocity as a function of illumination pattern intensity. (b) Particle velocity as a function of applied ac voltage at a frequency of 100 kHz.	90
Figure 6.1 Fabrication process for InGaAs/InGaAsP multiple-quantum-well (MQW) microdisk lasers.	95

Figure 6.2 5- μm -diameter microdisks on an InP substrate. (a) The disks are wet etched by 0.5% Br_2 in methanol, followed by partial etch of the InP sacrificial layer using diluted HCl. The rhombic grey region is an InP pedestal under the active layers of the microdisk. (b) Microdisk sidewall after etching. The smooth sidewall creates a high quality factor laser cavity.	95
Figure 6.3 The calculated magnetic field intensity profiles of the fundamental TE whispering gallery radial mode for 5- μm -diameter and 10- μm -diameter microdisks. The origins of the figures represent the center of the disks while the orange area represents the cross-section of the microdisks.	96
Figure 6.4 Schematic diagram of the integrated LOET device for microdisk laser assembly.....	97
Figure 6.5 Fabrication process of integrated LOET devices.	98
Figure 6.6 Finite-element simulation of the electric field profile across the LOET electrodes. The arrows show the direction of the optically-induced force. The strongest forces occur near the edges of electrodes with illumination.	99
Figure 6.7 Optical setup for microdisk assembly using LOET. A computer-controlled projector is used to generate optical patterns to attract and transport microdisks to a designated position.....	101
Figure 6.8 Assembly of 5- μm -diameter (a-c) and 10- μm -diameter (d-f) microdisks onto 3- μm -diameter silicon pedestals using LOET. (a, d) The initial positions of the microdisks. The optical trapping pattern, generated by a computer projector, is visible as a red rectangle. The target Si pedestal for assembly is indicated by an arrow. (b, e) The microdisks are positioned over the target Si pedestal. The trapping force is then increased to immobilize the disks on the substrates. (c, f) SEM pictures of assembled 5- and 10- μm -diameter microdisks.	102
Figure 6.9 Alignment accuracy measurement of assembled microdisks. The horizontal alignment is achieved by a self-alignment of the disks across the electrode gap. Vertical alignment is achieved by user control of the optical pattern.	103
Figure 6.10 Optical measurements of assembled microdisk lasers. (a) Lasing spectra from assembled 5- and 10- μm -diameter microdisks on silicon pedestals under pulsed excitation. The pump power for these two spectra is 1.7 mW for the 5- μm disks and 3.5 mW for the 10- μm disks. (b) Collected laser power versus peak pump power (L-L curves). The threshold pump powers for 5- and 10- μm disks are 0.85 mW and 2.5 mW, corresponding to 0.34 mW and 1 mW of effective absorbed power in the active layers.	105
Figure 6.11 L-L curves of assembled 5- μm microdisk lasers before and after thermal annealing. The maximum output power of a 5- μm microdisk laser is improved by annealing at 300 $^\circ\text{C}$ for 5 hours (Anneal 1), or 300 $^\circ\text{C}$ for 5 hours, followed by another anneal at 350 $^\circ\text{C}$ for 5 hours (Anneal 2). After annealing, the maximum output power is increased by 30% and 57% for annealing conditions 1 and 2, respectively.	106

Figure 7.1 Trapping and transport of silicon nanowires using LOET [61]. (a) The initial position of a silicon nanowire, with the electric field turned off. The laser spot is visible in the upper right. (b) The laser is moved closer to the nanowire. This frame is immediately before the electric field is switched on; after the electric field is applied, the nanowire is attracted towards the laser. (c) The trapped nanowire is transported by scanning the laser spot at up to 20 $\mu\text{m/s}$. (d) The laser is switched off to show the final position of the nanowire in greater clarity. The initial position is also indicated; the direction of the transport is shown by the arrow.	109
Figure 7.2 Schematic of planar lateral-field optoelectronic tweezers (PLOET) for nanowire assembly [62]. The device consists of an unpatterned amorphous silicon layer over an aluminum electrode array, fabricated on an oxidized silicon wafer. Paired triangular optical patterns create nanowire traps in between the metal electrodes.	111
Figure 7.3 Simplified equivalent circuit model of the PLOET device.	112
Figure 7.4 Finite-element simulation of the electric field profile across the PLOET electrodes.	113
Figure 7.5 Trapping of silver nanowires using PLOET [62]. Aluminum electrodes are visible underneath the amorphous silicon layer, at the top and bottom of each image. Optical patterns, visible as the bright areas, are used to create nanowire traps. The nanowire positions are indicated by dashed circles. (a, b) Transport of a nanowire in the negative x -direction at a rate of approximately 3 $\mu\text{m/s}$. (c, d) Transport of a nanowire in the positive y -direction. Other nanowires are weakly trapped at the edges of the electrodes, but can be moved by the LOET trap patterns. (e) Rotational control of a nanowire is achieved by moving the tips of the optical patterns relative to each other.	114
Figure 7.6 Measured photoluminescence of semiconductor nanowires for a red-green-blue nanowire LED display.	115
Figure 7.7 Fabrication of a silver nanowire array [62]. (a) Three nanowires have been trapped in parallel. (b) The nanowires are arranged in a closer, more regular spacing. Another nanowire can be seen to the left of the array. (c) The fourth nanowire is trapped by another set of optical patterns. The applied voltage is increased to assemble the nanowires on the surface of the device. (d) An SEM image of the nanowire array.	116
Figure 8.1 Principle of electrowetting-on-dielectric. An applied voltage changes the contact angle at the liquid/dielectric interface.	119
Figure 8.2 Typical EWOD device [124].	120
Figure 8.3 Cross-section of the integrated OET/EWOD device [64]. The top glass substrate has EWOD electrodes except for the central electrode, which is used for OET. The bottom glass substrate consists of the a-Si photosensitive OET electrode. Silicon dioxide and Cytop® are patterned on EWOD chip, except for the OET region, which only has a thin hydrophobic layer.	121

- Figure 8.4 Schematic of the integrated OET/EWOD device [64]. The light gray areas represent EWOD electrodes, and the dark gray represents the OET manipulation area. (a) A droplet containing cells is transported to the OET area using EWOD. (b) Using OET, cells are swept to left and individual cells are selected based on dielectric properties or visual differences. The droplet position relative to the OET area can be adjusted by the EWOD side-electrodes. (c) Using EWOD, desired cells are removed by generating a droplet, or waste medium is removed as droplets. A fresh droplet can be added from other directions to replenish cell medium. 122
- Figure 8.5 Droplet manipulation by EWOD [64]. (a, b) EWOD is used to transport a droplet with beads into OET manipulation region. (c, d) EWOD cuts a droplet out of the OET region as in Fig. 2(c). The dielectric pattern inside the OET electrode (rotated square) marks active OET region. Surrounding EWOD electrodes are used to move droplets into, out of and around OET region..... 124
- Figure 8.6 Particles swept to the left side of the image using OET [64]. (a) Each particle (dark dot) is pushed to left by an optical line pattern. (b) User-controlled optical patterns can also be used to sweep particles. (c) Nearly all particles in the OET region have been swept to the left (most are out of the field-of-view). The edges of the OET manipulation region are added for clarity..... 125
- Figure 8.7 Individual particle control using OET [64]. (a) A specific particle (circled) is chosen by the user, and transported to the right. (b, c) The selected particle is moved away from the others, as indicated by the arrow. The edges of the OET manipulation region are added for clarity..... 125
- Figure 8.8 EWOD electrode arrangements around the OET manipulation region with two alternative shapes for the hydrophilic opening. During EWOD droplet actuation, the fluid in the hydrophilic region remains stagnant (indicated by the flow lines), while causing flow near the meniscus to grow stronger. This creates strong viscous forces on particles outside the hydrophilic region, such as those labeled 1 and 2. 126
- Figure 8.9 Schematic of the operations performed on the integrated PLOET/EWOD device. The light arrows indicate droplet movement by EWOD while the dark arrow indicates the movement of the PLOET optical pattern. (a) A droplet containing cells is placed on the device. (b) To avoid disturbing the PLOET-generated particle distribution due to fluidic movements during the droplet cutting step, the droplet is positioned properly by EWOD prior to PLOET operations. The PLOET image pattern is then projected and moved across the droplet, transporting the cells upwards. (c) Since the droplet dimensions are larger than the PLOET image area, cell manipulation may be repeated over multiple regions to cover the entire droplet. (d) All but a few cells have been concentrated in one region. (e) The droplet is subsequently split using EWOD. (f) Cells have been separated into the collected droplet and the depleted droplet. 131
- Figure 8.10 EWOD functions during the operation of the integrated PLOET/EWOD device. (a) A 350-nL droplet containing HeLa cells is placed on the integrated

device. (b) The droplet is positioned so the PLOET-generated cell distribution is not disturbed during the droplet cutting. PLOET manipulation is performed starting from the bottom of the stretched droplet. (C) Collection of the cells from the lower (“depleted”) region into the upper (“collected”) region of the droplet. (d) The cell collection is performed across the width of the droplet to move most of the cells into the collected region. (e, f) After collection, the droplet is split into the “collected” (top) and “depleted” (bottom) droplets. 132

Figure 8.11 PLOET manipulation of HeLa cells within a droplet. The dark arrows indicate the movement direction of the optical pattern. (a) Since the cells experience positive OET, they are attracted to the pattern. (b) As the pattern moves up, the pattern more cells are collected. (c) The movement of the cells can be seen with respect to the EWOD features. (d to f) The pattern sweeps across multiple EWOD electrodes starting from the bottom of the droplet, collecting all the cells in the upper (“collected”) region. 133

Figure 9.1 Experimental setup for the optically actuated thermocapillary movement of air bubbles [160]. A 10 mW, 635 nm laser is focused onto the absorbing substrate of a fluidic chamber by a 20× objective lens. Air bubbles in the silicone oil have a contact angle of approximately 180°, as the oil completely wets the surface of the substrate. 138

Figure 9.2 Optically-actuated thermocapillary movement of an air bubble in silicone oil [160]. A 114-μm-diameter (1.0 nL) bubble is trapped in the thermal trap created by a laser focused on the absorbing substrate (a). The oil/air meniscus can be seen at the top left. The bubble follows the position of the laser spot, as it is scanned in the positive *y*-direction (b) and then in the positive *x*-direction (c). The bubble is then moved in the negative *y*- and negative *x*-directions (d). The initial bubble position is indicated by a dashed circle, and the approximate trajectory of the bubble is indicated by a dashed line..... 140

Figure 9.3 Optically-actuated thermocapillary movement-induced velocities of air bubbles as a function of laser intensity. The solid lines are linear fits to the data points..... 141

Figure A1.1 Fabrication process of OET devices fabricated at UCLA. 150

Figure A1.2 Fabrication process of OET devices with ITO and a-Si:H layers deposited by Silicon Display Technology. 152

Figure A1.3 Fabrication process of OET devices fabricated at UC Berkeley..... 154

LIST OF TABLES

Table 1.1 Types of OET devices.....	8
Table 2.1 Cell parameters for the simulation shown in Figure 2.6.....	28
Table 2.2 Simulation parameters for finite-element modeling.....	32
Table 5.1 LOET fabrication process overview.....	87
Table 6.1 Epitaxial layer structure of the microdisk lasers.....	94
Table A1.1 OET fabrication process overview (UCLA process).....	149
Table A1.2 Alternate fabrication process overview.....	151
Table A1.3 OET fabrication process overview (UC Berkeley process).....	153
Table A2.1 PEG coating process on a-Si electrodes.....	156
Table A2.2 PEG coating process on ITO electrodes.....	157

ACKNOWLEDGEMENT

I would like to thank my research advisor, Prof. Ming C. Wu. He has provided the mentorship and resources necessary for the success of my research endeavors. Prof. Pei-Yu “Eric” Chiou has also provided valuable mentorship and technical advice. I have benefited greatly from working with Ming-Chun “Jason” Tien, Hsan-Yin “Tony” Hsu, Arash Jamshidi, Justin Valley, and Dr. Steven Neale, as well as my other colleagues in the Integrated Photonics Laboratory.

Collaborators outside of our research group have supplied valuable materials, advice, and knowledge. This includes Prof. Chih-Ming Ho’s and Prof. Chang-Jin Kim’s groups from UCLA, and Prof. Peidong Yang’s, Prof. Ali Javey’s, and Prof. Ehud Isacoff’s groups at UC Berkeley. Collaborative research with Dr. Aldrich Lau and Dr. Huan Phan from Applied Biosystems has helped to improve the performance of our devices. In addition, some very exciting research has been done in conjunction with Prof. Tom Lue’s group from UCSF.

The National Science Foundation’s Graduate Research Fellowship program has graciously funded three years of my research.

I like to acknowledge my undergraduate research advisor, Prof. Wayne Shiroma of the University of Hawai’i at Manoa, who has helped me to reach this stage in my education. I also thank my friends for providing me with an outlet for stress relief, and for keeping me grounded. I especially thank Akane Takahashi for understanding about the busy life of a graduate student. Last, but definitely not least, I would like to thank my parents, Alan and Gayle, and my sister, Leigh, for much love and support.

Chapter 1 Introduction

1.1 Methods of Micro- and Nanoparticle Manipulation

Many research fields benefit from the ability to address particles in the micro- and nanoscale regimes. For example, biologists have traditionally studied cell behavior by observing the bulk response of a population of cells. However, it can be desirable to observe the behavior of a single cell in order to study phenomena such as cell-cell interactions, cell signaling pathways, mutations or genetic damage among a population, or the differentiation of stem cells. In addition, the response of a single cell is observed, rather than the average response of an entire population. Certain cells in a homogeneous population may exhibit behavior that deviates from the average response; single-cell observation may provide more insight into the cause of the deviant response. This information can be used in applications such as drug screening and cancer or disease detection and diagnosis.

Engineers and physicists are interested in non-biological particle manipulation. Nanostructures that exhibit quantum-mechanical behavior are interesting to researchers studying nanoscale physics, or to engineers who are exploiting the unique properties of nanomaterials to create improved devices. However, the difficulty in addressing and assembling these extremely small particles presents an obstacle to creating electronic or optoelectronic devices that incorporate nanostructures.

Micro- and nanoscale manipulation can be achieved with a variety of forces, including mechanical, magnetic, fluidic, optical, and electrokinetic forces. A wide variety of devices have been developed to control these forces for particle manipulation. Perhaps the most intuitive devices are mechanical manipulators, such as microgrippers for cells [1-3] or atomic-force microscope tips used for nanoparticle positioning [4, 5]. However, it is difficult to scale up the number of mechanical manipulators in order to increase the parallel manipulation capabilities of the device. In addition, non-contact methods are often preferred by biologists.

Magnetic forces are not invasive, but this limits manipulation to particles that either have an intrinsic magnetic response [6, 7] or are tagged with magnetic beads [8, 9]. Cellular tagging with magnetic beads has a high specificity and efficiency [10], but tagging protocols may not exist for all the cells of interest. As a result, tag-free protocols that do not require attaching cells to magnetic beads or other particles are more attractive to biologists.

Hydrodynamic forces are another non-contact method of cellular manipulation. Hydrodynamic forces have been used to trap [11, 12] and sort [13, 14] single cells. However, these devices require complicated pump systems and control systems, and the

high fluid flow rates in the microfluidic channels can induce shear stress on the cells, altering behavior such as protein expression [15].

Optical forces can also be used for cell manipulation, either through radiation pressure [16] or by the force exerted by the gradient of the optical field of a highly-focused laser beam, as in the classic optical tweezers trap [17]. Optical tweezers provides dynamic, flexible manipulation of specific single cells or particles, especially in configurations where dynamic optical tweezers traps may be created from a single input beam, in a technique known as holographic optical tweezers [18, 19]. Optical tweezers has been used in many research applications, such as measuring cell motility [20], sorting colloidal particles [21], sorting cells [22], and trapping and assembling nanowires [23, 24].

The basic single-beam optical tweezers trap is formed when a laser beam is highly focused. Near the focal point, lateral trapping forces are created due to the gradient force of the light. Along the axial direction of the laser beam, a force due to radiation pressure also exists. Thus, the trap is only stable in three dimensions if the axial gradient force near the focal point is stronger than the forces from radiation pressure. In order to generate sufficient trapping forces, laser intensities of approximately 10^5 to 10^7 W/cm² are typically used, which can damage some types of particles, including cells [25]. Cellular photodamage can be reduced by using infrared lasers [26, 27], but some harmful effects may still remain [27, 28].

In addition, to generate a sufficient gradient force, the laser is highly focused with high-numerical-aperture objective lenses. This results in a limited area over which the optical traps can be created, limiting the parallel manipulation capabilities of an optical

tweezers system. This limitation becomes more restrictive for larger particles, such as mammalian cells, which typically have diameters of approximately 10 μm . Other types of optical trapping, such as evanescent wave trapping [29, 30], are effective over larger areas, but have difficulty isolating a single particle from a larger population. Plasmonic-enhanced optical tweezers traps have also been demonstrated using low-numerical-aperture lenses [31], but significant optical intensities are still required to achieve particle or cell trapping (approximately $8 \times 10^3 \text{ W/cm}^2$) [31, 32].

Dielectrophoresis (DEP) is the electrical analog of optical tweezers. This phenomena, first described by Pohl in 1958 [33], relies on the gradient force of an electric field rather than an optical field. Dielectrophoretic force results when the interaction of the electric field gradient with the induced dipole of particles within the field produces a net force on the particles. DEP can act on a variety of particles, including non-conductive particles, conductive particles, particles that have a net electric charge, or particles that are charge-neutral. Typically, microfabricated metal electrodes are used to create electric field gradients that are sufficient to trap micro- and nanoscale particles [34-36].

DEP-based devices have been demonstrated in applications ranging from cell trapping and sorting [34, 35, 37-40] to carbon nanotube sample separation [41] and nanowire assembly [42, 43]. Electrode-based DEP devices have parallel manipulation capabilities, but the fixed trapping patterns limit the flexibility of individual devices, and make it difficult to isolate a single particle of interest. Spatially-varying electric fields can be generated by applying alternating phases to electrodes, transporting cells in what is known as traveling-wave dielectrophoresis [34]. However, the same limitations of

electrode-based DEP also apply to traveling-wave DEP, namely difficult in isolating specific single particles. True dynamic single-cell control requires active control of the electric field, achieved in a CMOS-circuit-based device that creates dynamic DEP cages [44, 45]. However, this device is limited by the pitch of the CMOS circuitry, and is currently limited the manipulation of microscale objects.

In addition to DEP, other electrokinetic forces may be used for particle manipulation, such as electrophoresis [36, 46]. However, electrophoresis only acts upon charged particles; charge-neutral particles will experience no force. Another electrokinetic effect, electroosmotically-driven fluid flows, have also been used to manipulate cells and other particles [47, 48], but like electrode-based DEP, these devices have fixed manipulation patterns.

1.2 Optoelectronic Tweezers (OET)

Another approach to single-particle manipulation combines aspects of both optical tweezers and dielectrophoresis, resulting in optically-induced dielectrophoresis. This technology, which we call optoelectronic tweezers (OET), uses a photosensitive surface to allow optical patterns to control the electric field landscape [49, 50]. The resulting non-uniform electric field then generates a DEP force on particles in the OET device (Figure 1.1). As optical energy is not directly used for trapping, much lower optical intensities can be used as compared to optical tweezers, in the range of 0.01 to 10 W/cm². These optical intensities can be achieved by a computer projector or an LED, allowing the creation of complex optical manipulation patterns [50, 51]. In addition, the optical gradient force is no longer required, relaxing the focusing requirements and allowing the use of low numerical aperture lenses. As a result, in our current configuration, the

effective manipulation of OET is 500 times larger than that of a typical optical tweezers setup. Furthermore, since the manipulation patterns are controlled optically, OET retains the flexibility and dynamic control enjoyed by optical tweezers. Unlike electrode-based DEP, OET is capable of trapping a *specific* single particle from a larger population. In addition to the advantages presented by optically-controlled manipulation, OET also retains the properties of DEP. Different cells experience varying DEP forces, allowing the separation of cells based on the DEP response [50, 52].

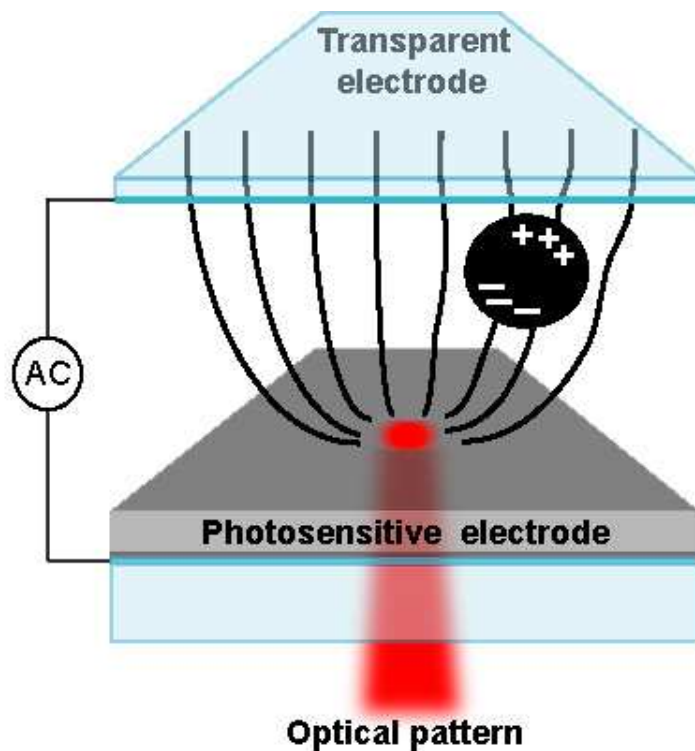


Figure 1.1 Schematic of the optoelectronic tweezers device. The OET device uses optically-induced dielectrophoretic force to manipulate micro- and nanoscale objects. The illuminated areas create optically-defined electrodes on the photosensitive surface, creating electric field gradients that generate dielectrophoretic force.

Since OET was developed by our research group in 2003 [49], OET manipulation has been demonstrated on a variety of microparticles, including polystyrene beads [50-56],

semiconductor microdisks [57], *E. coli* bacteria [58], red blood cells [51, 56], white blood cells [50-52], HeLa cells [52, 59], Jurkat cells [52], and yeast cells [53]. In addition, OET is capable of manipulating nanostructures, such as semiconducting and metallic nanowires [60-62].

The source of optical actuation for the OET device can be coherent or incoherent. Thus, a variety of light sources can be used for OET manipulation, including low-power lasers [49], halogen lamps [50], and LEDs [50, 52]. The optical source and the optical patterning system can also be integrated by focusing the output of a computer projector [51] or LCD [55, 56] onto the OET device. Directly using an LCD as in ref [55] creates a feature-rich lab-on-a-display that has a smaller footprint than many microfluidic lab-on-a-chip devices that require bulky external fluidic pumps.

Alternate configurations of the OET device include using amorphous silicon for both of the electrode surfaces [63], which has been shown to reduce the stiction of polystyrene beads by reducing their contact to the electrode surfaces of the device. We have also integrated OET with electrowetting-on-dielectric devices [64] in order to manipulate particles within aqueous droplets. This configuration is described further in Chapter 8. In addition, the photosensitive electrode of the OET device can be altered to create a device that uses only one substrate. In this device, the electric field direction is primarily parallel to the surface of the substrate, so we call this configuration lateral-field optoelectronic tweezers (LOET) [52, 57, 61]. The LOET device can be more easily integrated with other microdevices, as there is only one substrate. In addition, anisotropic particles such as microdisks [57] and nanowires [61, 62] align with their long axis parallel to the surface of the OET device, unlike in the standard OET device [60]. The LOET device is

described further in Chapter 5. We have also developed another variant of LOET, called planar LOET (PLOET) [62], which is described in Chapter 7.3. Finally, another variant of the OET device can be used to manipulate aqueous droplets in oil for cell-based assays, and is known as floating-electrode OET [65]. The types of OET devices are summarized in Table 1.1.

Table 1.1 Types of OET devices

Type of OET device	Description	Inventors	Key reference(s)
OET	Original OET device	Chiou, Ohta, Wu	[50], Chapters 1 to 4, 8, 9
OET / EWOD	Integration with EWOD device	Shah, Chiou, Ohta, Wu	[64], Chapter 8
LOET	Single-sided, lateral-field device	Ohta, Chiou, Jamshidi, Hsu, Wu	[52], Chapters 5 to 7
PLOET	Single-sided, planar lateral-field device	Ohta, Neale, Jamshidi, Hsu, Wu	[62], Chapter 7.3
3D OET	a-Si on both electrode surfaces	Hwang, et al.	[63]
FE-OET	Manipulation of droplets in oil	Park, et al.	[65]

1.3 Capabilities of Optoelectronic Tweezers

Here, some of the capabilities of the OET device will be described, including massively parallel single-particle manipulation, size-based particle sorting, and image-feedback-controlled manipulation and sorting. These capabilities enable the use of OET for interesting applications, which will be discussed in further detail in subsequent chapters.

1.3.1 Massively Parallel Manipulation

A demonstration of the high-resolution manipulation capabilities of OET is the creation of 15,000 OET traps across an area of 1.3 mm x 1.0 mm solely using optical patterning (Figure 1.2) [50]. The optical pattern is created by illuminating a digital

micromirror device (DMD) spatial light modulator (Texas Instruments) with a 100-W halogen lamp (Figure 1.3). The image created by the DMD is focused onto the OET device using a 10× objective lens with a numerical aperture of 0.3. The particles are trapped in the darker circular areas of the projected manipulation pattern by the induced negative (repulsive) OET forces, which push the beads into the non-illuminated regions where the electric field is weaker. The size of each trap is optimized to capture a single 4.5- μm -diameter polystyrene bead, and corresponds to a 3 x 3 array of DMD pixels. By programming the projected images using a computer interface, these trapped particles can be individually moved in parallel (Figure 1.2b).

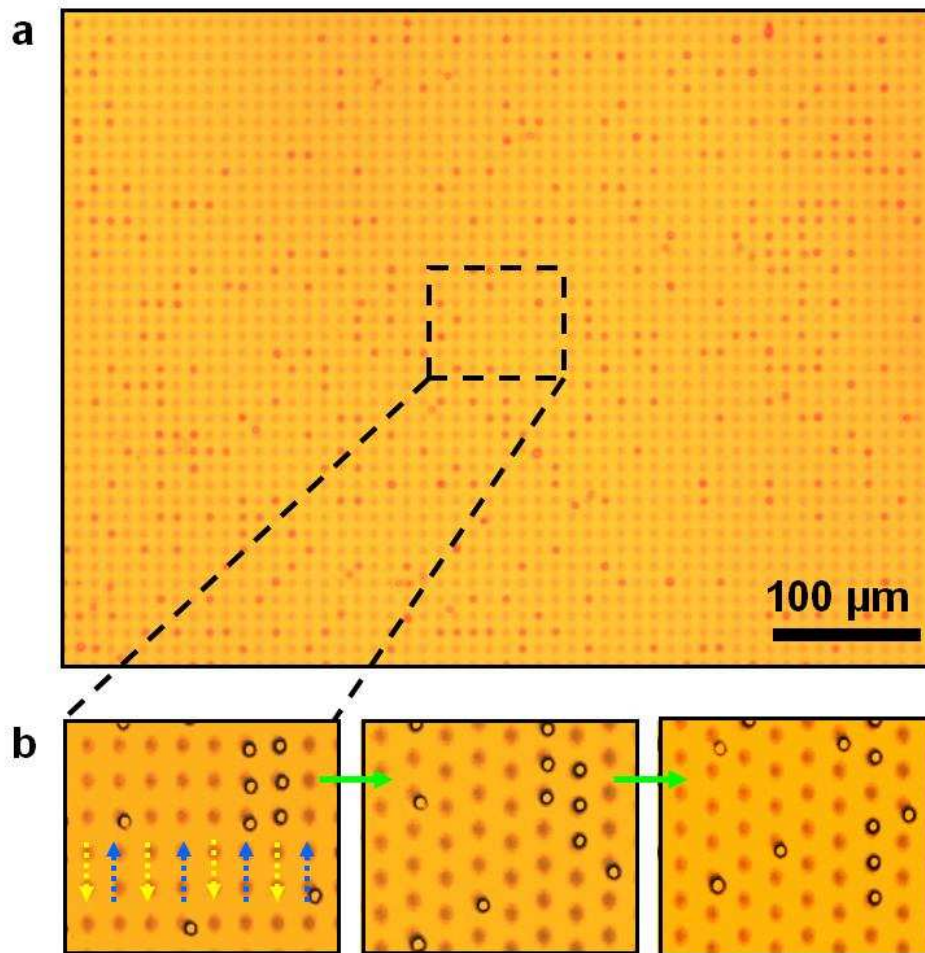


Figure 1.2 Massively parallel manipulation of single particles [50]. (a) 15,000 particle traps are created across a 1.3 mm x 1.0 mm area. The 4.5- μm -diameter polystyrene beads experience negative OET forces and are trapped in the darker circular areas. Each trap has a diameter of 4.5 μm , which is adjusted to fit a single particle. (b) Parallel transportation of single particles. Three video images show the particle motion in a section of the overall manipulation area. The trapped particles in two adjacent columns move in opposite directions, as indicated by the blue and yellow arrows.

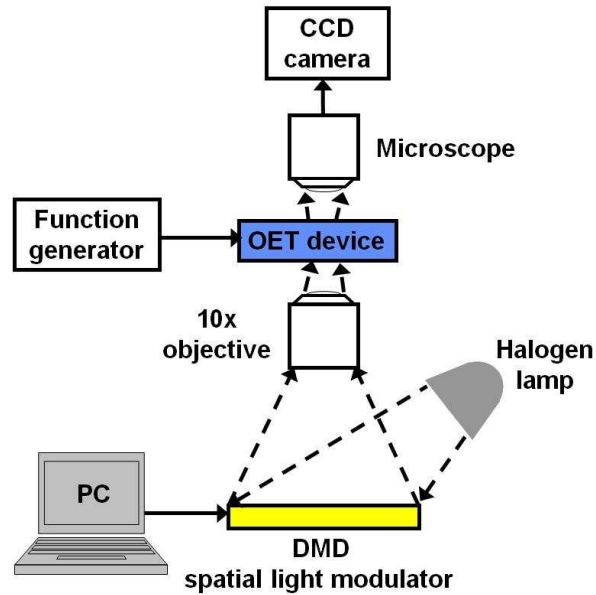


Figure 1.3 Optical setup for the generation of optical patterns using the DMD spatial light modulator.

1.3.2 Size-Based Particle Sorting

The optically-induced force in the OET device depends on the volume of the particle (explained further in Chapter 2.4), so particles of varying size will experience varying strengths of OET forces. This can be used to automatically sort particles based on their size. We have demonstrated this using a DMD spatial light modulator to create a continuous sorting pattern without the assistance of fluidic flow [50]. Figure 1.4 shows an example of an integrated optical manipulator that combines the functions of optical conveyors, sorters, wedges and joints. Particles are transported through different functional areas and recycled in this light-patterned circuit, traveling through different paths depending on the size of the particle. Particles with different sizes are fractionated in the lateral z -direction as they pass through the sorter path, due to the angled shape of the optical patterns (Figure 1.4b). Larger particles are moved more easily by the

optically-induced DEP forces, and do not require as strong of an electric field gradient. Thus, the larger particles travel on a trajectory that has a higher value of z . Smaller particles need a larger electric field gradient to be transported at the same velocity as larger particles, and move up along the field gradient. Thus, the trajectory of smaller particles has a lower value of z . The distinct trajectories of a larger 24- μm -diameter polystyrene bead and a smaller 10- μm -diameter polystyrene bead can be seen in Figure 1.4c. At the end of the sorter path, an optical wedge divides and guides the particles into the two conveyors. The looped optical conveyors then recycle the particles back to the sorter input to repeat the process. The paths of the fractionated particles can be switched by reconfiguring the tip position of the optical wedge (Figure 1.4c, d). The trajectories of the particle movement are highly repeatable and accurately defined. Figure 1.5 shows the distribution of the particle position in the middle of the sorter (marked by a white bar in Figure 1.4c, d) after the same particles have passed through the sorter 43 times. The standard deviations of trace broadening are 0.5 μm for the 10- μm bead and 0.15 μm for the 24- μm bead. The larger particle shows a better confinement in the optically-patterned OET cages during transportation due to a larger OET force.

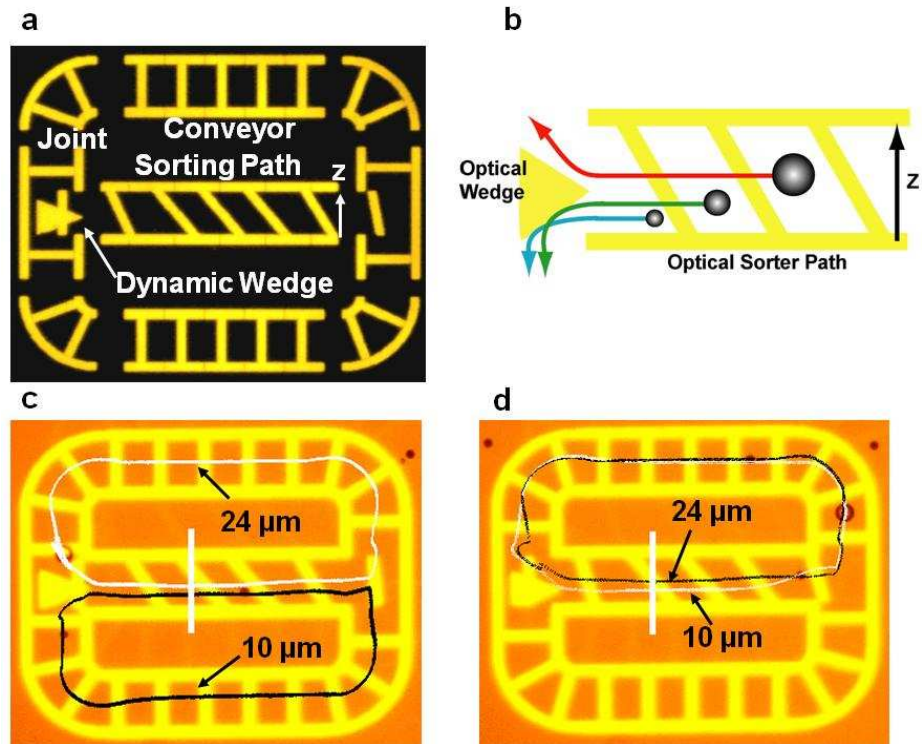


Figure 1.4 An example of an integrated virtual optical machine [50]. (a) Integration of virtual components, including an optical sorter path, conveyors, joints and a wedge. The motion of different components is synchronized. (b) Fractionation of particles by size occurs in the z -direction due to differences in the OET force. (c, d) Two polystyrene particles with diameters of 10 and 24 μm pass through the sorter path and are fractionated in the z -direction. The particle trajectories can be switched at the end of the sorter path by the optical wedge.

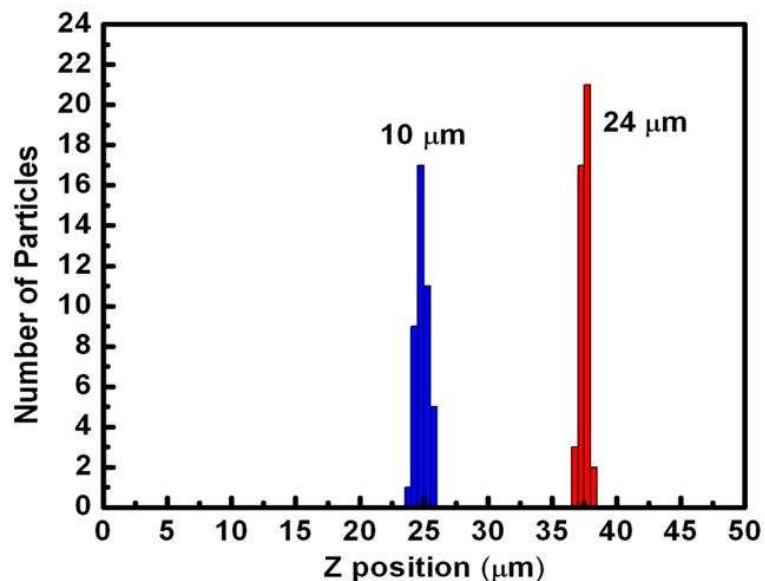


Figure 1.5 Optical sorting repeatability test [50]. The white and black loops in Figure 1.4c and Figure 1.4d represent the particle trajectories after 43 cycles. The trace broadening at the white bar has a standard deviation of 0.5 μm for the 10- μm bead and 0.15 μm for the 24- μm bead.

1.3.3 Image-Based Automated Cell Manipulation

The most practical method of controlling a large number of particles in parallel is through the use of image-feedback-controlled optical manipulation pattern generation. The feedback control is combined with a continuously moving OET platform, creating a large manipulation area by rastering the OET device across the microscope field of view [66]. The experimental setup is shown in Figure 1.6a. The system uses a liquid-crystal spatial light modulator (Hamamatsu Photonics Corp.) to generate image patterns for optical manipulation. A 10-mW, 635-nm laser is expanded 10 times to cover the image-generating surface of the spatial light modulator (SLM). The patterned light is focused onto the OET device through a 10x objective lens. The OET device is mounted on a motorized stage.

The image-feedback-control is realized by capturing the microscope image using a video CCD camera, and analyzing the video feed with an image-processing software (Processing 1.0 [67]) to determine particle characteristics such as size, color, texture, or shape. Based on this information, a corresponding optical pattern is generated by the software, and transferred to the SLM for projection onto the OET device. In order to manipulate a larger number of particles, the OET chip is programmed to move continuously across the manipulation area using the motorized stage (Figure 1.6b). As the particles move through the OET manipulation area, the randomly distributed particles are sorted into multiple groups.

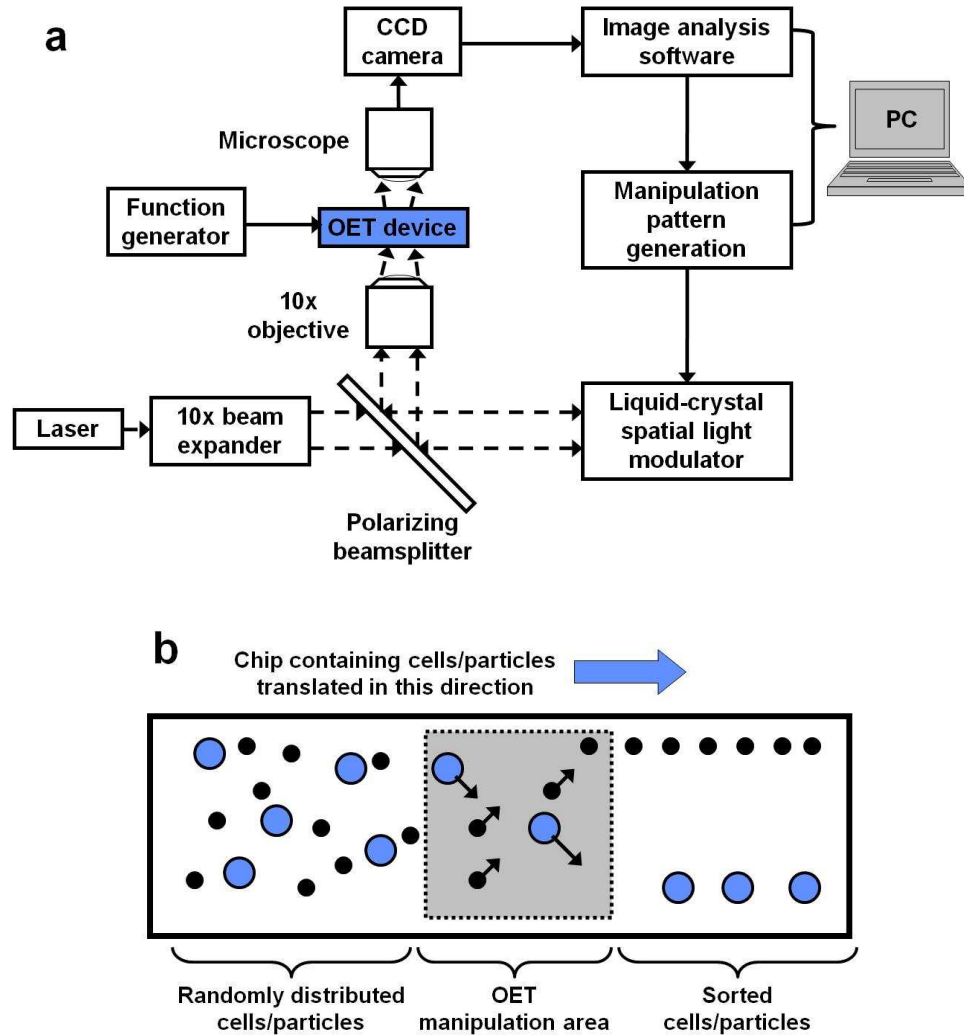


Figure 1.6 (a) Automated OET system for real-time image-analysis feedback control. (b) Schematic of chip-scale sorting using OET.

Automated cell trapping is demonstrated using HeLa cells, a cervical carcinoma cell line (Figure 1.7) [66]. The stage carrying the OET device moves from the left to the right at a constant speed of $5 \mu\text{m/s}$. The cells enter the OET manipulation area from the left side of the screen and trigger the SLM to switch on the pixels below the cells, projecting the corresponding optical patterns. Unlike polystyrene beads, the cells experience a positive (attractive) OET response, and are pulled by the optical patterns towards the

lower edge of the field-of-view. Once the corresponding cell reaches the lower edge of the field-of-view, the optical trapping patterns are deactivated. The linear trajectories of the cells show that a constant OET force is generated across the manipulation area (Figure 1.7c).

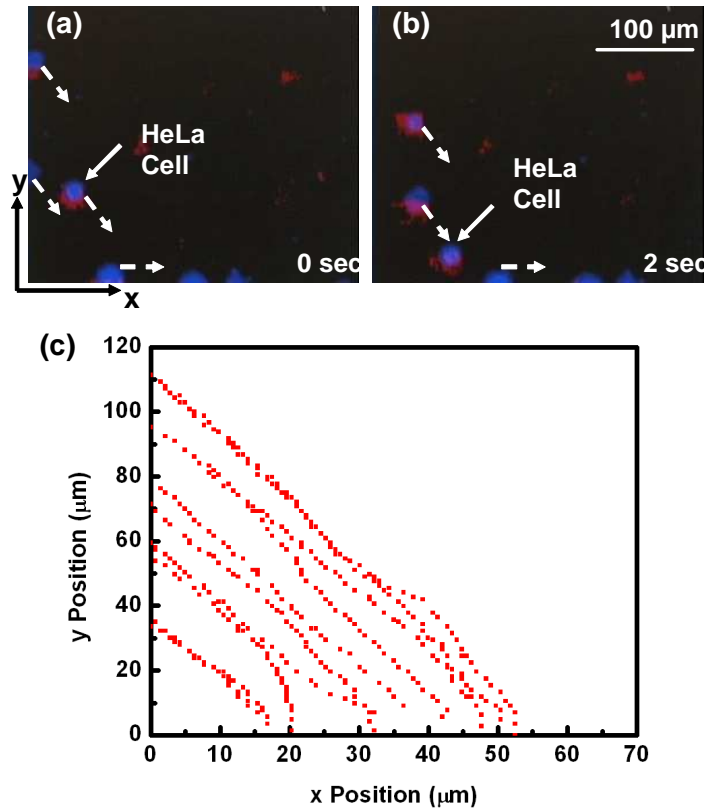


Figure 1.7 Automated manipulation of HeLa cells. (a, b) HeLa cells are transported to the lower region of the field-of-view. (c) Trajectories of the HeLa cells entering the OET manipulation area from the left side of the image.

Image-feedback control provides another method of size-based sorting. The image-analysis software can be used to identify the size of particles, and generate the appropriate sorting patterns. This has been demonstrated with the sorting of a mixed population of 15- and 20-μm-diameter polystyrene beads. The beads enter the active area from the lower edge of the field-of-view as the microscope stage moves at a velocity of

10 $\mu\text{m/s}$. The bead sizes are identified, and optical patterns are generated to sweep the 20- μm beads to the left edge of the manipulation area, while the 15- μm particles are swept to the right edge (Figure 1.8) [66]. The dashed black lines represent the edges of the OET manipulation area.

In our current system, the throughput is limited by the refresh rate of the SLM, which is 5 frames/s. Moving the stage at a velocity greater than 15 $\mu\text{m/s}$ introduces a time delay to the optical patterns projected onto the OET surface, resulting in a reduced sorting efficiency. The highest particle concentration that has been successfully sorted in this system is 1600 beads/ mm^2 , corresponding to a sorting throughput of 120 beads/min in the OET manipulation area. A higher stage velocity, and thus a higher throughput can be achieved by incorporating prediction algorithms in the image analysis software.

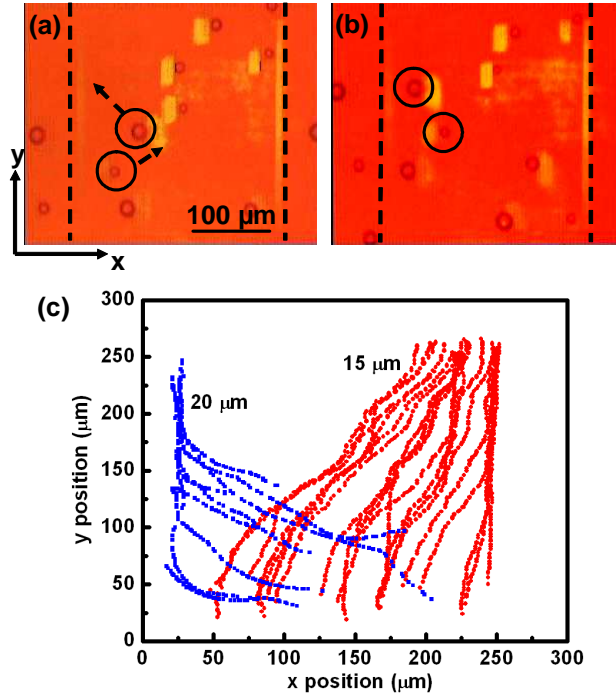


Figure 1.8 Automated particle sorting. (a, b) Continuous sorting of 15- and 20- μm -diameter polystyrene beads. The dashed lines indicated the edges of the OET manipulation area. (c) Trajectories of the beads entering the active area from the lower edge of the field-of-view ($y = 0$).

Chapter 2

Optoelectronic Tweezers Design and Fabrication

2.1 Introduction

The physical mechanism of optoelectronic tweezers is that of optically-induced dielectrophoresis. In this chapter, the physics of OET will be explained, illustrating how light can be used to pattern an electric field within the OET device. Dielectrophoresis, the force that is produced in the OET device, will also be described. Design considerations and constraints of the OET device will be discussed, along with methods of simulating OET operation using finite-element modeling. The fabrication process of OET is also disclosed, as well as methods of characterizing OET performance. Finally, a brief discussion of other effects present in the OET device will be presented.

2.2 Description of Optoelectronic Tweezers Device

The OET device consists of two electrodes (Figure 2.1). The upper transparent electrode consists of a 100-nm-thick layer of indium tin oxide (ITO), a transparent

conductive material, on a glass substrate. The lower photosensitive electrode typically consists of featureless layers of ITO and intrinsic amorphous silicon (a-Si) on a glass substrate. The upper and lower electrodes are of equal area, typically 1.5 cm by 2.5 cm. The two electrodes are separated by spacers, creating a chamber between the electrodes that is typically 100 μm in height. An aqueous solution containing the cells or particles under manipulation is introduced into the chamber between the electrodes. An electric field is created in the device by applying an ac bias across the top and bottom electrodes.

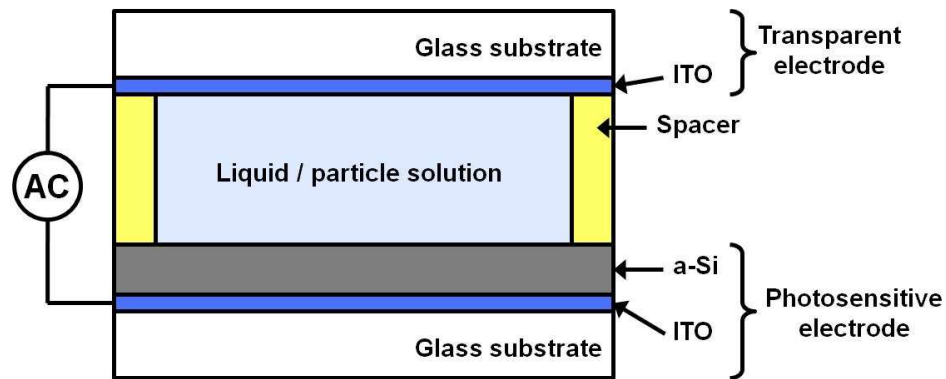


Figure 2.1 Cross-section of the OET device.

The OET device is placed under a microscope to observe the particles under manipulation (Figure 2.2). Optical patterns are focused onto the photosensitive surface, typically using a microscope objective lens. The focusing objective can be a separate lens (Figure 2.2a), or the same lens as the microscope observation objective (Figure 2.2b). The optical source is rather flexible. A low-power laser can be used, or an incoherent light source such as a halogen or mercury lamp, or a light-emitting diode (LED). Optical patterns are created using spatial light modulators, such as a digital micromirror device (DMD) (Texas Instruments), which consists of a MEMS mirror array. Another alternative

is a liquid-crystal-based spatial light modulator (Hamamatsu Photonics Corp.). The optical source and the optical patterning system can also be integrated by focusing the output of a computer projector or LCD onto the OET device.

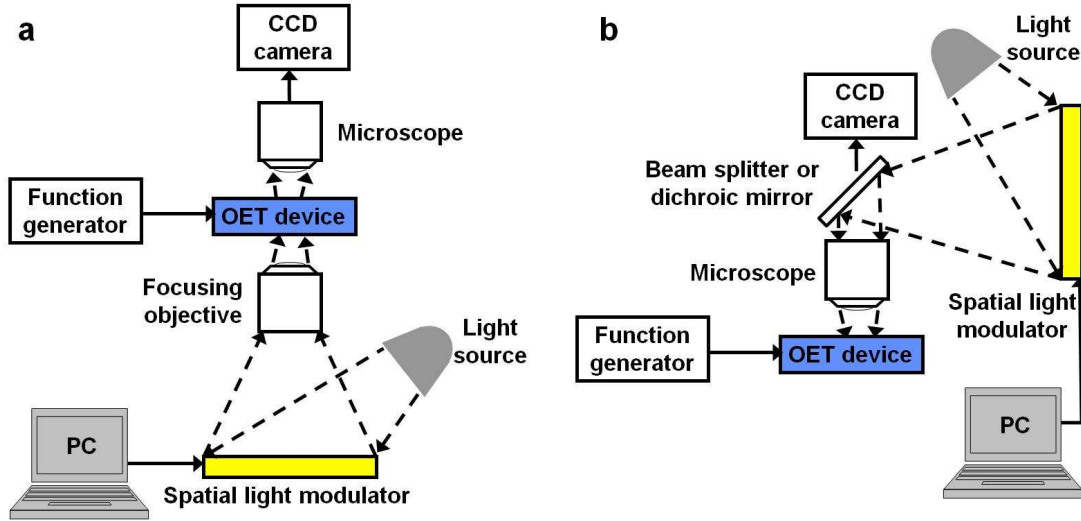


Figure 2.2 OET setup. A spatial light modulator is used to pattern a light source. The patterned light is focused onto the OET device using either (a) an additional objective lens or (b) the viewing objective lens.

2.3 Operating Principle of Optoelectronic Tweezers

The OET device relies on optically-induced dielectrophoresis to impart a force on the particles under manipulation. The dielectrophoretic force is controlled by optical patterns that are projected on the photosensitive surface of the device.

Amorphous silicon, the material used in the photosensitive electrodes of OET, has its conductivity modulated by the intensity of the light that is absorbed in the material (Figure 2.3). Under ambient lighting conditions and a 5V bias, the a-Si film has a conductivity of 0.9×10^{-6} S/m. However, when illuminated with light, photogenerated charge carriers are produced in the a-Si. As a result, the conductivity of the a-Si layer increases by a few orders of magnitude, to 2.1×10^{-3} S/m under an illumination intensity

of 10 W/cm^2 . The a-Si layer thus has two states; a low-conductivity dark (“off”) state, and high-conductivity illuminated (“on”) state. Furthermore, the transition between these two states is confined to the region under illumination, due to an ambipolar diffusion length of only 115 nm in amorphous silicon [68]. These two states allow the a-Si layer to act as an optically-controlled and optically-defined electrode, with a resolution limited to the optical diffraction limit. The diffraction limit is given by

$$\text{Diffraction limit} = 1.22 \frac{\lambda}{2N.A.} \quad (2.1)$$

where λ is the wavelength of the light and $N.A.$ is the numerical aperture of the focusing lens. Typical values in OET operation are $\lambda \approx 630 \text{ nm}$ and $N.A. \approx 0.3$, which corresponds to a diffraction-limited feature size of approximately $1.3 \text{ }\mu\text{m}$.

The function of the a-Si photoconductive layer can be seen by modeling the OET devices with a simplified equivalent circuit model (Figure 2.4). In the dark state, the impedance of the a-Si, Z_{PC} , is larger than the impedance of the liquid layer, Z_L . Thus, in areas with no illumination, most of the applied ac voltage drops across the high impedance of the a-Si layer. However, Z_{PC} becomes significantly lower in the illuminated areas, allowing a significant voltage drop to occur across the liquid layer. In this manner, an electric field gradient is set up between the illuminated and dark areas in the OET device.

The conductivity of the liquid media in the OET device is an important consideration. The liquid impedance, Z_L , plays an important role in the impedance-divider equivalent circuit model of Figure 2.4. If the liquid impedance is too low, the OET device will not be able to fully switch the applied voltage to the liquid layer, even in the illuminated (on-

state) areas. As a result, OET force is minimized if the liquid conductivity is too large. The operation of the OET device uses illumination intensities of 10 W/cm^2 or less to avoid the excitation of undesirable operating regimes (see Chapter 2.9). These optical intensities limit the maximum photoconductivity of the a-Si to approximately 2 mS/m . Thus, efficient OET operation is limited to liquids with conductivities of approximately 20 mS/m or less. A typical OET experiment uses a liquid media with a conductivity of 1 to 10 mS/m .

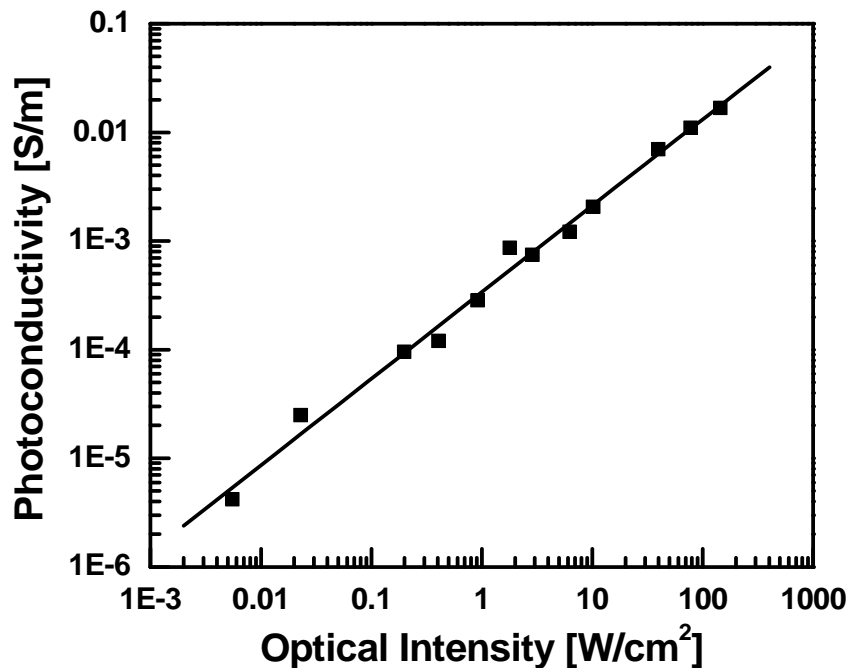


Figure 2.3 Measured photoconductivity of amorphous silicon as a function of optical intensity. The light source is a 635-nm diode laser.

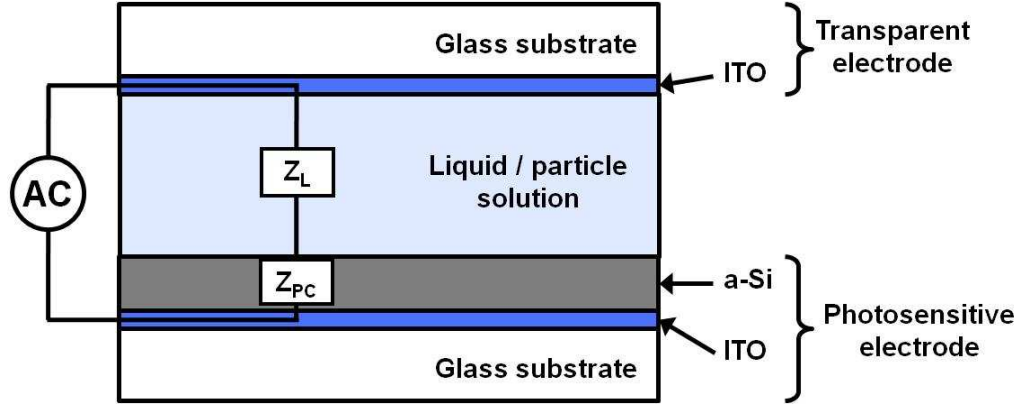


Figure 2.4 Simplified equivalent circuit model of the OET device.

2.4 Dielectrophoresis (DEP)

Electric field gradients in the OET device result in an optically-induced dielectrophoretic (DEP) force. This DEP force results from the interaction of a non-uniform electric field and the induced dipole of a particle within the electric field. The forces at each end of the particle's dipole are unequal due to the non-uniform field, resulting in a net force (Figure 2.5a, b). This force can be described by the following equation:

$$F = \bar{p} \cdot \nabla \bar{E} \quad (2.2)$$

where \bar{p} is the dipole moment of the particle, and \bar{E} is the first term of the Taylor series expansion of the electric field [69]. If the particle is a homogeneous dielectric sphere (e.g. a polystyrene bead), then the time-averaged DEP force reduces to:

$$F_{DEP} = F_{OET} = 2\pi r^3 \epsilon_m \text{Re}[K(\omega)] \nabla E_{rms}^2 \quad (2.3)$$

where r is the particle radius, ε_m is the permittivity of the medium surrounding the particle, E_{rms} is the root-mean-square electric field strength, and $\text{Re}[K(\omega)]$ is the real part of the Clausius-Mossotti factor, given by:

$$K(\omega) = \frac{\varepsilon_p^* - \varepsilon_m^*}{\varepsilon_p^* + 2\varepsilon_m^*}, \varepsilon_p^* = \varepsilon_p - j\frac{\sigma_p}{\omega}, \varepsilon_m^* = \varepsilon_m - j\frac{\sigma_m}{\omega} \quad (2.4)$$

where ε is the permittivity of the particle or medium (denoted by a subscript p or m , respectively), σ is the conductivity of the particle or medium, and ω is the angular frequency of the electric field [69]. The magnitude of $\text{Re}[K(\omega)]$ varies with frequency, resulting in a frequency-dependence of the dielectrophoretic force. Positive values of $\text{Re}[K(\omega)]$ result in particle attraction to electric field maxima (Figure 2.5a). This phenomenon is positive DEP, referred to here as positive OET. For negative values of $\text{Re}[K(\omega)]$, particles are repelled from field maxima (Figure 2.5b). This phenomenon is negative DEP, referred to here as negative OET. Applying an ac electric field thus allows the tuning of the type of DEP force induced on a particle, as well as negating any electrophoretic effects, or particle movement due to its surface charge.

If the particles experiencing a DEP force are not homogeneous throughout their volumes, the Clausius-Mossotti factor is affected. This is the case for biological cells, which, unlike polystyrene beads, are not homogeneous. Thus, a single-shell model is typically used to determine the frequency-dependent Clausius-Mossotti factor for mammalian cells (Figure 2.5c). The permittivity and conductivity of the cell membrane and interior are used to determine an effective complex permittivity that can then be used in Equation 2.4. This effective permittivity is given by:

$$\epsilon_p^* = C_{mem}^* \frac{r \epsilon_{int}^*}{\epsilon_{int}^* + C_{mem}^* r} \quad (2.5)$$

where ϵ_{int}^* is the complex internal conductivity of the cell, and it is assumed that the thickness of the cell membrane, d , is much less than the radius of the cell interior, r [70].

The membrane capacitance, C_{mem}^* , is given by:

$$C_{mem}^* = \frac{\epsilon_{mem}}{d} - \frac{j\sigma_{mem}}{d} \quad (2.6)$$

Many cell types are uniquely distinguishable by the real part of the Clausius-Mossotti factor (Figure 2.6, Table 2.1). This enables the separation of different cell types using DEP force.

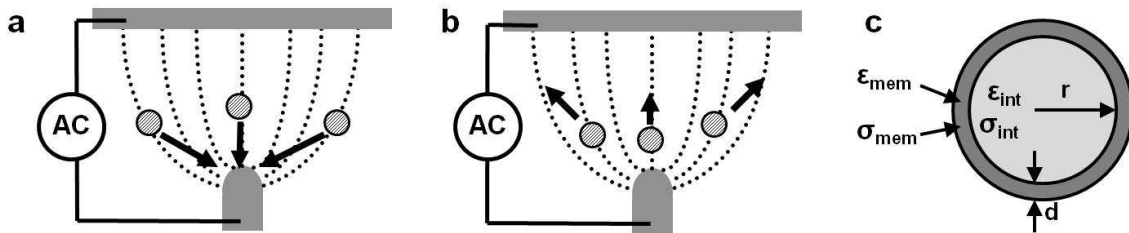


Figure 2.5 Dielectrophoresis (DEP). (a) Positive DEP, where particles are attracted towards regions of high electric field. (b) Negative DEP, where particles are repelled from regions of high electric field. (c) The single-shell model for approximating the DEP response of biological shells. The cell membrane is represented by a permittivity and conductivity represented by ϵ_{mem} and σ_{mem} , respectively. The cell interior is represented by a separate permittivity and conductivity, represented by ϵ_{int} and σ_{int} , respectively.

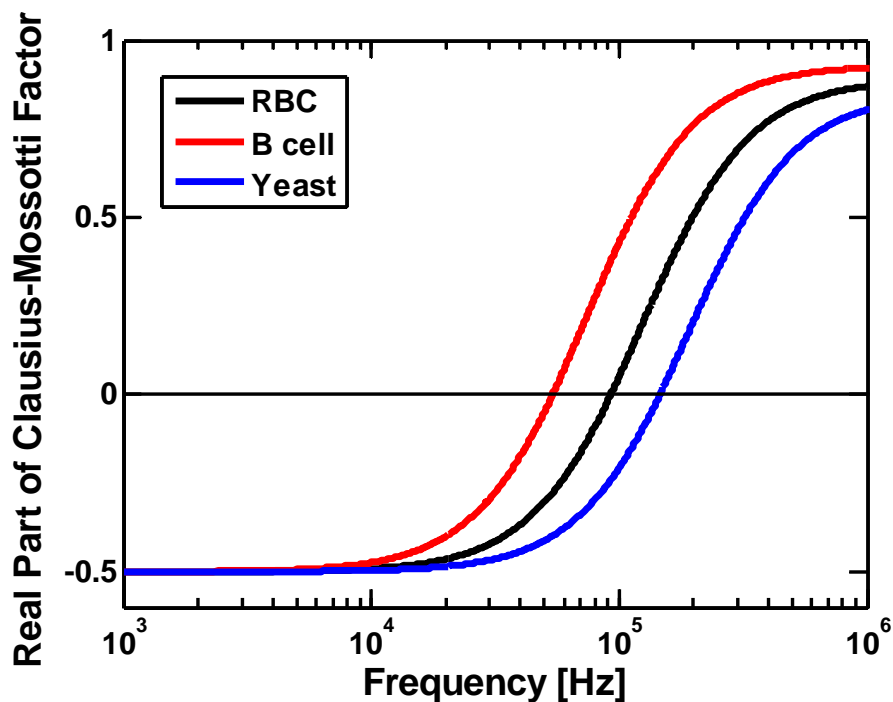


Figure 2.6 Real part of the Clausius-Mossotti factor for red blood cells (RBC), B cells (a type of white blood cell), and yeast cells.

Table 2.1 Cell parameters for the simulation shown in Figure 2.6

Cell type	Internal relative permittivity, ϵ_{int}	Internal conductivity, σ_{int} (S/m)	Membrane capacitance, C_{mem} (mF/m ²)	Radius, r (μ m)
Red blood cell (RBC) [71]	50	0.53	10	2.4
White blood cell (B cell) [72]	154.4	0.73	12.6	3.29
Yeast cell [73, 74]	50.6	0.515	7.03	2.15

2.5 Design of Optoelectronic Tweezers

Amorphous silicon is chosen for the photoconductive layer, as it is easily deposited in thin films, has high photoconductive gain, and has sufficient absorption in the visible light wavelengths (Figure 2.7). In addition, the 115-nm ambipolar diffusion length of a-

Si [68] means that the patterning of the optically-induced dielectrophoretic traps is diffraction-limited, and not limited by carrier diffusion.

As seen in Figure 2.7, the a-Si absorption changes dramatically as a function of wavelength [75]. There is a peak in absorption in the UV wavelengths, then the absorption coefficient drops as the wavelength increases. In order to fully activate the virtual electrode effects of the a-Si, the optical pattern should be absorbed throughout the entire thickness of the a-Si film. Ultraviolet wavelengths, which are strongly absorbed, will only fully modulate the impedance of an a-Si film less than 100 nm in thickness. However, if the a-Si film is too thin, then the applied voltage will cause breakdown of the thin film. Thus, the thickness of the a-Si film is kept at 0.5 μm or above to avoid breakdown effects. Typical OET devices use a-Si films with a thickness of 1 μm . This thickness of a-Si can be modulated using red or near-infrared light. White light sources may also be used to activate the OET device, although the red and longer wavelengths are the most important components of the white light source.

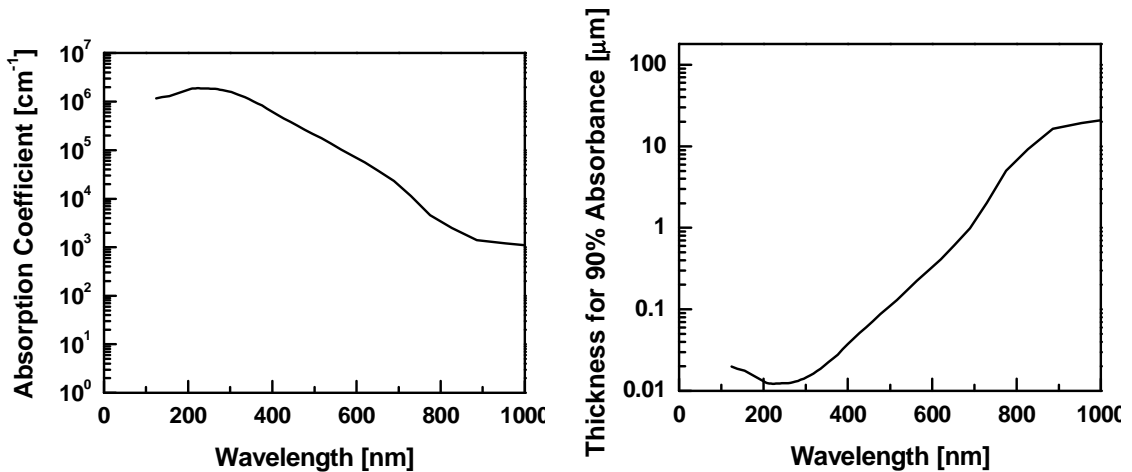


Figure 2.7 Absorption in amorphous silicon as a function of wavelength [75].

The forces induced in the OET device are sensitive to the gap between the top and bottom electrodes. This gap also defines the thickness of the liquid layer in the OET device. If the bias voltage across the electrodes is held constant as the electrode gap is decreased, the electric field strength in the OET device will increase. As a result, the induced OET force will also increase (Figure 2.8). However, the liquid layer thickness has a practical limit. A gap that is too small may cause cells to experience significant shear stresses; thus for cellular manipulation this gap should ideally be limited to 50 μm or greater.

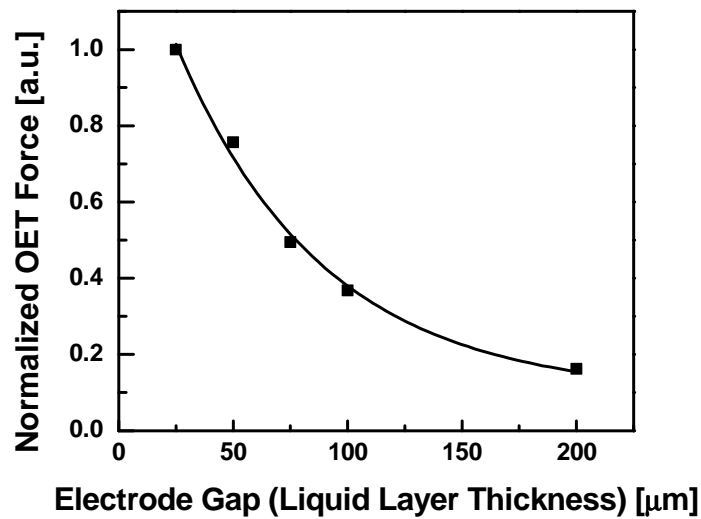


Figure 2.8 Force induced in the OET device as a function of the gap between the upper and lower electrodes.

2.6 Finite-Element Modeling

The electric field profile within the OET device is simulated using finite-element modeling software (COMSOL Multiphysics). Typical simulation parameters are shown in Table 2.2. The actual thickness of each layer of the OET device is used. However, to

reduce computation time, an area of approximately $50 \mu\text{m} \times 50 \mu\text{m}$ is modeled. The simulation model is adjusted so that there are no edge effects from this smaller simulation area.

The effect of the illumination pattern on the OET device is modeled by a change in electrical conductivity of the a-Si layer. A typical laser has a Gaussian optical profile; thus, the electrical conductivity in the a-Si layer is expressed using a Gaussian equation in the x - and y -directions (Table 2.2).

The electric field profile within the OET device is shown in Figure 2.9. The simulations show that the highest electric fields occur at the center of the Gaussian spot, where the electrical conductivity of the a-Si is highest. The highest gradients of the square of the electric field are also at the center of the optical pattern, and are proportional to the amount of OET force exerted on a particle (Figure 2.10). Furthermore, by analyzing the gradients in each direction, more physical insight can be gained from the simulations. The magnitudes of the x - and y - components of ∇E^2 are shown in Figure 2.11. The gradients in the lateral directions are strongest near the edges of the optical pattern. Thus, particles experiencing a positive OET force will be trapped near the edges of the optical pattern, if the optical pattern is larger than the particle. However, particles that are approximately the same size as the optical pattern or larger may be trapped in the center of the pattern, due to the radial symmetry of the force.

Conversely, particles experiencing a negative OET force will be repelled by the edges of the optical pattern. However, with negative OET forces, the gradient of E^2 in the z -direction significantly affects particle trapping. The z -component of ∇E^2 is strongest at the center of the optical pattern (Figure 2.12). As a result, particles exhibiting negative

OET will be levitated if they move into the central area of the optical pattern. In addition, the electric field gradients quickly decrease as the distance from the photosensitive surface is increased. Thus, the induced forces in the OET device are strongest near the photosensitive electrode surface. As negative-OET particles levitate away from the photosensitive electrode, the lateral gradient forces will be reduced, lowering the OET manipulation velocity of these particles. This is observed experimentally; particles such as polystyrene beads, which experience a negative force, can be levitated if situated in the center of an optical pattern. Levitated beads experience a greatly reduced manipulation velocity, until gravity allows the bead to settle near the photosensitive surface. This phenomenon does not occur with particles experiencing positive OET, as the z -gradient attracts the particle towards the photosensitive electrode.

Table 2.2 Simulation parameters for finite-element modeling

Parameter	Variable	Value / Expression
Relative permittivity of ITO	$\epsilon_{r,ITO}$	5
Electrical conductivity of ITO	σ_{ITO}	1×10^6 S/m
Relative permittivity of a-Si	$\epsilon_{r,aSi}$	11.7
Electrical conductivity of a-Si, dark (off) state	$\sigma_{aSi,dark}$	1×10^{-6} S/m
Electrical conductivity of a-Si, illuminated (on) state	$\sigma_{aSi,light}$	1×10^{-3} S/m (peak value) Expression for a-Si conductivity: $\sigma_{aSi,dark} + 0.001 \left(\exp\left(-\frac{2x}{(4 \times 10^{-6})^2}\right) \exp\left(-\frac{2y}{(4 \times 10^{-6})^2}\right) \right)$
Relative permittivity of glass	$\epsilon_{r,glass}$	2.09
Electrical conductivity of glass	σ_{glass}	1×10^{-14}
Relative permittivity of liquid	$\epsilon_{r,liquid}$	78
Electrical conductivity of liquid	σ_{liquid}	0.01 S/m

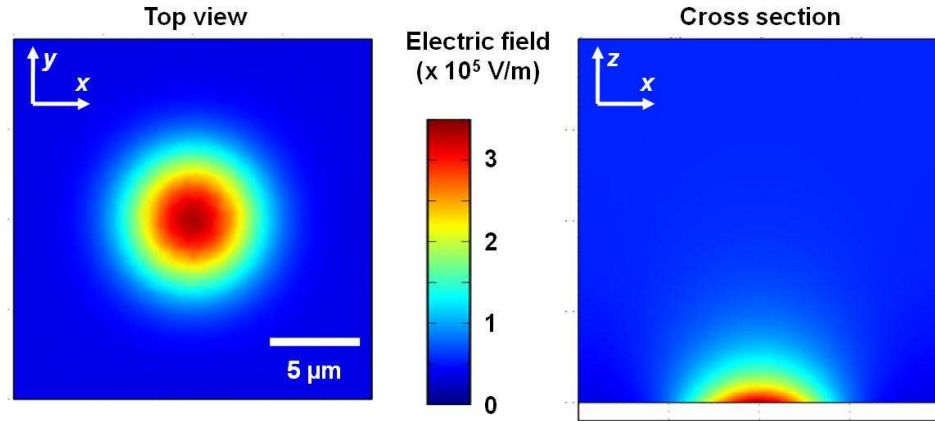


Figure 2.9 Finite-element simulation showing the electric field strength in the liquid layer of the OET device. The highest electric fields occur in the center of the optical pattern, corresponding to the areas of highest electrical conductivity in the a-Si layer.

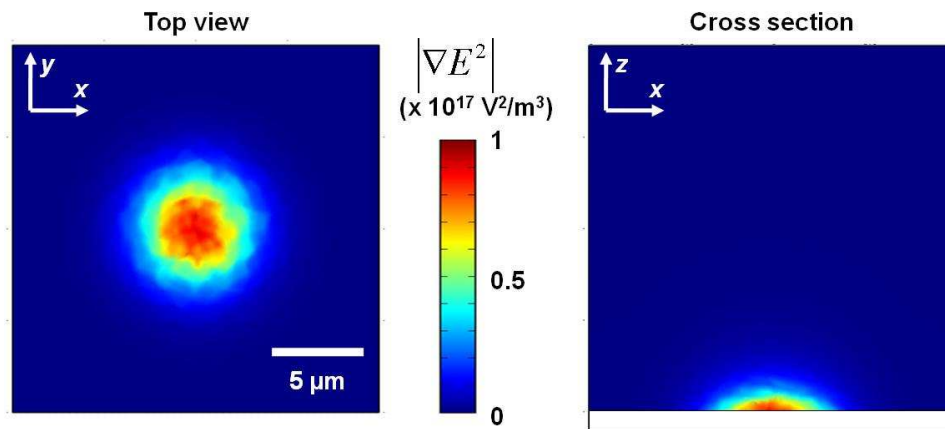


Figure 2.10 Finite-element simulation device showing $|\nabla E^2|$ in the liquid layer.

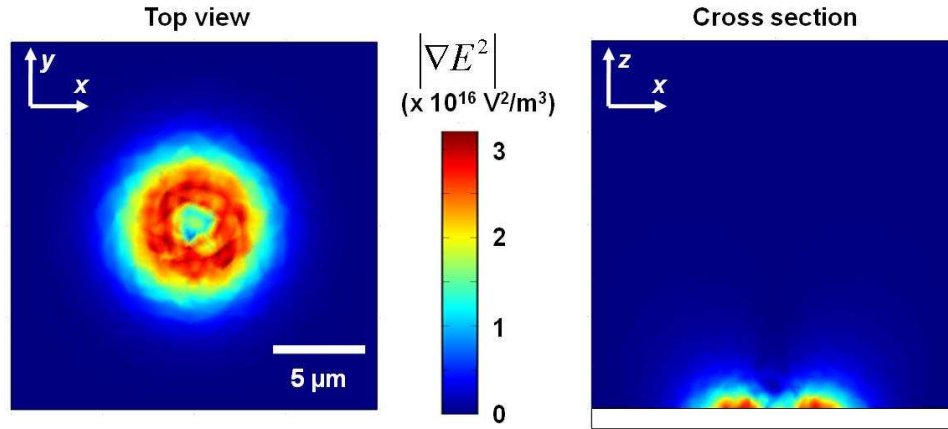


Figure 2.11 Finite-element simulation showing the x - and y -components of $|\nabla E^2|$.

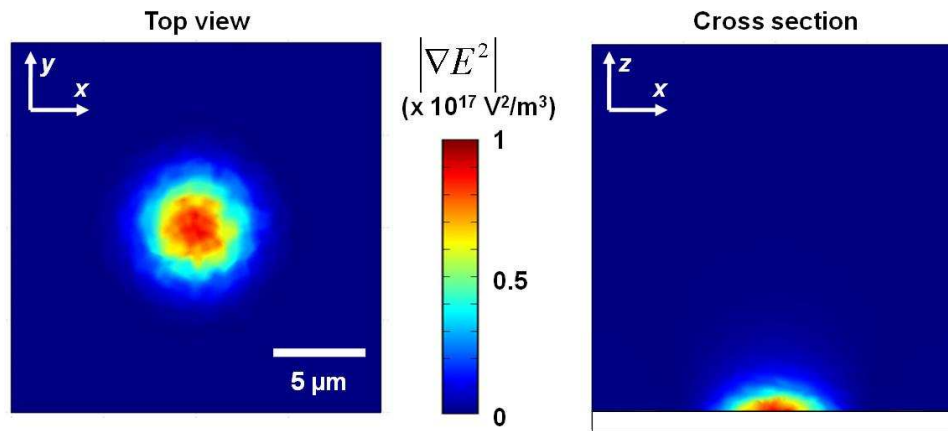


Figure 2.12 Finite-element simulation showing the z -component of $|\nabla E^2|$.

Particles experiencing a negative OET response are more effectively trapped using a ring-shaped optical pattern. A ring trap fulfills two functions on particles with a negative OET response: single particles are contained in the center of the ring, and additional particles are prevented from entering the trapping area. Ring patterns can be easily created using spatial light modulators. We have empirically determined the optical profile

of the ring trap to be that of a saturated Gaussian, which is simulated using the following equations for a-Si conductivity:

$$\sigma_{aSi} = \sigma_{aSi,dark} + \sigma_{aSi,light} \frac{1}{sat} \exp\left(-\frac{2[\sqrt{x^2+y^2}-\mu]^2}{\sigma^2}\right), \text{ if } \exp\left(-\frac{2[\sqrt{x^2+y^2}-\mu]^2}{\sigma^2}\right) \leq sat \quad (2.7)$$

$$\sigma_{aSi} = \sigma_{aSi,dark} + \sigma_{aSi,light}, \text{ if } \exp\left(-\frac{2[\sqrt{x^2+y^2}-\mu]^2}{\sigma^2}\right) > sat \quad (2.8)$$

where $\sigma_{aSi,dark}$ is the dark conductivity of the a-Si film (1×10^{-6} S/m), $\sigma_{aSi,light}$ is the peak illuminated conductivity of the a-Si film (1 mS/m for this simulation), sat is the saturation value of the Gaussian profile, μ is the distance from the center of the trap to the location of peak intensity, and 2σ is the ring width, at an intensity $1/e^2$ times the peak level. The value of sat has been empirically measured to be 0.2 if a DMD is used to create the ring trap.

The electric field profile of the ring trap is shown in Figure 2.13. In this simulation, $\mu = 5 \mu\text{m}$ and $\sigma = 1 \mu\text{m}$ in Equation 2.7, representative of a typical ring trap. The highest electric fields occur at the outer and inner borders of the ring. The highest gradients of the square of the electric field are also located at the borders of the ring pattern (Figure 2.14). Thus, particles experiencing a negative OET force will be repelled by the edges of the ring pattern. Lateral particle movement is primarily driven by the x - and y - components of ∇E^2 , the magnitudes of which are shown in Figure 2.15. However, as in the case of the single optical spot, the gradient of E^2 in the z -direction affects the trapping of particles experiencing negative OET. In the case of the ring trap, the z -component of ∇E^2 is strongest at the borders of the ring, where the strongest x - and y -directional forces also occur (Figure 2.16). However, unlike the gradients in the x - and y -directions, a significant

z -gradient exists over the area illuminated by the optical ring. Thus, if the ring trap is moved too quickly across the surface of the OET device, particles within the trap or outside of the trap can be levitated over the high electric field region defined by the optical pattern. During experiments, the ring trap should be translated at velocities less than those that cause particle levitation instead of lateral movement.

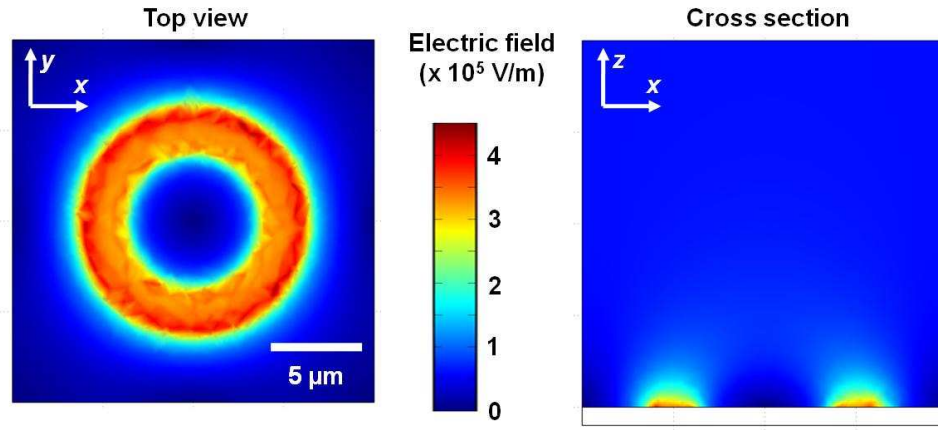


Figure 2.13 Finite-element simulation of the electric field strength in the liquid layer for a ring trap pattern. The highest electric fields occur at the borders of the ring, corresponding to the areas of highest electrical conductivity in the a-Si layer.

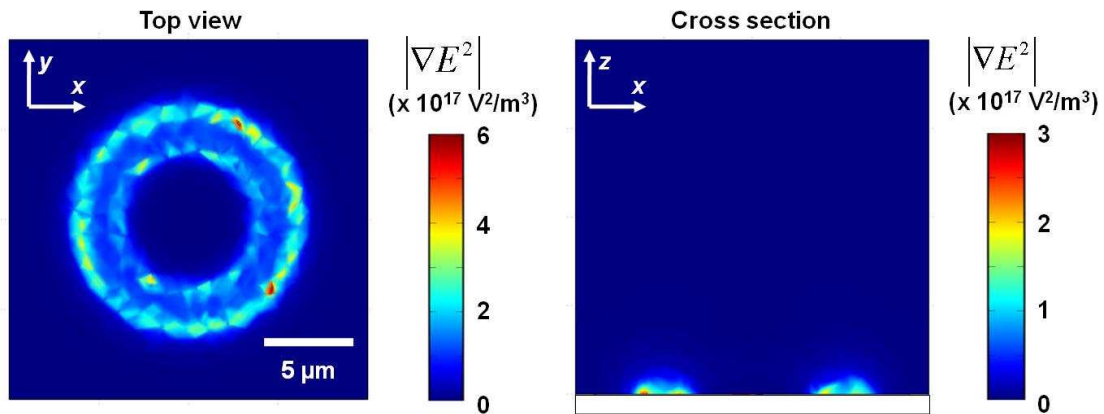


Figure 2.14 Finite-element simulation of $|\nabla E^2|$ for a ring trap. Note the intensity scale is different between the top view and cross-sectional view.

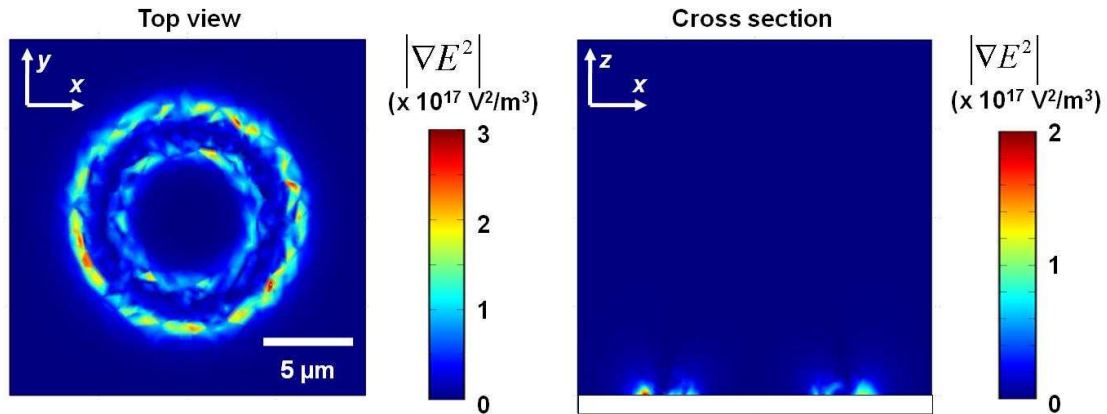


Figure 2.15 Finite-element simulation showing the x - and y -components of $|\nabla E^2|$ for a ring trap. Note the intensity scale is different between the top view and cross-sectional view.

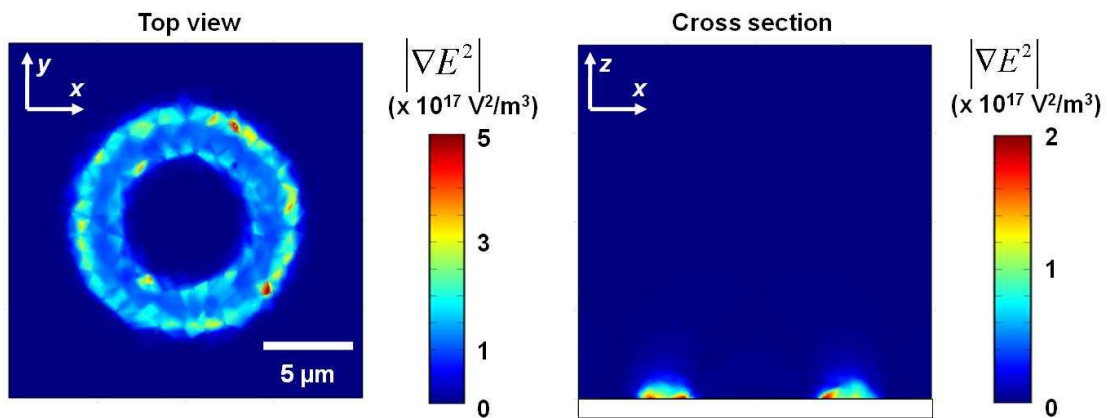


Figure 2.16 Finite-element simulation showing the z -component of $|\nabla E^2|$ for a ring trap. Note the intensity scale is different between the top view and cross-sectional view.

2.7 Fabrication of Optoelectronic Tweezers

The fabrication process of the standard OET device is suitable for low-cost mass fabrication for disposable applications. This is an advantage for biological applications, as disposable devices reduce the chances of sample cross-contamination. The basic fabrication process of the photosensitive electrode is as follows: first, ITO is sputtered

onto 1.1-mm-thick glass wafers. The a-Si photosensitive electrodes are then created by plasma-enhanced chemical vapor deposition (PECVD). Only one etch step is necessary to complete the OET device; a section of the a-Si layer is removed to create a bias pad to apply ac bias to the ITO layer. Slight variations of this process have been used with comparable results. The detailed fabrication process is outlined in Appendix 1.

Preparation of the ITO-coated glass electrode surface is the same for all variations of the OET device. Commercially-available ITO-coated glass is diced to approximately the same size as the corresponding photosensitive electrode. Silver conductive epoxy is added to the ITO-coated side of the glass, and is wrapped around the edge of the glass piece to form a conductive bias pad on the glass side of the substrate (Figure 2.17).

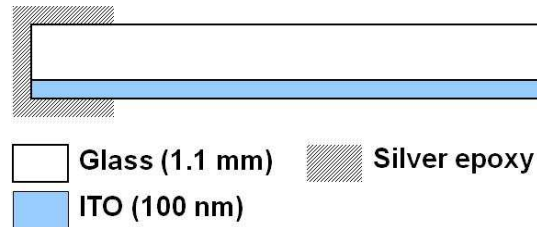


Figure 2.17 Fabrication of ITO-coated glass electrodes.

2.8 Characterization of Optoelectronic Tweezers Performance

Many variants of the standard OET device can exist. In addition, the quality of the thin films can vary between fabrication runs, although all process conditions are kept constant. Thus, it is desirable to have some metrics available to quantitatively analyze OET performance. The most useful figures of merit are the ratio of illuminated-to-dark photoconductivity of the photosensitive layer, and the maximum induced particle velocity.

2.8.1 Photoconductivity Measurements

One of the main parameters contributing to OET performance is the properties of the photoconductive film. Studying the properties of photoconductive films can also be used to identify alternate photoconductive films in addition to amorphous silicon, such as cadmium sulfide [76]. There are two properties that are of primary significance: the dark conductivity, and the illuminated conductivity. The dark conductivity should be minimized, so in the dark (off) state of OET operation the majority of the applied voltage is dissipated in the photoconductive layer. In addition, the photoconductivity should be maximized, so that the impedance of the photoconductive layer is minimized in the illuminated (on) state of OET operation, and the majority of the applied voltage is dissipated in the liquid layer.

In order to measure the dark and illuminated conductivities of the amorphous silicon film, a standard test structure is used, consisting of islands of a-Si with top aluminum contacts (Figure 2.18). The a-Si test structure is illuminated through the glass substrate with a red laser at various intensities. The illumination is focused such that the entire a-Si island under test experiences a uniform light intensity. Probes are used to contact the ITO layer and the aluminum top electrode. Using this setup, I-V curves can be extracted for various applied voltages and light intensities. This data is then used to calculate the photoconductivity of the a-Si (Figure 2.3). For the a-Si films used in these OET devices, the OET illuminated conductivity is approximately 300 times the OET dark conductivity at an illumination intensity of 1 W/cm^2 .

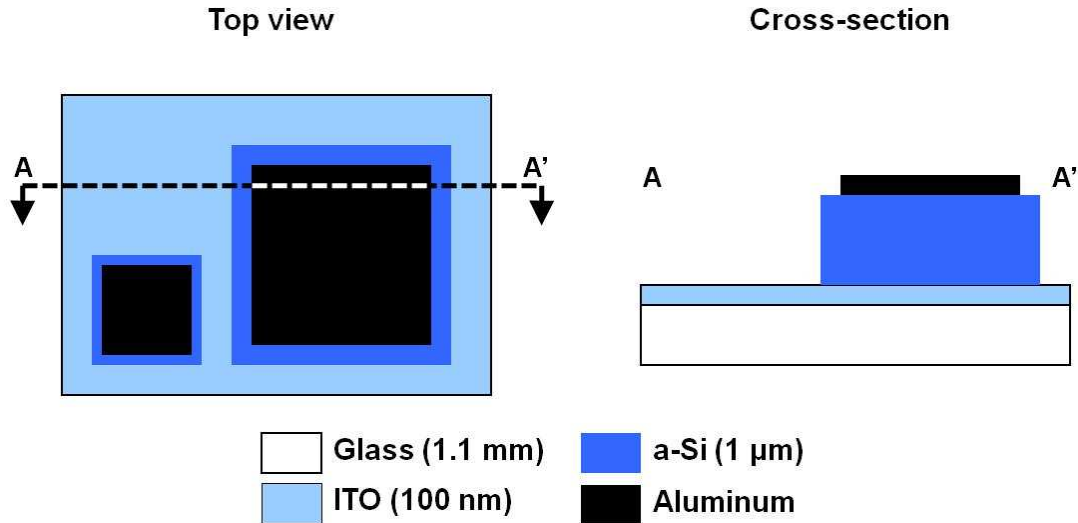


Figure 2.18 Amorphous silicon conductivity test structure.

2.8.2 Particle Velocity

Another figure of merit is the maximum velocity at which a particle can be manipulated by the OET device. Particle velocity in the OET device is a function of multiple parameters, including applied voltage, optical pattern intensity, optical pattern width, and optical pattern trap dimensions. Typically, polystyrene microbeads are used as model particles in the OET device. The polystyrene beads experience negative DEP over wide range of applied frequencies and liquid conductivities, resulting in a consistent OET operation mode for a variety of conditions. Simulations of the Clausius-Mossotti factors for polystyrene beads in liquids of different conductivities are shown in Figure 2.19. Under typical OET operating frequencies of 50 kHz to 300 kHz, the polystyrene beads experience a negative OET force. Thus, by using polystyrene beads as model particles, the effects of OET operation under different experimental conditions can be quantified. In addition, by keeping all parameters constant, the performance of the photoconductive films can be quantified.

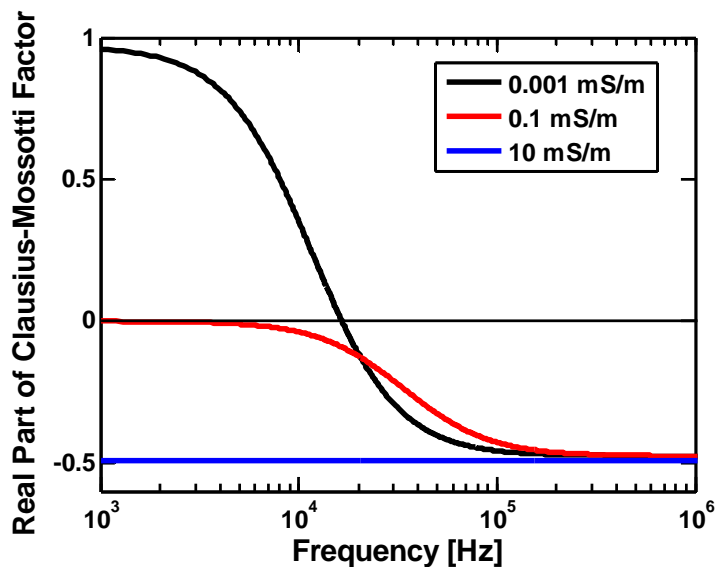


Figure 2.19 Simulation of the real part of the Clausius-Mossotti factor for polystyrene beads in solutions of varying conductivities. The polystyrene beads experience negative OET for typical OET operating frequencies (real part of the Clausius-Mossotti factor < 0).

Particle velocity is measured by translating the optical pattern, or by keeping the optical pattern stationary and translating the OET device, by moving the microscope stage. In the latter case, a motorized microactuator (Newport LTA-HL) is used to provide a constant stage velocity.

The following data provides a baseline for comparing particle velocity [51]. The test setup consists of an LED source and a DMD spatial light modulator. The image from the DMD is focused onto the OET device using a 10x objective lens (N.A. = 0.3). A red LED source (Luxeon Star/O, $\lambda = 625$ nm) provides an optical intensity of 1 W/cm^2 . The maximum manipulation velocity of 20- μm -diameter polystyrene beads is measured as a function of several factors. In steady-state, the OET force is balanced by the viscous drag of the fluid, which is related to the velocity of a spherical particle by Stokes' Law:

$$F = 6\pi r \eta v \quad (2.9)$$

where r is the radius of the particle, η is the viscosity of the fluid, and v is the velocity of the particle. Thus, Stokes' Law can be used to calculate the OET force on a particle, based upon empirical velocity measurements.

As expected, the induced velocity increases as the applied voltage is increased (Figure 2.20). Increasing the applied voltage translates into a sharper electric field gradient, increasing the DEP force (see Equation 2.3). However, DEP forces are typically proportional to the square of the applied voltage; our results show a more linear relationship. We have also found that particle velocity is dependent on the linewidth of the manipulation pattern, a phenomenon that is unique to our manipulation technique (Figure 2.21). The trends observed in Figure 2.20 and Figure 2.21 can be attributed to the tendency of polystyrene particles to levitate vertically, due to the vertical gradient of the electric field (Figure 2.12). As a result, particle velocity increases more slowly as a function of voltage than predicted with simplified DEP force models.

As the optical patterns are swept across the manipulation area, particles move in both the lateral and vertical directions to the electric field gradients. Furthermore, as the applied voltage is increased, both the lateral and vertical gradients increase proportionally. However, in the case of these experiments, an increase in the vertical gradient is undesirable. The increased vertical gradient will result in increased particle levitation, which reduces the lateral force induced on a particle. As a particle is levitated away from the a-Si surface, the lateral field gradient decreases, resulting in reduced lateral forces. Similarly, a pattern with a narrow linewidth cannot be moved very rapidly before a particle's tendency to levitate causes it to rise over the potential "wall" created

by the pattern's corresponding electric field. However, this problem is alleviated by utilizing wider linewidth patterns. It may also be possible to reduce this effect by using a smaller spacing between the top and bottom OET surfaces.

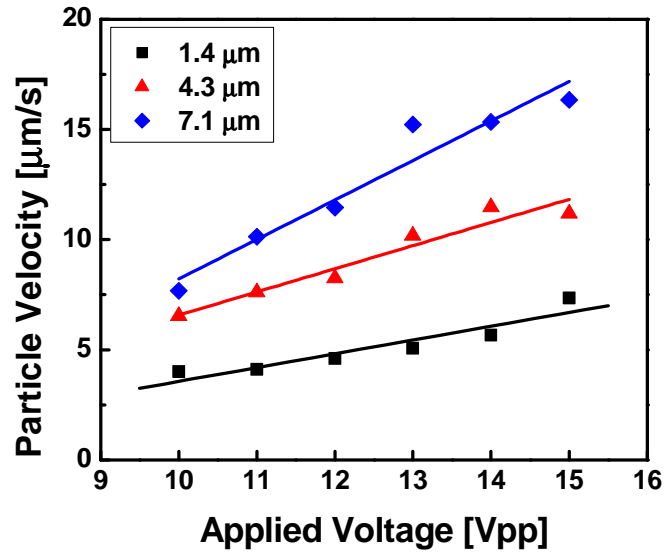


Figure 2.20 Induced velocity of 20- μm -diameter polystyrene beads as a function of applied voltage at 100 kHz for several illumination pattern widths [51].

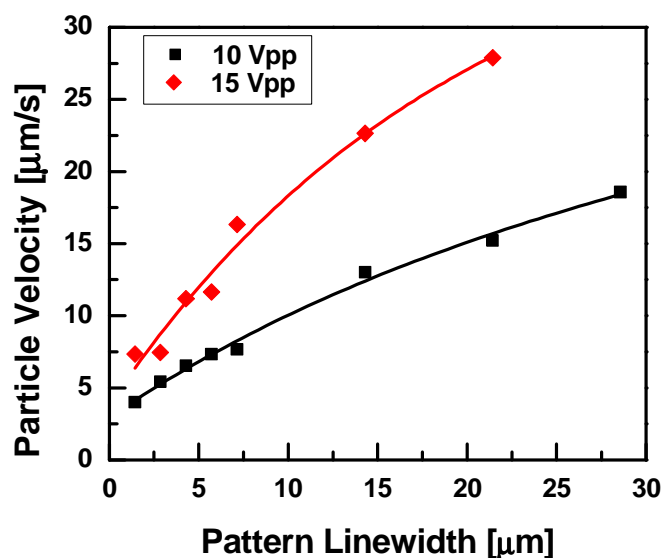


Figure 2.21 Induced velocity of 20- μm -diameter polystyrene beads as a function of the illuminated linewidth of the manipulation pattern [51]. The lower curve is for an applied bias of 10 Vpp at 100 kHz; the top curve is for a bias of 15 Vpp at 100 kHz.

2.9 Other Effects in Optoelectronic Tweezers Devices

In addition to dielectrophoresis, there are other phenomena that can affect micro- and nanoparticle motion within the OET device. Some of these forces are parasitic, while others can be exploited to expand the operational capabilities of the OET device.

2.9.1 Electrolysis

Electrolysis is the breakdown of water molecules into hydrogen and oxygen gas due to an electric current. This is undesirable in the OET device, as the bubble formation can rupture cell membranes and interfere with OET operation. In addition, if the bubble formation process is violent enough, the a-Si film can crack, or pinholes can form. Electrolysis in the OET device occurs more easily under DC bias or under an AC bias

frequency of 1 kHz or lower. To avoid electrolysis, the OET devices are usually operated at AC frequencies of 10 kHz or greater.

2.9.2 Electrothermal Heating

Another undesirable effect is electrothermal heating, as elevated temperatures can cause cell death or even boiling of the liquid media. The electrothermal heating is caused by phonon generation in the a-Si layer or joule heating in the a-Si and liquid layers [77]. As a result, gradients in the electrical conductivity and permittivity of the liquid media arise, resulting in a liquid flow. Phonon generation is dependent on incident optical power, whereas joule heating is dependent upon the conductivity and electric field within the material, as given by:

$$W = \sigma E^2 \quad (2.10)$$

where W is the power generated per unit volume, and σ is the conductivity of the material. However, these effects are only significant under high optical intensities (greater than 100 W/cm^2) [77]. Alternatively, the heat generation due to optical absorption can also be used to induce other operational modes in the OET device (discussed in Chapter 9).

2.9.3 Buoyancy Effects

Increasing the temperature of a liquid also affects the liquid density. Thus, temperature gradients in the liquid result in density gradients that can drive fluidic flows under the influence of gravity. However, this effect does not become significant with optical intensities of less than 10^4 W/cm^2 , which is well within the operating parameters of the OET device [77].

2.9.4 Light-induced AC Electro-osmosis (LACE)

Light-induced AC electroosmosis (LACE) is another operational regime of the OET device, typically occurring at low bias frequencies of approximately 1 kHz. The LACE effect is an optically-patterned control of fluid flow in the OET device, and has been used to trap polystyrene beads with diameters of 2 μm down to 50 nm, λ -phage DNA molecules, and quantum dots [78].

Electroosmosis is fluid flow driven by the interaction of an electric field in the liquid layer and ions in the electric double layer. The electric field generates enough force to drive the ions at a slip velocity given by the Helmholtz-Smoluchowski equation [79]:

$$v_{slip} = -\frac{\varepsilon\zeta E_t}{\eta} \quad (2.11)$$

where v_{slip} is the slip velocity, ε is the permittivity of the liquid, ζ is the zeta potential at the interface of the liquid and the OET electrode, E_t is the tangential component of the electric field, and η is the viscosity of the liquid. Electroosmotic flows are typically used for microfluidic pumps, driven either with a DC electric field [80, 81] or an AC electric field [82].

When inducing LACE in the OET device, there exists an optimal applied frequency to obtain the highest boundary slip velocity. If the applied frequency is too high, the impedance of the electric double layer capacitance is low, resulting in most of the applied voltage being applied across the liquid and photosensitive layers. In this case, LACE effects are negligible, and optically-induced DEP will occur. Conversely, if the applied frequency is too low, the impedance of the electric double layer capacitance will be high, creating a large voltage drop in the double layer, which screens the electric field in the liquid layer. This results in a low electric field in the liquid, and a small value of the

tangential electric field, lowering the slip velocity. Thus, an optimal frequency condition is given by [78]:

$$f_{opt} = \frac{1}{2\pi RC} = \frac{1}{2\pi} \frac{\sigma \lambda_d}{\varepsilon L} \quad (2.12)$$

where σ is the conductivity of the liquid, ε is the permittivity of the liquid, λ_d is the thickness of the double layer, and L is the thickness of the liquid layer. Assuming typical OET parameters, i.e. $L = 100 \mu\text{m}$, $\sigma = 10 \text{ mS/m}$, $\lambda_d = 10 \text{ nm}$, the calculated f_{opt} is 229 Hz [78]. However, the experimentally observed f_{opt} (1 to 10 kHz) is higher, since device geometries have not been factored into Equation 2.12.

2.9.5 Figure-of-Merit for OET Forces

A figure of merit has been developed to quantify the contribution of these other effects relative to the strength of the optically-induced DEP force [77]. This is expressed as a ratio, β :

$$\beta = \frac{X_{DEP}}{X_{DEP} + X_{EXT} + \langle X_{BROWNIAN} \rangle} \quad (2.13)$$

where X_{DEP} , X_{EXT} , and $\langle X_{BROWNIAN} \rangle$ represent the distance a particle travels in 1 s due to optically-induced DEP, all other external forces, and Brownian motion, respectively. If β is averaged over an area, a new figure of merit is obtained:

$$B = \frac{1}{A} \int_A \beta dx dy, \quad x \in [-r, r], y \in [0, d] \quad (2.14)$$

where r is the maximum radius from the center of the optical pattern within which particle perturbation is expected, d is the thickness of the liquid layer, and A is the area of integration, where $A = 2rd$. Thus, B represents the percentage of particle perturbation in the OET device due to optically-induced DEP. For applied bias frequencies of greater

than 50 kHz and optical intensities of less than 100 W/cm² (typical OET operating parameters), optically-induced DEP is indeed the dominant force (Figure 2.22) [77].

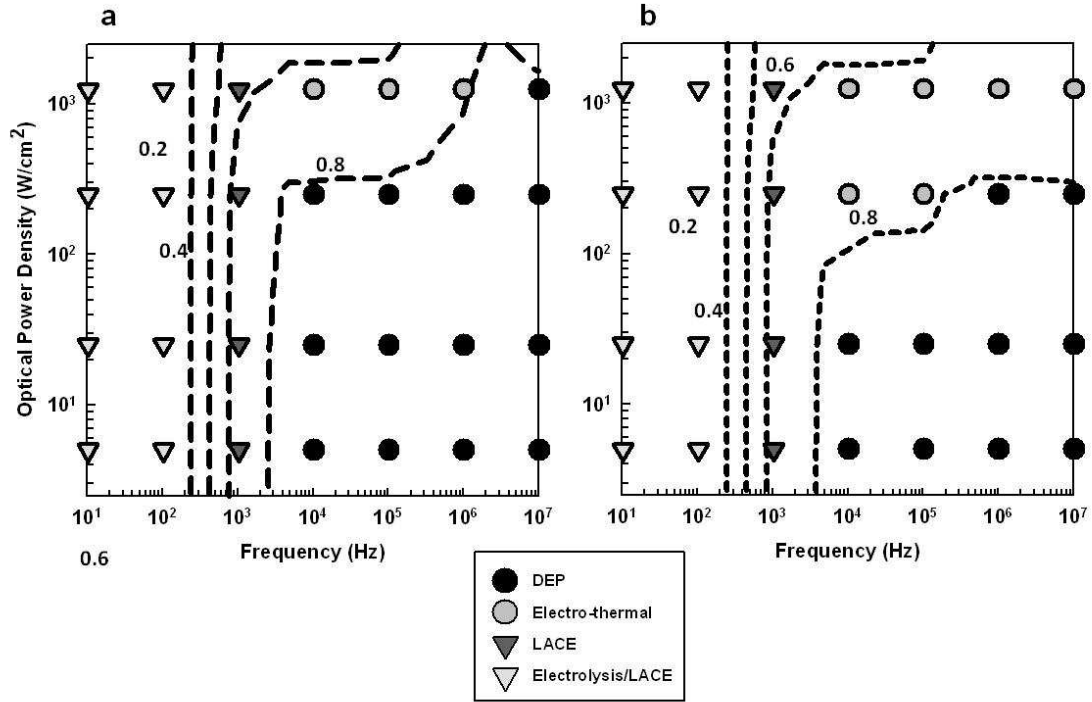


Figure 2.22 Dominant effects in the OET device [77]. Theoretical simulations are shown as dashed lines, and empirically-determined effects are shown as data points. The liquid solution has a conductivity of 1 mS/m. The applied voltage is at a frequency of 100 kHz, with amplitudes of (a) 20 Vpp and (b) 10 Vpp.

Chapter 3 Manipulation of Cells

3.1 Motivation

Optoelectronic tweezers is a powerful tool for biological research. Traditionally, biologists have studied cell behavior by observing the bulk response of a population of cells. However, single-cell studies yield insight into phenomena such as cell-cell interactions, cell signaling pathways, mutations or genetic damage among a population, or the differentiation of stem cells. OET is capable of manipulating specific single cells in parallel, enabling single-cell studies. However, cell manipulation using OET is more challenging than the manipulation of polystyrene beads. Here, issues involved in the manipulation of mammalian cells are discussed, along with the implemented solutions. We then demonstrate OET manipulation for the patterning of cell arrays, and the OET-based separation of live and dead cells, as well as cells of different types.

3.2 Issues with Cellular Manipulation

The two main factors that make cellular manipulation using OET more challenging than the manipulation of polystyrene beads are: 1) the high conductivity of cell culture

media and buffers; 2) the non-specific adhesion of cells to the OET surfaces. The solutions to these issues are presented here.

3.2.1 Media Conductivity and Osmotic Pressure

The media used for cell cultures and physiological buffers has a high concentration of ions such as Na^+ , Cl^- , K^+ , Ca^{2+} , Mg^{2+} , and SO_4^{2-} in order to provide osmotic balance for the cells and necessary inorganic chemicals. As a result, these media have high electrical conductivities. For example, a common culture medium, Dulbecco's Modified Eagle Medium (DMEM), has an electrical conductivity of 1.5 S/m. Another common buffer solution, phosphate-buffered saline (PBS), also has an electrical conductivity of 1.5 S/m.

As discussed in Chapter 2.3, the OET device has a relatively low illuminated (on-state) photoconductivity. At reasonable illumination intensities of 10 W/cm^2 or less, the maximum photoconductivity of the a-Si is approximately 2 mS/m, which is lower than that of cell culture media. This means that the OET device cannot fully switch the applied voltage to the liquid layer, and even in the illuminated state, the virtual electrode will remain off. A limited degree of OET manipulation in culture media may be obtained by further increasing the intensity of the optical patterns beyond 10 W/cm^2 ; however, this leads to non-desirable parasitic effects such as electrothermal heating, as discussed in Chapter 2.9. The a-Si photoconductivity is limited by the large number of defects in the thin film, resulting in a large density of carrier traps and a low carrier mobility. While this is beneficial for creating high-resolution optically-defined traps, the low carrier mobility limits practical OET operation to low-conductivity solutions.

Fortunately, the restriction to low-conductivity solutions does not preclude cellular manipulation in the OET device. Bacterial cells or other cells with cell walls are rigid

enough to withstand suspension in low-conductivity media. Furthermore, mammalian cells and other cells without cell walls can be suspended in osmotically-balanced low-conductivity isotonic solutions. We utilize an isotonic buffer consisting of 8.5% sucrose and 0.3% dextrose for our experiments involving mammalian cells (hereafter referred to simply as “isotonic solution”).

One advantage of using low-conductivity media is that the polarity of OET force is opposite for live cells versus dead cells. As a result, OET can be used to separate live cells from dead cells. This capability is described further in Chapter 3.7 and Chapter 4.

However, the usage of low-conductivity media also has drawbacks. It can be difficult to estimate effect of the non-physiological conditions for cell behavior studies. In addition, prolonged exposure to low-conductivity media can cause the loss of normal cellular functions and reduce cell viability. The timeframe in which deleterious effects from the low-conductivity media appear vary among different cell types, and can range from 2 hours to over 24 hours.

An alternative OET device that is capable of operation in high-conductivity solutions has also been developed. This device, called phototransistor-based OET (Ph-OET) uses single-crystal silicon as a photoconductive material in order to increase the carrier mobility [59]. In addition, as the name suggests, Ph-OET employs a vertical phototransistor structure to decrease dark (off-state) conductivity, while increasing the illuminated (on-state) conductivity by the phototransistor gain. While this device shows great potential for manipulating cells in their native culture media, separation between live and dead cells is more complicated, as both live and dead cells will experience a negative OET force in highly-conductive media.

3.2.2 Non-Specific Cell Adhesion

The non-specific adhesion of cells is a well-known issue in biomedical devices [83], and is also a concern in OET devices. The fabrication of OET devices is simple enough to allow OET devices to be used as single-use, disposable devices, eliminating the cross-contamination concerns of unwanted cell adhesion. However, cellular adhesion, especially among mammalian that adhere to surfaces in order to proliferate, is still significant during a single OET manipulation experiment (Figure 3.1). Many types of mammalian cells tend to adhere to charged hydrophilic surfaces, a condition which is present in the OET device, as the a-Si surface has a native oxide present at the a-Si/liquid interface. Adherent cells are capable of attaching to surfaces with forces on the order of nanonewtons, while OET produces forces in the tens to hundreds of piconewtons. Thus, it is necessary to passivate the surface of the OET device in order to prevent the undesirable adsorption of cells.

3.3 Surface Treatments for Optoelectronic Tweezers

In order to avoid cell adhesion, the surfaces of the OET device need to be modified to be hydrophilic and uncharged. Furthermore, the passivation layers must be non-conductive, to avoid shorting out the optically-defined virtual electrodes of the photosensitive electrode. At the same time, the non-conductive layers should be thin, in order to avoid any parasitic voltage drops across the passivation layers. Two types of surface treatments that fulfill these requirements have been used to prevent non-specific cell adhesion.

In order to test the quality of the anti-adhesion coatings, adherent HeLa endothelial cells (a cervical cancer cell line) were used to quantify the prevalence of nonspecific cell

adhesion. The HeLa cells, suspended in isotonic solution at a density of approximately 1×10^6 cells/mL, were introduced into the OET device in 20 μL aliquots. Attempts to move all cells within the microscope field-of-view (0.027 mm^2) were made using a 0.8-mW HeNe laser to actuate the OET device. Cells that exhibited movement as a result of the induced OET force were counted as “free” cells, while cells that did not have observable movement were counted as adhered cells. Five distinct fields-of-view were tested for each time point; at each time point, at least 30 cells were tested. The measurements were repeated on 5 different OET devices. On the standard OET devices, the initial percentage of free cells was only $20 \pm 21\%$, decreasing to $3 \pm 4\%$ after one hour (Figure 3.1).

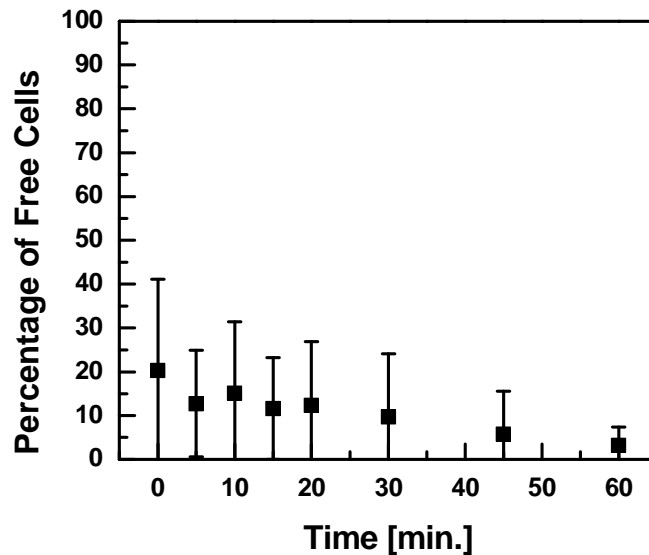


Figure 3.1 Percentage of live HeLa cells that can be transported under OET manipulation in standard OET devices. Non-specific cell adhesion limits the reliability of OET manipulation of mammalian cells. The error bars indicate the standard deviation of the measurements.

3.4 Teflon / Bovine Serum Albumin Surface Treatment

One method to achieve an adhesion-resistant surface is to coat it with bovine serum albumin (BSA), a protein found in the bloodstream of cows. Very thin layers of BSA protein can be created, making it suitable for use in the OET device.

Some proteins have a hydrophobic end and a hydrophilic end. Thus, to create an uncharged, hydrophilic coating, the hydrophobic end of the protein should be made to bond to the device surface. The a-Si surface is hydrophilic due to the native oxide; thus, to create a hydrophobic layer, a thin, 50-nm-thick layer of Teflon is coated on the photoconductive surface of the OET device by spin coating 0.2% Teflon AF[®] (diluted with perfluoro-(2-perfluoro-n-butyl)tetrahydrofuran) at 1500 rpm for 30 seconds. The Teflon-coated devices are cured at 150°C on a hotplate for 20 minutes, and then immersed in a solution of 0.1% BSA in DI water. The hydrophobic ends of the protein bind to the Teflon, creating a protein layer. The devices are removed after 30 minutes to 1 hour, and carefully dried with a nitrogen gun.

The same measurements of the percentage of free cells described in Chapter 3.3 were repeated on 5 different BSA-coated OET devices (Figure 3.2). The initial percentage of free cells was $88 \pm 7\%$, decreasing slightly to $82 \pm 15\%$ after one hour. However, when the BSA-coated OET devices were rinsed once using DI water, parts of the BSA coated were washed away, resulting in increased cell adhesion. In addition, certain areas of the OET surface had a high incidence of cell adhesion, evidenced by the large standard deviations.

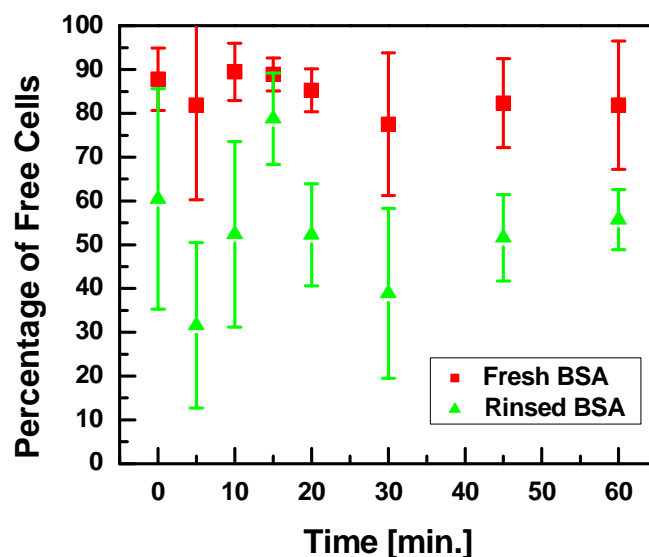


Figure 3.2 Percentage of live HeLa cells that can be transported under OET manipulation in BSA-coated OET devices. Non-specific cell adhesion is greatly reduced by using this passivation technique. However, rinsing the devices results in increased non-specific adhesion. The error bars indicate the standard deviation of the measurements.

3.5 Poly(ethylene glycol) Surface Treatment

Another type of passivation was explored for cell manipulation using OET. The gold standard of non-fouling surface coatings for biomedical devices is poly(ethylene glycol) (PEG), a polymer hydrogel [83]. PEG is based on a repeating unit of ethylene glycol, and has the following structure: $\text{HO}-(\text{-CH}_2\text{CH}_2\text{-O-})_n\text{-H}$. This surface has been shown to have an excellent resistance to protein and cell adsorption, reducing the amount of biofouling by more than 90% [83]. The model for the nonfouling properties of PEG is based on entropic repulsion and osmotic pressure; as the PEG hydrogel is hydrated, the PEG chain swells and excludes cells and proteins from the PEG surface (Figure 3.3) [84, 85]. In order to achieve a high-quality nonfouling surface, a high surface density of

grafted PEG chains is required. The PEG chains should be dense enough that the distance between grafted chains is approximately less than or equal to the radius of gyration of a hydrated PEG chain [86].

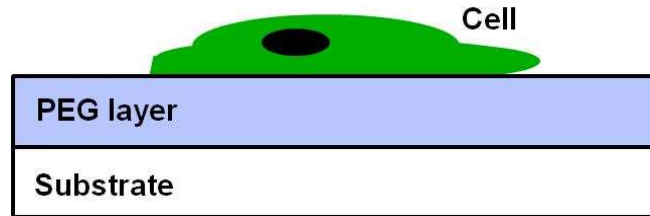


Figure 3.3 Poly(ethylene glycol) (PEG) polymer chains resist cell and protein adhesion via entropic repulsion and osmotic pressure.

We have developed a process for creating a thin, non-fouling PEG coating on the electrode surfaces of the OET. These surface-modified non-fouling OET devices provide a 30-fold increase the amount of cells that can be moved using OET forces.

The procedure for coating the OET electrodes with PEG was developed in collaboration with researchers from Applied Biosystems. To coat the photosensitive electrodes with PEG, the a-Si surface is first coated with a 10-nm-thick layer of SiO₂ using PECVD. The SiO₂ layer provides a surface that can be silanized to provide adhesion of the PEG polymer chains. The silanol groups on the SiO₂ layer are enhanced by a series of chemical washes. The electrodes are then brought into direct contact with a solid-phase PEG silane, (2-[methoxy(polyethyleneoxy)propyl]trimethoxysilane) and heated at 65°C, allowing the PEG silane to melt and coat the surface of the photosensitive electrode.

The process for the ITO-coated glass electrodes is similar. First, the hydroxyl end groups on the ITO surface are enhanced through a series of chemical washes. The

electrodes are then coated with PEG using the same PEG silane process described above. The detailed fabrication process for both the a-Si and ITO-coated electrodes is given in Appendix 2.

The resistance to protein adsorption of the PEG-coated OET devices was verified by x-ray photoemission spectroscopy (XPS) measurements. The XPS measurements are performed at the Molecular Foundry facility of the Lawrence Berkeley National Laboratories, using a Physical Electronics PHI 5400 XPS tool, which was equipped with an aluminum x-ray source. The measurement area of each sample is approximately 0.5 mm x 0.5 mm.

A standard OET device and a PEGylated OET device were both exposed to a solution of 0.1% laminin protein. The XPS spectrum of the a-Si electrode shows the presence of oxygen, nitrogen, and carbon from the adsorbed proteins (Figure 3.4a). Silicon from the a-Si film is also present, suggesting the PEG layer is thin, as desired. The PEG-coated a-Si electrode also has oxygen and carbon present due to the PEG layer, but it lacks a nitrogen peak, indicating the absence of adsorbed laminin proteins (Figure 3.4b). The carbon/oxygen (C/O) ratio of the PEG-coated a-Si electrode is 1.63. An ideal PEG layer has a C/O ratio of 2; however, the C/O ratio of the measured device may be lower due to the presence of the SiO₂ layer.

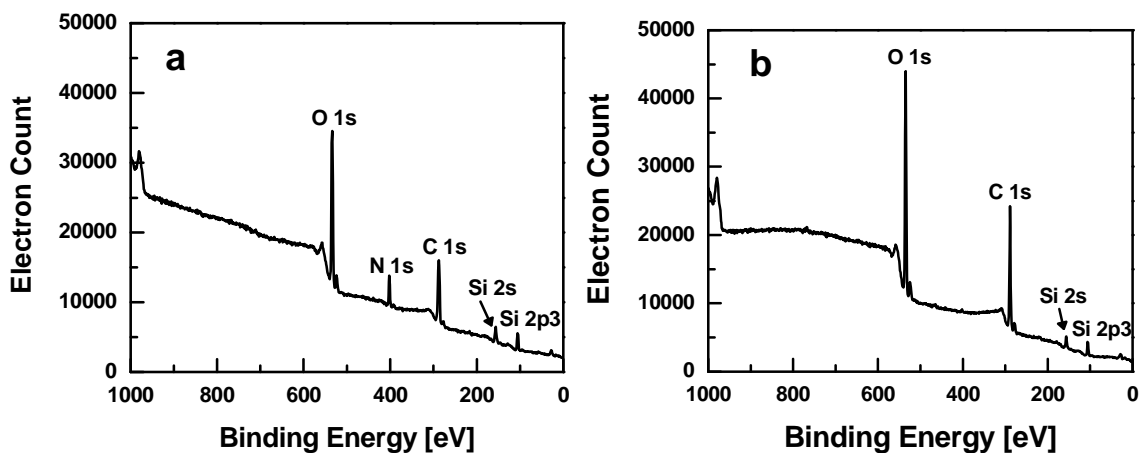


Figure 3.4 XPS measurements of laminin adsorption on the a-Si electrode of an OET device. (a) Standard a-Si electrode. (b) PEG-coated a-Si electrode. The absence of an N 1s peak in this spectrum is an indicator of the resistance to protein adsorption.

The XPS spectrum of the ITO electrode shows similar results as the a-Si electrode. Again, the spectrum shows the presence of oxygen, nitrogen, and carbon from the adsorbed proteins (Figure 3.5a). As expected, indium and tin are also present, due to the ITO film. The PEG-coated ITO electrode also has oxygen and carbon present due to the PEG layer, but it lacks a nitrogen peak, indicating the absence of adsorbed laminin proteins (Figure 3.5b). The C/O ratio of the PEG-coated ITO electrode is 1.55, which is again lower than the ideal C/O ratio. However, the C/O ratio may be affected by the oxygen content of the ITO film.

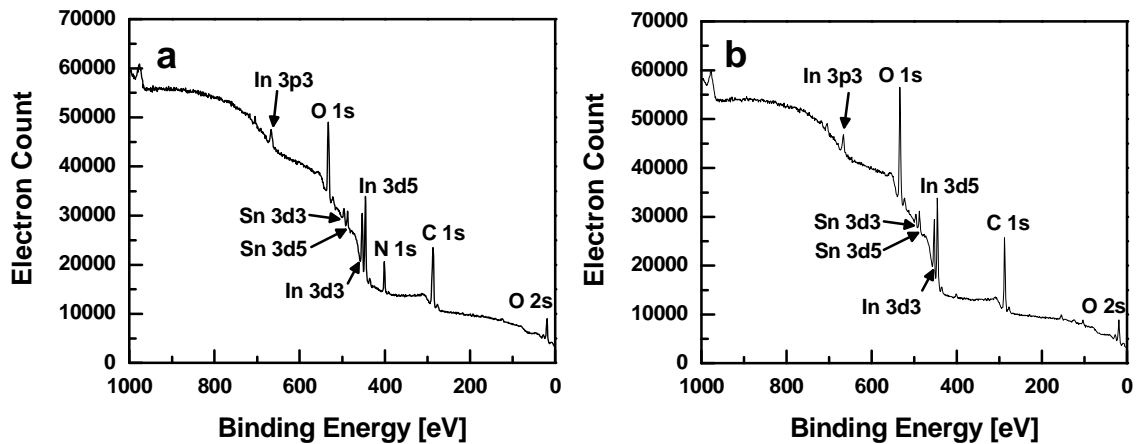


Figure 3.5 XPS measurements of laminin adsorption on the ITO electrode of an OET device. (a) Standard ITO electrode. (b) PEG-coated ITO electrode. The absence of an N 1s peak in this spectrum is an indicator of the resistance to protein adsorption.

In addition to the XPS data, the same measurements of the percentage of free cells described in Chapter 3.3 were repeated on 5 different PEG-coated OET devices (Figure 3.6). The initial percentage of free cells was $97 \pm 5\%$ on the PEG-coated OET devices. After one hour, $91 \pm 8\%$ of the cells remained responsive to OET manipulation. The PEG-coated OET devices increase the reliability of OET manipulation on live adherent cells by 30 times compared to an uncoated OET device. Thus, the PEG coating is the most effective passivation layer to avoid non-specific cell adhesion in the OET device. In addition, the PEG-coated devices are more robust than the BSA-coated devices. Figure 3.7 shows the results of the HeLa adhesion experiments on different surfaces for comparison.

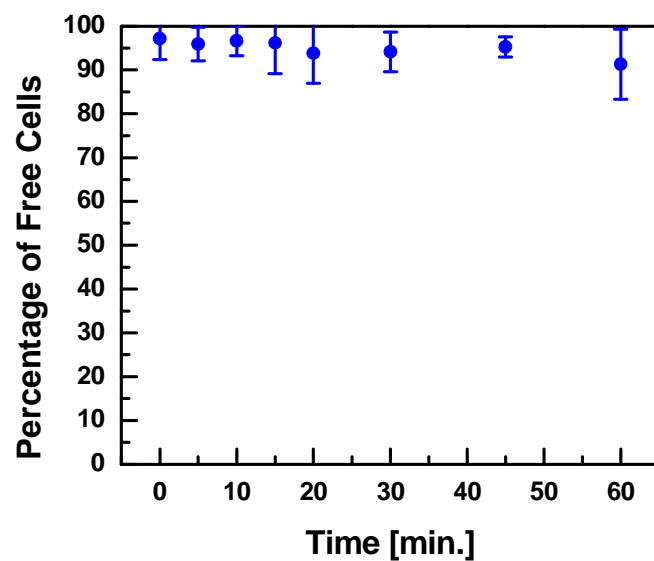


Figure 3.6 Percentage of live HeLa cells that can be transported under OET manipulation in PEG-coated OET devices. Non-specific cell adhesion is reduced 30 times by this passivation technique. The error bars indicate the standard deviation of the measurements.

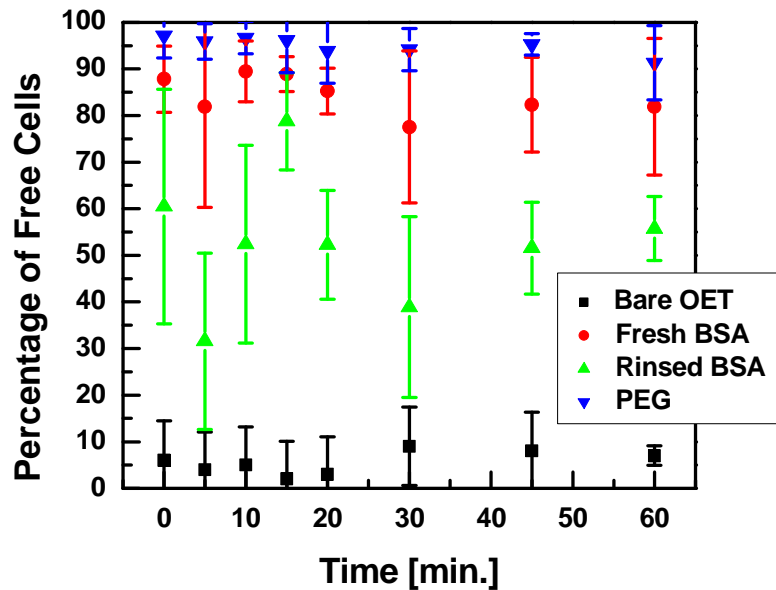


Figure 3.7 Comparison of the percentage of live HeLa cells that can be transported under OET manipulation in various OET devices. The PEG coating provides the most robust coating, and the most reliable OET manipulation. The error bars indicate the standard deviation of the measurements.

3.6 Cell Patterning

The reliable OET manipulation of single cells on PEG-coated devices can be used to spatially arrange live cells in arbitrary patterns. This type of manipulation is not possible on untreated OET devices, as non-specific cell adhesion is too prevalent.

Here, we use OET manipulation to assemble Jurkat cells into a cell array (Figure 3.8). The optical manipulation patterns are generated using a 635-nm laser and a liquid-crystal SLM, in a setup similar to Figure 1.6a. However, in this case, the manipulation patterns are created under direct user control.

Furthermore, multiple cell types can be trapped and transported using OET manipulation. This is demonstrated with live fluorescent-labeled Jurkat cells and

unlabeled HeLa cells (Figure 3.9). Each cell type can be identified via fluorescent microscopy, and subsequently trapped and transported under OET manipulation. Thus, the original random distribution of the two cell types can be organized into segregated patterns for further single-cell study (Figure 3.9d).

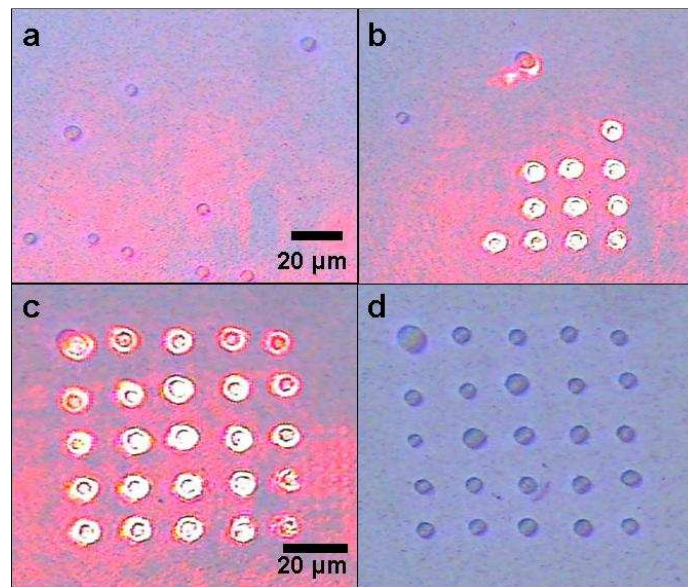


Figure 3.8 Formation of an array of live Jurkat cells on a PEG-coated OET device. (a, b) The original randomly-distributed cells are trapped and transported using OET manipulation patterns. (c) A 5 x 5 individually-addressable cell array is formed. (d) The same array, with the the OET manipulation pattern temporarily shut off for cell imaging clarity.

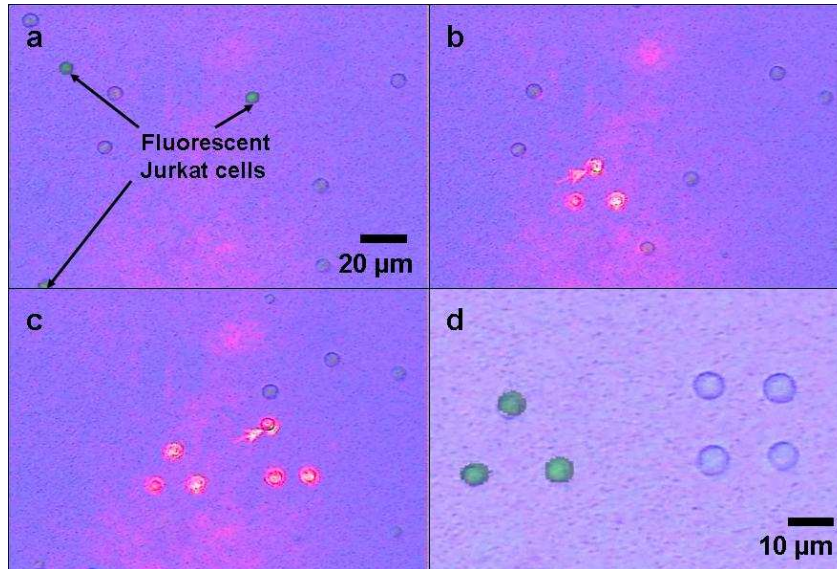


Figure 3.9 OET spatial manipulation of multiple cell types. (a) The fluorescent-labeled Jurkat cells are distinguished from the unlabeled HeLa cells (composite image). (b) The Jurkat cells are arranged in a triangular pattern. (c) The HeLa cells are arranged in a square pattern. (d) Fluorescent imaging verifies that the cell types are segregated (composite image).

3.7 Separation of Live and Dead White Blood Cells

As described in Chapter 2.4, dielectrophoretic force is a function of the frequency-dependent electrical properties of the cells under manipulation. As different cell types exhibit dissimilar electrical properties, DEP can be used to sort between cell types, or even between widely varying cells of the same type [34, 35, 37]. This property is useful for cellular manipulation, in which heterogeneous mixtures of cells are common. We have used this capability to selectively concentrate live human B cells from dead B cells [50].

In a live cell, the semi-permeable phospholipid membrane allows a cell to maintain an ion differential between its interior and the surrounding liquid medium. As mentioned in Chapter 3.2.1, OET experiments use cells that are suspended in a low-conductivity

isotonic buffer of 8.5% sucrose and 0.3% dextrose. Thus, live cells have internal conductivities greater than the liquid conductivity. However, once a cell dies, the membrane becomes permeable to ions. The ion differential is no longer maintained, and the conductivity of the cell interior becomes similar to that of the surrounding liquid. This means that the Clausius-Mossotti factor is different for live and dead cells. The real part of the Clausius-Mossotti factor for a human B cell was calculated, using the single-shell model of the cell, as described in Equations 2.5 to 2.6 (Figure 3.10). To determine the Clausius-Mossotti factor of dead B cells, it is assumed that the internal permittivity and conductivity of the cell is equal to that of the surrounding media, while all other parameters remain constant. The simulated results predict that for applied frequencies greater than approximately 60 kHz, live B cells will experience a positive OET force, while dead B cells will experience a negative OET force.

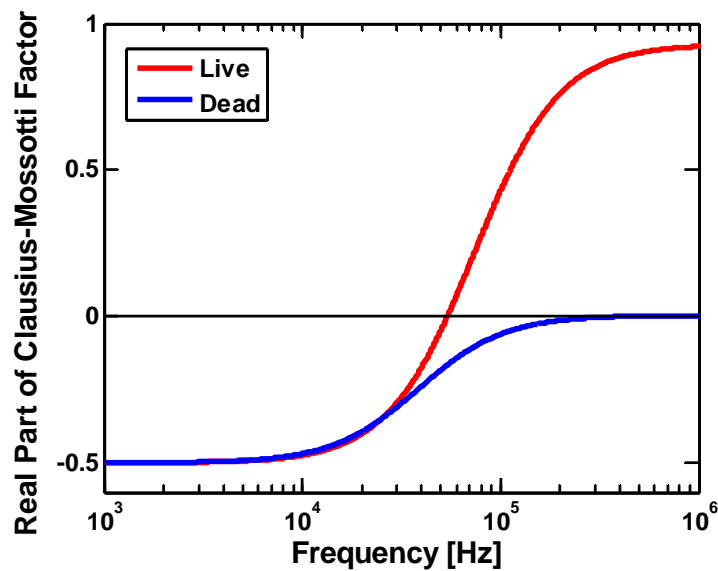


Figure 3.10 Real part of the Clausius-Mossotti factor for live and dead B cells.

The difference in DEP response between live and dead B cells is used to selectively concentrate live B cells at an applied frequency of 120 kHz. The selective collection pattern is a series of broken concentric rings (Figure 3.10). The pattern is created using the DMD, and illumination is provided by a 100-W halogen lamp. As the concentric rings shrink, the live cells are focused to the center of the pattern by positive OET. In contrast, the dead cells experience negative OET, and slip through the gaps in the ring patterns. The B cells are suspended in isotonic solution, with 0.4% Trypan Blue dye. The Trypan Blue dye identifies live and dead cells; live cells exclude the dye, and appear clear. The dead cells, which have a permeable membrane, absorb the dye, and appear dark. The experiment is performed immediately after the addition of the Trypan Blue dye, as the dye is toxic, and will increase the amount of dead cells in the sample.

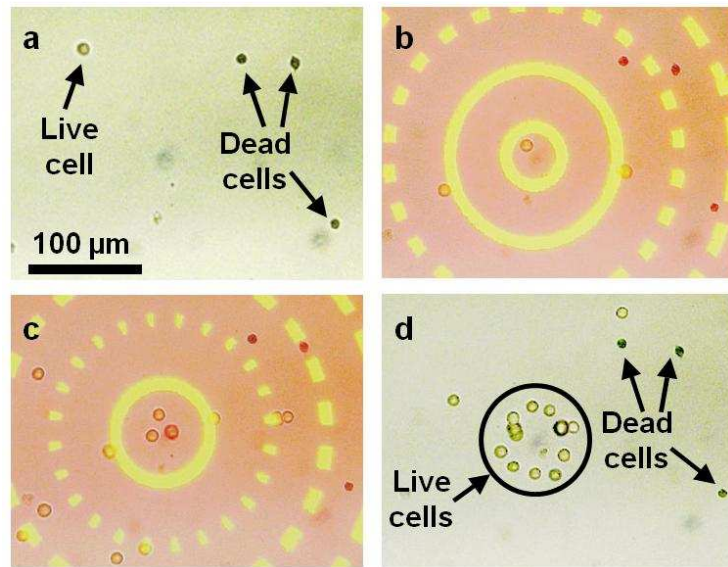


Figure 3.11 Selective concentration of live B cells from dead B cells [50]. (a) Initial positions of live (clear) and dead (dark) B cells. (b, c) A broken concentric ring pattern is used to transport the live cells to the center of the field-of-view while leaving the dead cells behind. (d) Live cells have been concentrated to the central region of the optical pattern.

3.8 Separation of Live Jurkat and HeLa Cells

In addition to differentiating between live and dead cells, OET force can be used to discriminate between different cell types. This ability is demonstrated through the spatial discrimination of live Jurkat and HeLa cells using OET [52].

In this experiment, cultured Jurkat cells were labeled with a green fluorescent dye. The labeled Jurkat cells and cultured HeLa cells are washed with isotonic buffer, re-suspended in isotonic solution, and mixed together. The concentration of the mixed solution is approximately 5×10^5 cells/mL. Culture media was added to adjust the conductivity of the cell solution to approximately 2 mS/m. A 20- μ L aliquot of cell solution was introduced into the OET device for manipulation. The cells experience a positive OET force, and are attracted towards the optical manipulation patterns.

The maximum OET manipulation velocity of Jurkat and HeLa cells as a function of the frequency of the applied voltage was empirically determined (Figure 3.12) [52]. The manipulation velocity is proportional to OET force. At an applied voltage of 10 V_{pp} at 100 kHz, sufficient variation in the OET force exists to differentiate between the two cell types.

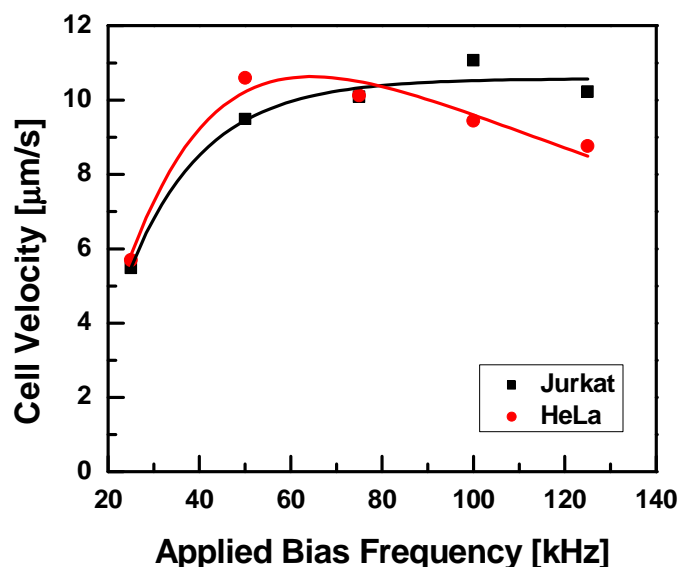


Figure 3.12 OET-induced manipulation velocity of different cell types as a function of the frequency of the electric field [52]. Cells are manipulated using a 15- μm -wide scanning line pattern.

In order to spatially separate the HeLa and Jurkat cells, a scanning line optical pattern is used to exploit the differences in OET force on the cells (Figure 3.13). The scanning lines are produced using the DMD and an LED source (Luxeon Star/O, $\lambda = 625 \text{ nm}$) that provides an optical intensity of 1 W/cm^2 . A 15- μm -wide leading line and a 23- μm -wide trailing line are separated by approximately 40 μm , and are simultaneously scanned at a rate of 13 $\mu\text{m/s}$. The thinner leading line produces a weaker OET force than the thicker trailing line, as the manipulation velocity of cells exhibits a dependence on the width of the optical pattern (Figure 3.14). Thus, as the two lines are scanned across the OET device, the Jurkat cells, which experience a stronger OET force, are held by the leading line (Figure 3.13b, c). The leading line does not produce sufficient force to transport the HeLa cells against the viscous drag, which are subsequently attracted to and transported

by the trailing line (Figure 3.13c). After the scan is completed, the cells retain a spatial separation equal to the spacing of the two scanning lines.

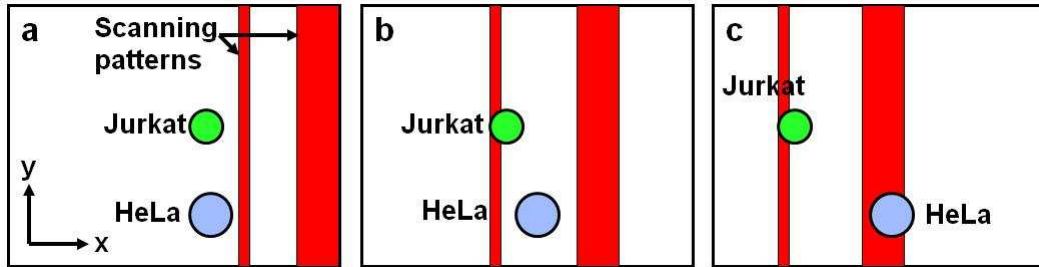


Figure 3.13 Optical pattern for OET-enabled cell discrimination [52]. (a) Cells before the lines are scanned in the negative x -direction. The thin leading line produces a weaker OET force than the thicker trailing line. (b) As the pattern is scanned, the Jurkat cells have a sufficiently OET strong force to be retained by the leading line, while the HeLa cells do not experience sufficient force. (c) The trailing line provides enough force to transport the HeLa cells, while the Jurkat cells continue to be retained by the leading line, achieving spatial discrimination.

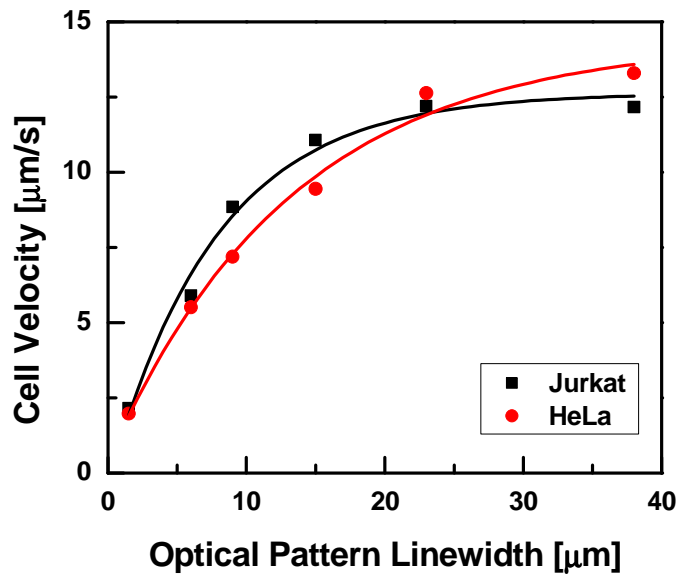


Figure 3.14 The OET manipulation velocity of Jurkat and HeLa cells as a function of the width of the optical pattern [52].

The results of the optical line scanning on a mixed population of Jurkat and HeLa cells are shown in Figure 3.15. An initial group of both cell types is present (Figure 3.15a). As the scanning pattern moves from right to left across the field of view, the Jurkat cells are transported by the 15- μm leading line (Figure 3.15b). The HeLa cells are transported only slightly by the leading line pattern, and cannot maintain the velocity of the translated leading line. The 23- μm trailing line then attracts and transports the HeLa cells. Scanning of the line patterns was repeated twice to achieve the desired separation between the Jurkat and HeLa cells. After the third scan, the two cell types are spatially separated (Figure 3.15c). A second HeLa cell is also visible, which moved into the field-of-view during the scanning of the optical pattern. Using fluorescent imaging, it is verified that the cells on the leading line pattern are the fluorescent-labeled Jurkat cells (Figure 3.15d). In this image, the unlabeled HeLa cells do not appear.

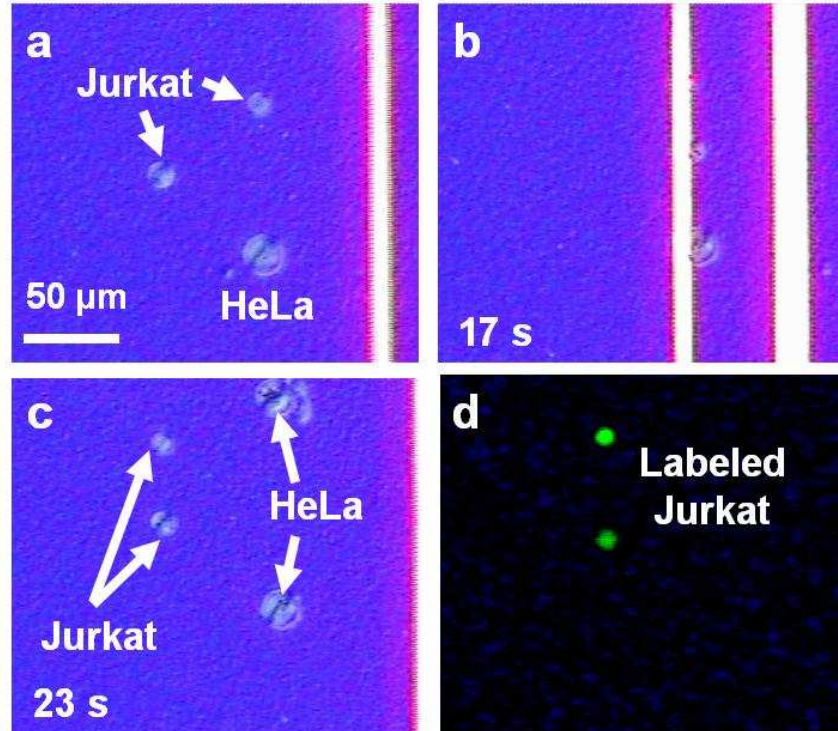


Figure 3.15 OET-enabled spatial discrimination of live Jurkat and HeLa cells [52]. (a) Initial cell positions before the optical pattern is scanned from right to left across the field-of-view. (b) Cells are attracted to the leading line. The HeLa cell is starting to lag the scanning line. (c) Cells showing spatial separation after the scan is completed. An additional HeLa cell has moved into the field-of-view during the scan. (d) Fluorescent image of the cells in (c), verifying that the leading cells are the fluorescent-labeled Jurkat cells.

Chapter 4 Sperm Sorting for *in vitro* Fertilization

4.1 Motivation

Assisted reproductive technology (ART) is used to treat 35 to 70 million couples worldwide [87]. In the United States, the Centers for Disease Control and Prevention (CDC) estimate that more than 1% of US births are attributed to ART [88].

Up to 50% of the cases at infertility clinics are due to male infertility [89, 90]. Male fertility problems include low sperm counts and/or concentration, low sperm motility, and abnormal sperm morphology. One treatment that is available for patients with low sperm counts and/or low sperm motility is intracytoplasmic sperm injection (ICSI) [91]. This procedure entails directly injecting an entire sperm into an egg's cytoplasm using a micropipette. Since the introduction of ICSI in 1992, this procedure has rapidly gained acceptance; as of 2005, ICSI is used in 60% of the ART cases in the US [88].

A major concern of the ICSI procedure is that the natural sperm selection mechanisms are bypassed during fertilization. Thus, it is imperative that healthy viable

sperm are selected for the ICSI procedure. The selection of viable sperm for ICSI is challenging and relies primarily upon sperm motility [92, 93]. However, motility-based sperm selection methods are ineffective on samples with reduced sperm motility (asthenozoospermia). Furthermore, asthenozoospermic samples for ICSI are not limited to patients with reduced sperm motility in fresh ejaculate. Typical *in vitro* fertilization techniques use previously-frozen sperm samples from patients. Upon thawing of the sample, previously-motile sperm can be rendered non-motile. Fortunately, even in samples with complete asthenozoospermia (no motile sperm), up to 50% of the non-motile sperm remain viable [94, 95]. In these instances, it is desirable to analyze the viability of the available non-motile sperm.

Current sperm viability assays are limited by subjectivity, sensitivity, and potential toxicity. The Trypan Blue dye exclusion test is a gold-standard cell viability assay, but its toxicity precludes using sperm exposed to Trypan Blue for ICSI. Another dye-based assay, eosin-nigrosin staining, involves an air-drying step which renders the tested sperm unavailable for further use [96]. A potentially non-damaging assay is the hypo-osmotic swelling test [94, 97, 98]. This assay has been successfully used to increase the fertilization rate of eggs *in vitro* [99]. However, the collection of viable sperm is still performed manually. As a result, sperm in typical ICSI procedures are still subjectively selected by a technician based on morphology.

Optoelectronic tweezers can provide a method of distinguishing between live and dead cells (see Chapter 3.7), which is applicable to selecting viable non-motile sperm. In addition, viable sperm that is identified using OET can be collected in parallel, and transported off-chip for use in ICSI procedures. Here, the OET response of live non-

motile sperm and dead sperm are quantified, showing a clear distinction in OET-induced force. In addition, we demonstrate that the OET manipulation procedure does not induce DNA damage to the cells under manipulation, which is an important concern if the sperm are to be used for *in vitro* fertilization.

4.2 Experimental Setup

PEG-coated OET devices, as described in Chapter 3.5, were used to manipulate sperm samples. OET actuation was provided by a 10-mW, 635-nm diode laser, focused onto the OET surface using a 10× objective lens (Figure 4.1). The output of the laser is attenuated, resulting in an intensity of 40 mW/cm² incident upon the OET device. The laser is incident from the glass substrate underneath the a-Si layer; thus, the sperm sample is further screened from the actuation laser by the absorption of the light in the a-Si layer.

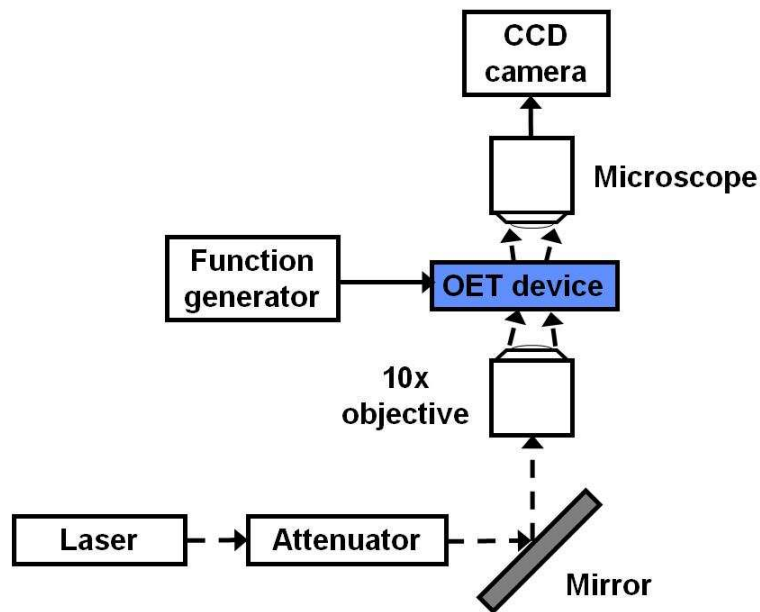


Figure 4.1 Setup of the OET device for sperm manipulation.

Fresh ejaculate specimens from 6 healthy males were evaluated using OET (Figure 4.2). The adequacy of each specimen was confirmed by the presence of motile sperm in the sample, indicating viability. In order to determine the viability of non-motile cells, the samples were mixed in a 1:1 volume ratio with 0.4% Trypan Blue dye in DI water, and incubated at room temperature for 3 minutes. The sperm/Trypan mixture was then diluted approximately 100 times by adding isotonic solution. The conductivity of the diluted sperm solution was adjusted to be 6.5 mS/m for all samples.

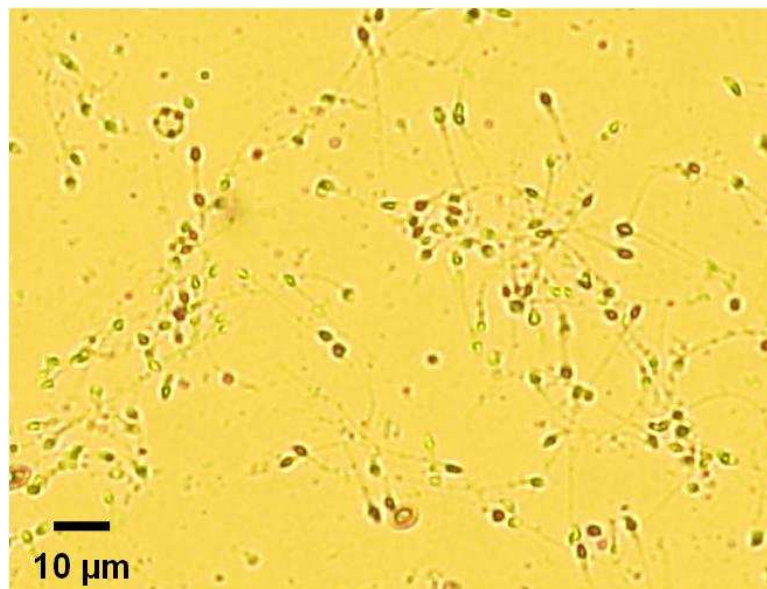


Figure 4.2 Sperm samples for OET manipulation.

A 20- μ L aliquot of the Trypan-stained sperm sample was pipetted into the PEG-coated OET devices. Over a 15-minute period, 55 distinct sperm were evaluated from each donor. As a positive control, five motile sperm were trapped using OET, verifying that a positive OET response was induced on these viable sperm. The OET-induced velocity of 25 non-motile sperm that excluded the Trypan Blue dye was also evaluated. These sperm are live, but non-motile. In addition, the OET-induced velocity of 25 dead

sperm was measured. Here, dead sperm refer to the cells that experienced negative OET or no OET response. Most of these sperm were stained by Trypan Blue (Trypan Blue positive), although a few were not stained (Trypan Blue negative). All velocity measurements were done using an applied bias of 9 Vpp at 100 kHz.

4.3 OET Response of Live Non-Motile Sperm and Dead Sperm

A total of 330 individual sperm from the 6 donors were assayed. All (100%) of the motile sperm visualized in each specimen were Trypan Blue negative, and all of those assayed (N=25) experienced positive OET. All (100%) sperm experiencing positive OET were Trypan Blue negative (N=150). The Trypan-Blue-positive sperm demonstrated either no response (54%) or a weak repulsive response (46%) to the OET manipulation pattern. A few Trypan-Blue-negative sperm (15%) demonstrated no response to OET actuation, suggesting that these sperm are also dead.

The velocity measurements on the live non-motile sperm and dead sperm are shown in Figure 4.3. The average velocity of live non-motile sperm in the OET device is $8.0 \pm 3.9 \mu\text{m/s}$, averaged over 150 cells from 6 separate donors. The average velocity of dead sperm is $-1.0 \pm 1.2 \mu\text{m/s}$ with the negative value indicating a negative OET force. The dead Trypan-Blue-positive sperm exhibited some variability in their OET response, exhibiting either weak negative OET (54%) or no response to the OET pattern (46%). However, no Trypan-Blue-positive sperm exhibited a positive OET response. Thus, these results show a clear separation of the cell subpopulations.

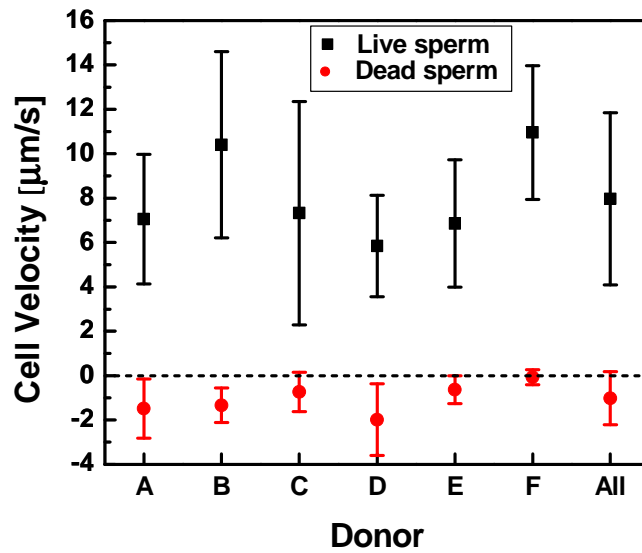


Figure 4.3 OET-induced velocities of live non-motile sperm and dead sperm. The error bars indicate the standard deviation of the measurements. “All” refers to sperm velocities averaged across all 6 donors.

4.4 Characterization of DNA Damage on Sperm

We have demonstrated the OET capability of distinguishing between live and dead non-motile sperm, but if OET is to be used for *in vitro* fertilization, we must also establish that the OET manipulation process is gentle enough to avoid inducing DNA damage on sperm. The DNA fragmentation of sperm is measured using the Comet assay.

An PEG-coated OET device with a microfluidic chamber was used in the Comet assay experiments. The microfluidic chamber measures 1 cm x 1 cm x 100 μm, and allows the introduction and removal of the test samples using syringe pumps. Six separate test samples were prepared from a single semen sample. The test samples consist of: 1) the fresh ejaculate sample (“pure sample”); 2) sperm suspended in a 1:100 dilution of the pure sample to isotonic solution, and flushed through the OET device (“isotonic

sample”); 3) sperm in isotonic solution that are exposed to an applied bias of 10 Vpp at 100 kHz and an optical pattern at an intensity of 80 mW/cm² for 30 s (“low dose sample”); 4) a sample similar to the low dose sample, except the applied bias is increased to 20 Vpp at 100 kHz (“high dose sample”); 5) pure sample that has been incubated in a UV oven for 15 minutes (“UV sample”); 6) pure sample that has been heated in a water bath at 50°C for 5 minutes (“Heat sample”).

The results of the Comet assay show that a very low level of DNA fragmentation is present in the pure and isotonic samples, as expected (Figure 4.4). Most significantly, no increase in DNA fragmentation is observed for the samples that underwent OET manipulation, either at a low dose or a high dose. The UV-treated sample surprisingly showed little DNA fragmentation, but the heat-treated sample provided a positive control, as DNA fragmentation was evident (inset). Thus, OET manipulation should provide viable cells after sorting operations are performed.

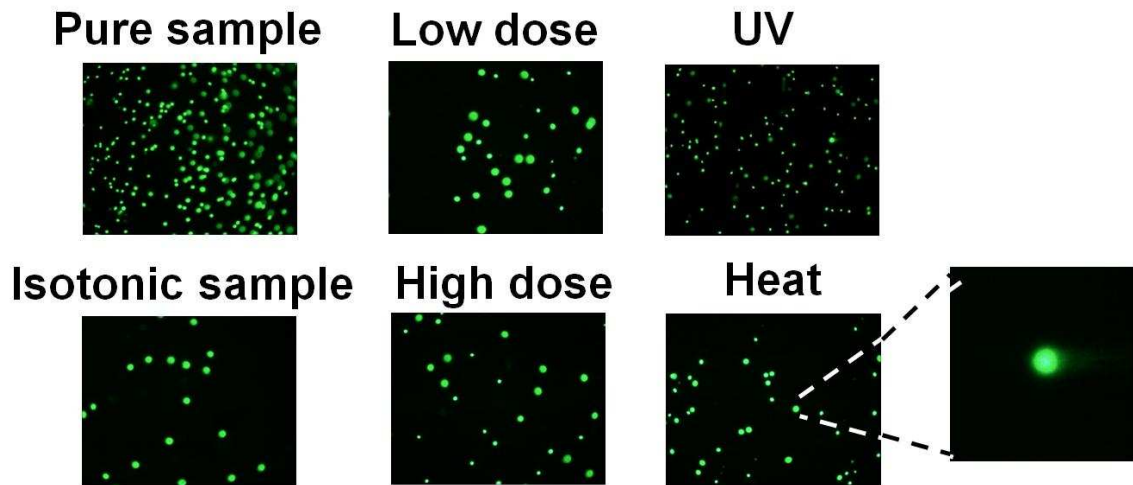


Figure 4.4 Comet assay on OET-manipulated sperm under different conditions. Similar levels of DNA fragmentation is evident in the pure control sample and the samples manipulated using OET (low dose and high dose). DNA fragmentation is present in sperm that was heated to 50°C for 5 minutes (inset).

4.5 Future Work

We have demonstrated that OET is capable of non-invasively identifying, assessing, and sorting viable live non-motile sperm from non-viable sperm, without introducing DNA damage on the cells under manipulation. However, the experiments presented here were performed with fresh ejaculate; it will also be interesting to repeat the experiments using frozen samples to more closely simulate clinical IVF procedures.

In addition, an optimized microfluidic setup is being integrated with the PEG-coated OET devices to enable more efficient sample retrieval of the sorted cells. Concurrently, our collaborators at the University of California, San Francisco are developing an animal model to test ICSI fertilization using OET-sorted sperm.

Chapter 5

Lateral-Field Optoelectronic Tweezers (LOET)

5.1 Motivation

Although optoelectronic tweezers is a highly flexible, versatile device, certain limitations exist. The electric field in the OET device is created in a liquid layer between two planar electrodes (Figure 5.1), thus, both electrodes must be in contact with the liquid for the device to operate. As a result, OET cannot be integrated with devices that do not provide a conductive planar surface.

In addition, anisotropic objects such as microdisks, nanowires, and *E. coli* bacteria align normal to the plane of the electrodes in the OET device (Figure 5.2a) [57, 58, 60]. This is due to the torque exerted on the induced dipole of the particle in response to the electric field (Figure 5.2b). Thus, if an application (such as creating nanowire interconnects) requires the OET device to assemble anisotropic objects such that their major axis is parallel to the device surface, the primary electric field direction needs to be altered.

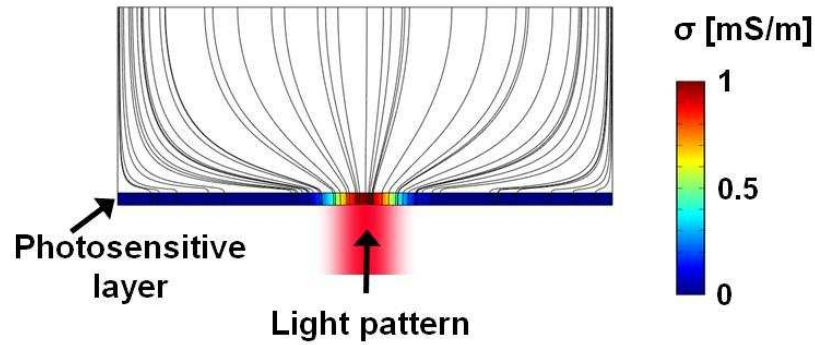


Figure 5.1 Electric field in the OET device. The color gradient shows the conductivity gradient in the a-Si layer, generated by illuminating the photoconductor. Note that the primary direction of the electric field is normal to the plane of the photosensitive electrode.

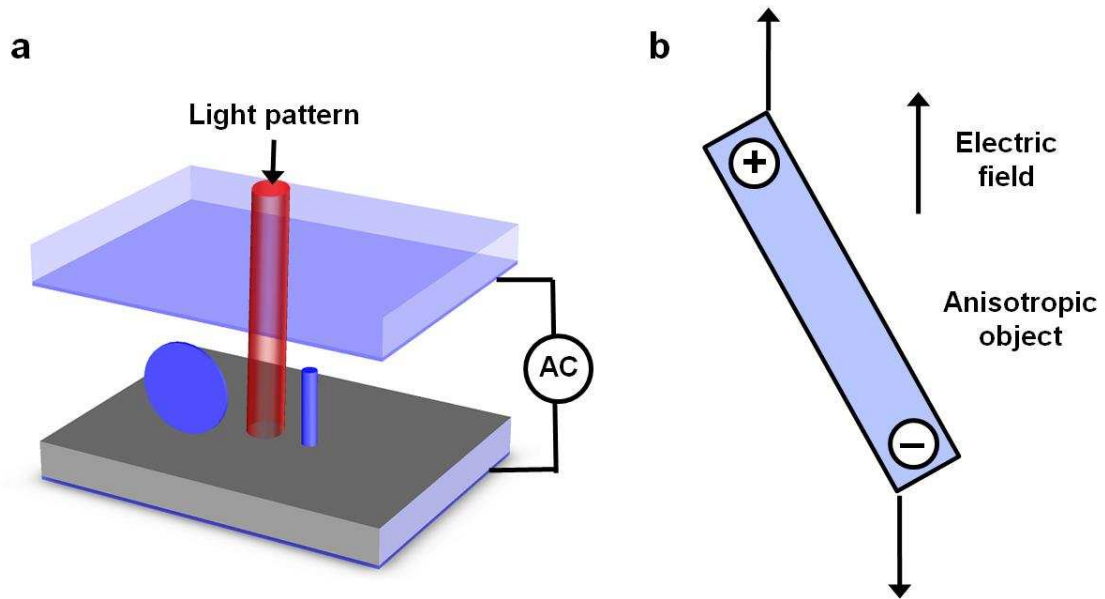


Figure 5.2 (a) Microdisks, nanowires, and other anisotropic objects align normal to the plane of the electrodes of the OET device. (b) Torque exerted on a dipole in an electric field.

To remedy this, we have developed another version of the OET device that retains the same functionality as the original OET device, namely optically-controlled dielectrophoresis. However, this new version of OET combines the ITO-coated glass

electrode and the photosensitive electrode of the standard OET device onto a single substrate (Figure 5.3). This new single-sided OET device can be used with a variety of opposing surfaces, facilitating integration with other microdevices, such as microfluidic channels. Unlike standard OET, the single-sided OET device produces an electric field that is parallel to the plane of the device; thus, we call this device lateral-field optoelectronic tweezers, or LOET. This lateral electric field allows anisotropic objects to be manipulated with the major axis parallel to the substrate of the LOET device.

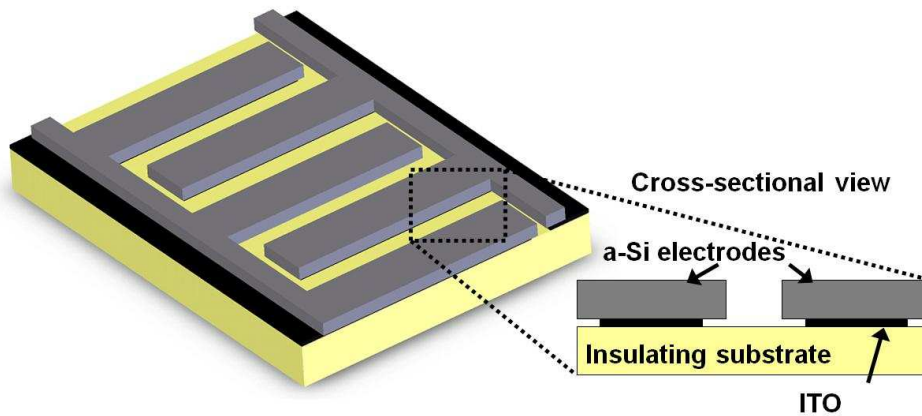


Figure 5.3 Lateral-field optoelectronic tweezers device. The LOET device consists of an interdigitated array of photosensitive a-Si electrodes.

Like the OET device, the lateral-field optoelectronic tweezers device is a two-electrode device. However, unlike the standard OET device, the electrodes of the LOET device are co-located on the same substrate. In LOET, the electrodes are laid out in an interdigitated pattern. As with OET, the electrodes are photosensitive, and consist of the same layers of ITO and intrinsic a-Si. In contrast to standard OET, the electric field is created by applying an ac bias across the interdigitated electrode arrays. As a result, an upper electrode is unnecessary in the LOET device. However, in most of the experiments

presented in this dissertation, a glass cover is used with the LOET device, in order to reduce the evaporation of the liquid / particle solution.

5.2 Operating Principle of LOET

The LOET device operates on the same principal of optically-induced dielectrophoresis as the standard OET device. The LOET device can be modeled with simplified equivalent circuit model that is similar to the OET model (Figure 5.4). In this simplified model, only one electrode pair, defined as one electrode at one potential, and an adjacent electrode at a potential 180° out-of-phase, is represented. The actual LOET device consists of an array of these electrode pair elements.

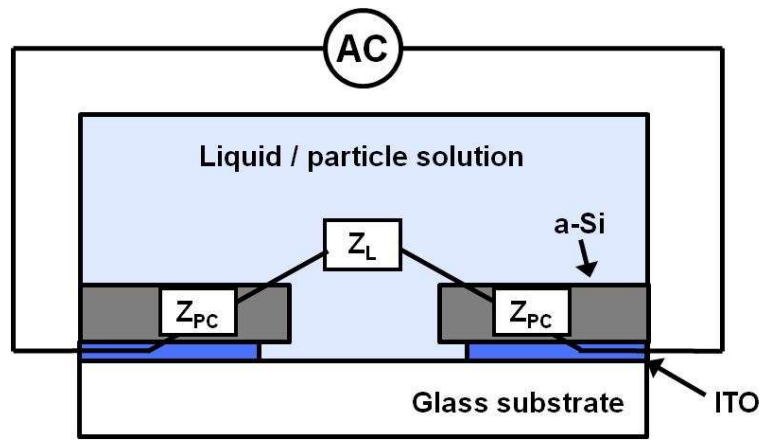


Figure 5.4 Simplified equivalent circuit model of the LOET device.

As with standard OET, in the dark state the impedance of the a-Si, Z_{PC} , is larger than the impedance of the liquid layer, Z_L . However, for LOET, both electrodes are coated with a-Si, so there are two elements represented by Z_{PC} . In areas with no illumination, most of the applied ac voltage drops across the a-Si layers, represented by the two Z_{PC} elements. In order to actuate the LOET device, both electrodes of the pair must be

illuminated, to reduce the impedance of both of the Z_{PC} elements. If this condition is met, a significant voltage drop will occur in the liquid layer, Z_L . Thus, the electric field gradient in the LOET device, like the OET device, is controlled by the position of the optical pattern. However, the direction of the electric field is different in the LOET device as compared to the OET device. In the OET device, the potential difference that creates the electric field is across the top and bottom electrodes, resulting in a field that is primarily perpendicular to the surface of the OET device (Figure 5.1). However, in the LOET device, the potential difference is across the interdigitated electrode fingers. When adjacent electrodes are illuminated, an electric field is formed parallel to the surface of the OET device (Figure 5.5). Full two-dimensional control is retained in the LOET device, as the electrodes are only activated when illuminated with an optical pattern.

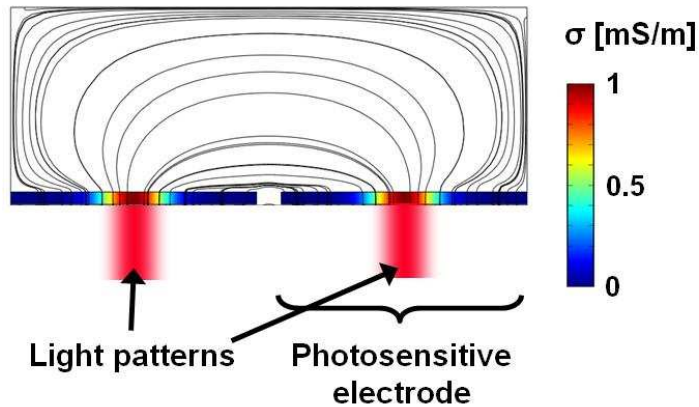


Figure 5.5 Electric field in the LOET device. The direction of the electric field is primarily parallel to the surface of the device.

5.3 Design of LOET

As the LOET device is essentially single-sided, the force in the LOET device is insensitive to a gap between the electrode array surface and an opposing surface. Instead,

the force induced in the LOET device is dependent on the dimensions of the electrodes, including the electrode width and the spacing between the electrode fingers.

When designing the LOET device, the particle size under manipulation must also be considered. The LOET device is more sensitive to variations in particle size than the standard OET device. In the case of particles that experience negative OET, this sensitivity is more relaxed. The electrode width, w , and the spacing between electrode fingers, g , should be equal to or smaller than the major axis of the particle, d (Figure 5.6a). If these conditions are not met, then 2-D particle manipulation will be sacrificed. As w and g become larger than d , the particles will only be actuated along the length of the electrode fingers. Movement across the electrode fingers will be limited, as the optically-patterned electric fields will no longer have enough resolution.

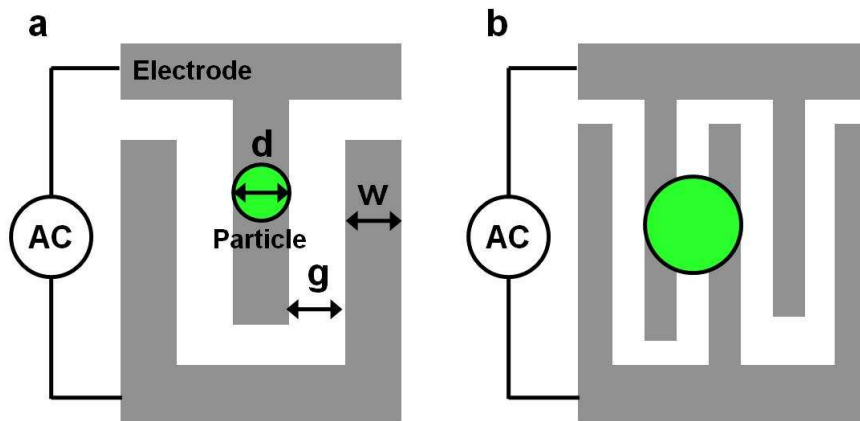


Figure 5.6 Optimizing LOET dimension for particle dimensions. (a) Particles experiencing negative OET should be equal to or larger than the electrode dimensions w and g to ensure 2-D manipulation. (b) Particles experiencing positive OET should be equal to or larger than $2w + g$ to ensure 2-D manipulation.

In the case of particles that experience positive OET, similar requirements exist. However, in this case, $2w + g$ should be equal to or less than d . Particles experiencing

negative OET will rest above the a-Si electrodes, even if no manipulation pattern is present. However, positive-OET-responsive particles will rest in the gaps between the electrodes when no manipulation pattern is present. Thus, if w and g are too large, the particles will remain in the electrode gaps, and only movement along the length of the electrodes will be achieved. However, this can also be used to help align particles to the electrode edges, as will be discussed in Chapter 6.

The reason why particles in the LOET device self-organize even in the absence of optical manipulation patterns is due to undesirable leakage fields across the portions of ITO that are exposed to the liquid layer (Figure 5.3). When voltage is applied across the LOET electrodes, some electric field exists in the liquid layer even in the absence of an optical pattern (Figure 5.7a). Thus, the gaps between the electrodes are regions of higher electric field, causing negative-OET-responsive particles to be repelled, and rest above the a-Si electrodes when no optical pattern is presented. The same high-field regions cause positive-OET-responsive particles to be attracted, and situate in the gaps between the electrodes.

The undesirable leakage fields can be reduced by undercutting the ITO layer beneath the a-Si. A 2- μm undercut of a 10- μm -wide electrode can significantly reduce the leakage fields, and is the technique employed in the devices described in this chapter (Figure 5.7b). Alternatively, an electrically insulating layer that blocks direct exposure of the ITO electrodes to the liquid can be used, such as encapsulating the ITO electrodes using a-Si (Figure 5.7c). Other LOET geometries that reduce the leakage fields will be described in Chapters 7 and 8.

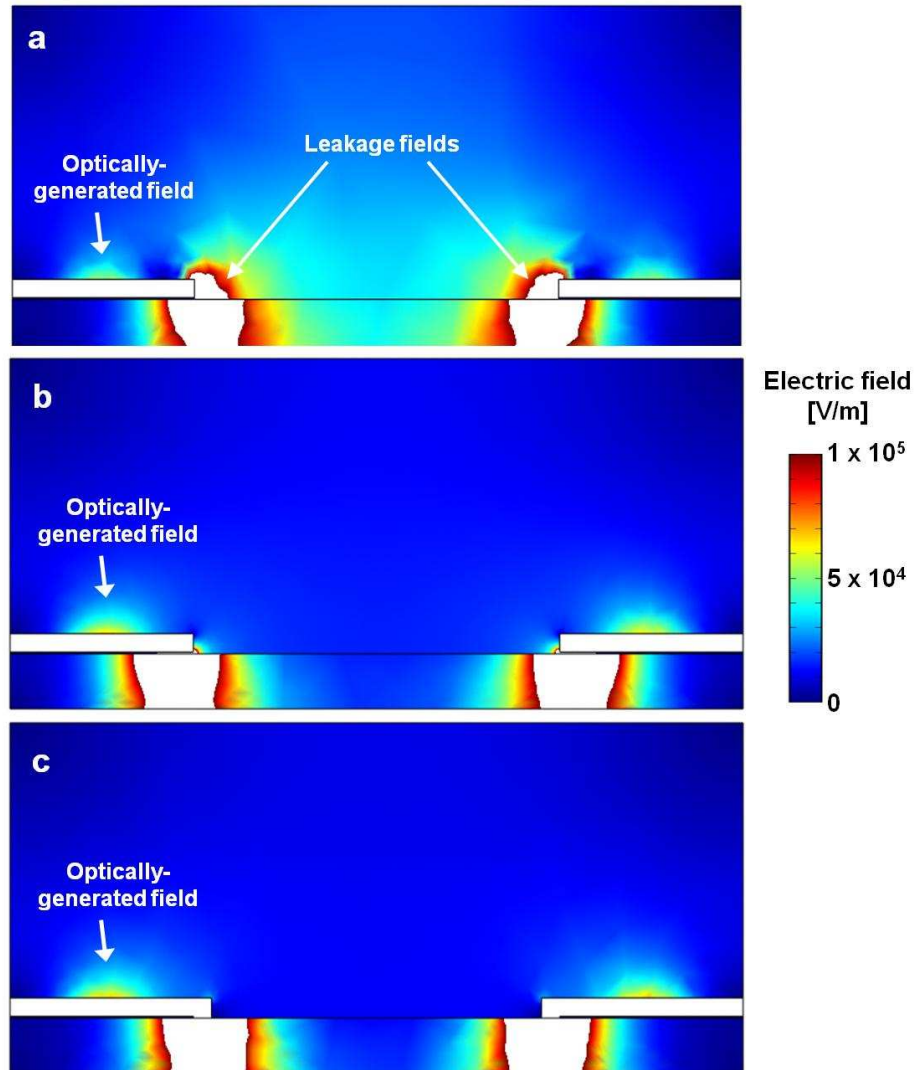


Figure 5.7 Leakage fields in the LOET device. (a) An LOET device with ITO directly exposed to the liquid, with no undercut, shows significant leakage fields. White areas represent electric field strengths that are higher than the range of the scale bar. (b) An LOET device with a 2- μm undercut of the ITO beneath a 10- μm -wide a-Si electrode. The leakage fields are significantly reduced. (c) A further reduction of the leakage fields can be obtained by encapsulated the ITO electrodes with the a-Si layer.

5.4 Fabrication of LOET

The fabrication of the LOET device is slightly more involved than the standard OET device, but is also suitable for the manufacturing of low-cost devices (Table 5.1 and

Figure 5.8). The devices are fabricated from wafers with existing ITO and hydrogenated amorphous silicon (a-Si:H) layers (Silicon Display Technology). The first two fabrications steps are the same as the standard OET device. After the a-Si:H layers are deposited, the electrode arrays are photolithographically defined and etched using reactive-ion etching (RIE), stopping on the ITO layer. The ITO is then chemically etched in 38% HCl to complete the formation of the interdigitated electrode arrays. Finally, a second RIE is performed to create bias pads to the ITO layer. Only two bias pads are required to address the entire LOET array, which consists of more than 450 electrode fingers.

Table 5.1 LOET fabrication process overview

Step	Process	Parameters
1	Clean substrate; N ₂ dry	Start with 0.85-mm-thick ITO-coated glass substrate, with 50 nm n+ a-Si:H / 1 μm a-Si:H
2	Dehydration bake	150°C for 15 min
3	Spin on photoresist (AZ 5214E), define interdigitated electrode pattern (Mask #1)	500 rpm spread for 5 s, 2000 rpm for 30 s Equipment: Headway spin coater Karl Suss MA6 contact mask aligner
4	RIE a-Si electrodes	9:1 SF ₆ :O ₂ , 100 mtorr, 100 W for 1 min. Equipment: Plasmatherm PK-12 RIE
5	Wet etch ITO between electrodes	38% HCl for 3 min.
6	Define electrical contact areas with photoresist	500 rpm spread for 5 s, 2000 rpm for 30 s Equipment: Headway spin coater
7	RIE electrical contact pads	9:1 SF ₆ :O ₂ , 100 mtorr, 100 W for ~2 min. Equipment: Plasmatherm PK-12 RIE
8	Remove photoresist	Acetone
9	Electrical contact pads	Silver conductive epoxy (Epotek E2101) Recipe: 3:1 part A to part B, cure @ 150°C for 1 hr.

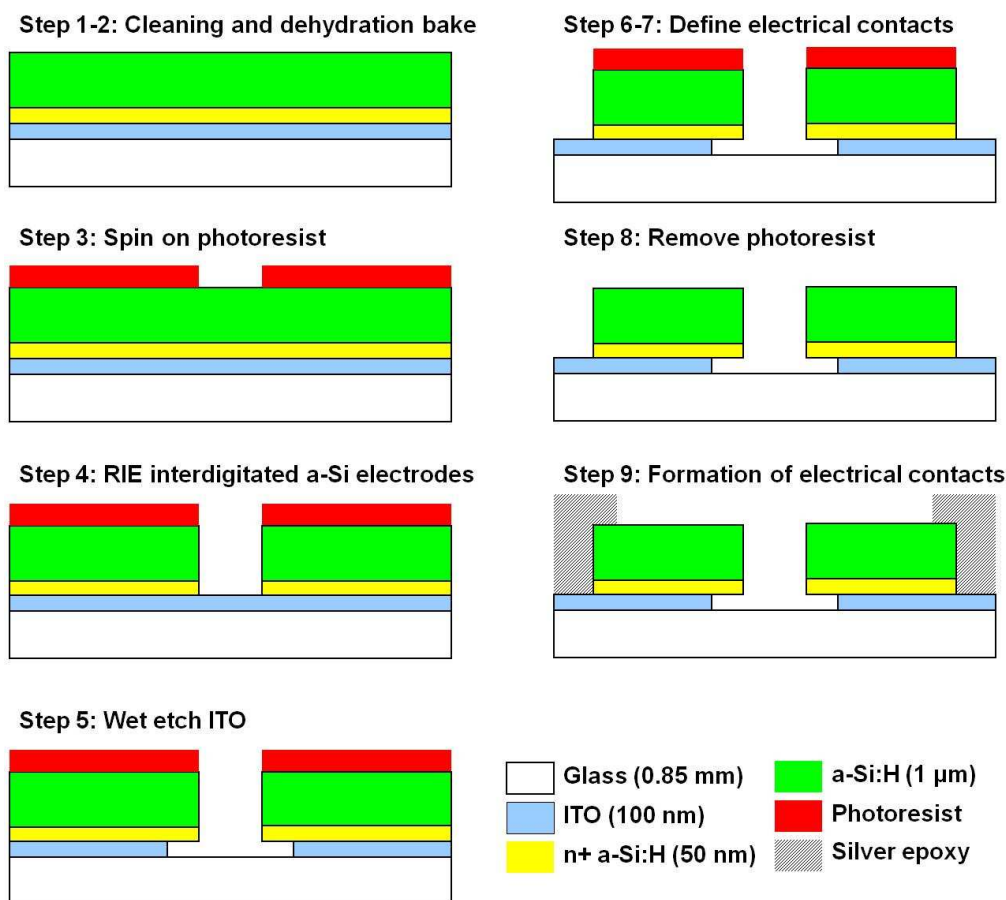


Figure 5.8 Fabrication process of LOET devices.

5.5 Experimental Results

In order to demonstrate that the lateral-field OET device retains the 2-D manipulation pattern capabilities of the standard OET device, initial tests were performed using polymer microparticles. Polystyrene beads with diameters of 25 and 45 μm were suspended in a solution of KCl and deionized water, which is adjusted to attain a conductivity of 10 mS/m. Approximately 20 μL of the bead solution is dispensed into the LOET device.

Polystyrene bead manipulation in the LOET device was tested using a laser source. The LOET devices had electrodes that were 10 μm in width, with a gap of 20 μm between electrode fingers. The electrode arrays were biased with an ac voltage of 4 Vpp at 100 kHz. Both longitudinal and transverse motion of 25- μm -diameter polystyrene beads was observed (Figure 5.9). Longitudinal motion refers to particle movement along the length of the electrodes, and transverse motion refers to particle movement across electrode fingers.

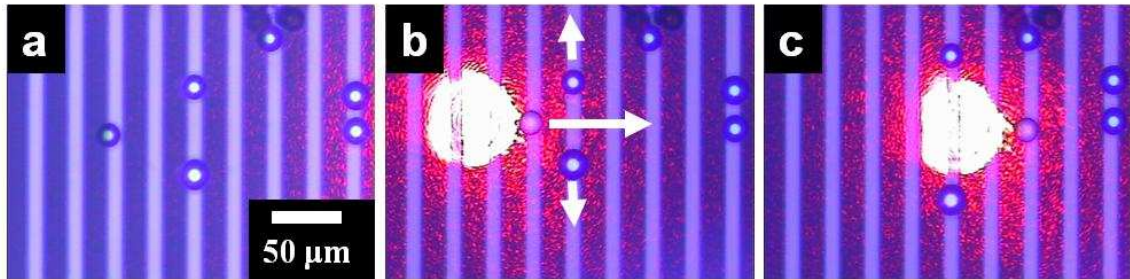


Figure 5.9 Movement of 25- μm -diameter polystyrene beads in the LOET device. (a) The initial positions of the beads. (b) A laser is used to transport a single bead in the transverse direction, while simultaneously moving other beads in the longitudinal directions. Arrows indicate the direction of motion. (c) The final position of the polystyrene beads.

The velocity induced in the LOET device on 25- and 45- μm -diameter polystyrene beads is shown as a function of the illumination light intensity and applied ac voltage (Figure 5.10). Both the longitudinal and the transverse directions of movement have approximately the same manipulation velocities, further confirming that full 2-D motion is preserved on the LOET device.

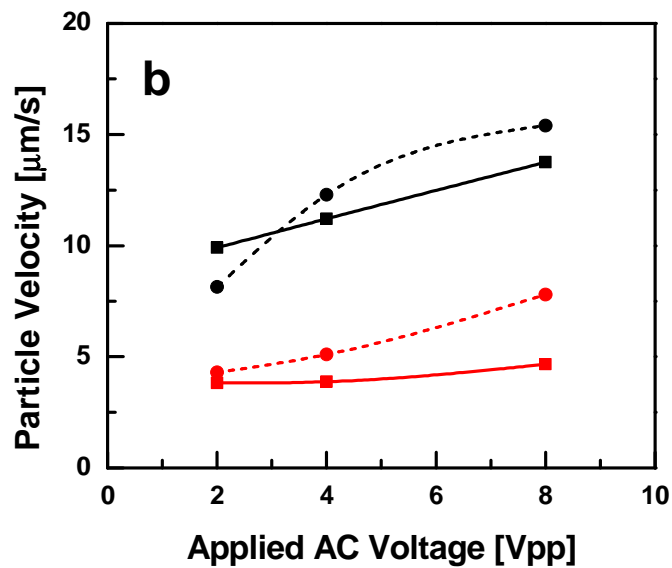
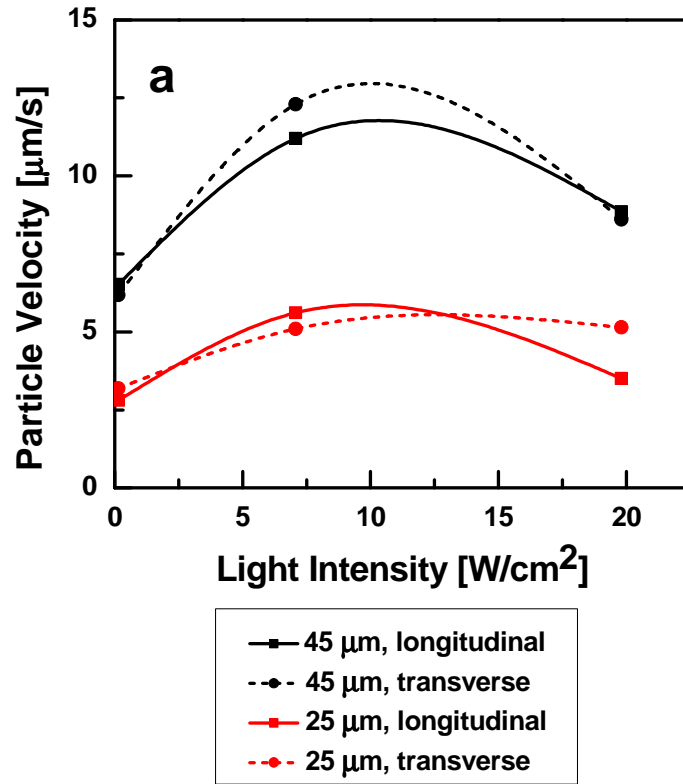


Figure 5.10 Experimental induced velocities of polystyrene beads in the LOET device [52]. Longitudinal velocity refers to movement along an electrode, while transverse velocity refers to movement across electrode fingers. (a) Particle velocity as a function of illumination pattern intensity. (b) Particle velocity as a function of applied ac voltage at a frequency of 100 kHz.

Chapter 6

III-V Microdisk Laser Assembly on Silicon Using Lateral-Field Optoelectronic Tweezers

6.1 Motivation

Copper interconnects are inherently low-bandwidth, and are limited to throughputs of 10 Gb/s or less. Copper presents a bottleneck in data throughput as data transfer rates in computers increase. Optical interconnects are an attractive alternative to copper, and have already supplanted copper wires in long-haul data networks as well as server-to-server interconnects. However, optical interconnects have not yet been employed for short-range data networks, such as from board-to-board, chip-to-chip, or intrachip, as optical integration is difficult and expensive.

One way to lower the manufacturing costs and increase integration of optical components is by fabricating optical elements directly on silicon. Silicon photonic devices are designed to be compatible with CMOS processes, leveraging the existing manufacturing infrastructure and processes. In addition, optical elements can be directly

integrated with CMOS circuitry, such as nanoscopic photonic waveguides and optical modulators [100, 101].

One challenge that remains for silicon photonics is the integration of optical sources. Silicon is an indirect bandgap semiconductor, making it a poor light emitter. Silicon Raman lasers have been demonstrated, but external optical light sources are still required, and their footprint is large [102, 103]. Electrically-pumped lasers are much more desirable for silicon photonics, requiring the use of compound semiconductor materials. However, the integration of these materials with silicon presents another set of challenges.

Heteroepitaxial growth can create compound semiconductor materials directly on a silicon substrate [104], but the growth temperature (greater than 400°C) is usually too high for post-CMOS processing. Alternatively, there are low temperature (less than 300°C) compound semiconductor-to-silicon bonding techniques, either assisted by oxygen plasma [105] or a thermosetting polymer [106]. Using these techniques, AlGaInAs-Si hybrid evanescent lasers [107] and InP-based microdisk lasers have been demonstrated [108]. However, integrating lasers on fully-processed CMOS wafers presents additional challenges, as the silicon bonding surfaces are buried underneath many (up to ten) layers of electrical interconnects, and therefore the bonding surface exhibits significant topographical variation. To avoid such issues, one approach is to build electrical interconnects and photonic circuits on separate Si wafers, bond the Si wafers, and then use flip-chip bonding to secure the III-V semiconductor materials on the Si wafers [109]. However, this is a complicated bonding process, requiring multiple bonding steps, making it difficult to integrate sources with a variety of wavelengths.

Optoelectronic tweezers provides a room-temperature microparticle manipulation process that is a good candidate for post-CMOS assembly of hybrid semiconductor lasers. The room-temperature optofluidic assembly process can overcome the topography issue and more efficiently utilize expensive epitaxial III-V wafers. Furthermore, heterogeneous integration of multiple materials can be performed in parallel, unlike wafer bonding techniques.

Microdisk lasers are an attractive candidate for CMOS integration, as they have a small footprint and do not require mirrors [110]. However, in the standard OET device, anisotropic objects such as microdisks align with the electric field lines, and are manipulated with the major axis normal to the photosensitive electrode. Instead, the microdisks should be assembled with their major axis parallel to the substrate. Thus, instead of the standard OET device, lateral-field optoelectronic tweezers (LOET) are used for the post-CMOS optofluidic assembly of microdisk lasers. This assembly process allows LOET to integrate pre-fabricated high-performance III-V semiconductor lasers on fully-processed CMOS wafers. Here, InP-based microdisk lasers are fabricated to demonstrate room-temperature heterogeneous integration onto a silicon platform.

6.2 InP-based Microdisk Lasers

An InGaAs/InGaAsP multiple-quantum-well (MQW) epitaxial wafer with a photoluminescence peak at 1550 nm is used to fabricate microdisk lasers [57]. Optical gain is provided by three 7-nm-thick InGaAs quantum wells that are separated by 10-nm-thick InGaAsP layers. The MQW layers are sandwiched by two symmetrical larger-bandgap optical confinement layers, while InP is used as a sacrificial layer for releasing

the microdisks into solution. The total thickness of the active layers is approximately 200 nm. The detailed epitaxial structure of the active layers is shown in Table 6.1.

Table 6.1 Epitaxial layer structure of the microdisk lasers

Layer (Bandgap)	Thickness	Description
InGaAsP (1.1 μm)	20 nm	Optical confinement layer
InGaAsP (1.2 μm)	50 nm	Optical confinement layer
InGaAsP (1.2 μm)	10 nm x 4	Quantum well barriers (4 layers)
$\text{In}_{0.53}\text{Ga}_{0.47}\text{As}$	7 nm x 3	Quantum wells (3 layers)
InGaAsP (1.2 μm)	50 nm	Optical confinement layer
InGaAsP (1.1 μm)	20 nm	Optical confinement layer
InP (919 nm)	350 μm	Sacrificial layer (substrate)

Microdisk fabrication is achieved by standard optical lithography and etching processes (Figure 6.1). Silicon nitride is deposited on the epitaxial wafer using low-pressure chemical vapor deposition (LPCVD) (Step 1). The circular microdisk pattern is transferred from photoresist to the silicon nitride hardmask by plasma etching (Step 2). After removing the photoresist, the hardmask pattern is then transferred through the active layers to the InP sacrificial layer by a nonselective etchant of 0.5% Br_2 in methanol (Step 3). The hardmask is removed, and the MQW microdisks are released by etching the InP sacrificial layer using a diluted hydrochloric acid (HCl) solution (Step 4). The microdisks are then re-suspended in ethanol for LOET assembly. Figure 6.2a shows fabricated 5- μm -diameter microdisks on a partially-etched InP sacrificial layer. A close-up of the microdisk is shown in Figure 6.2b, showing a smooth sidewall that is essential for laser cavities with a low scattering loss.

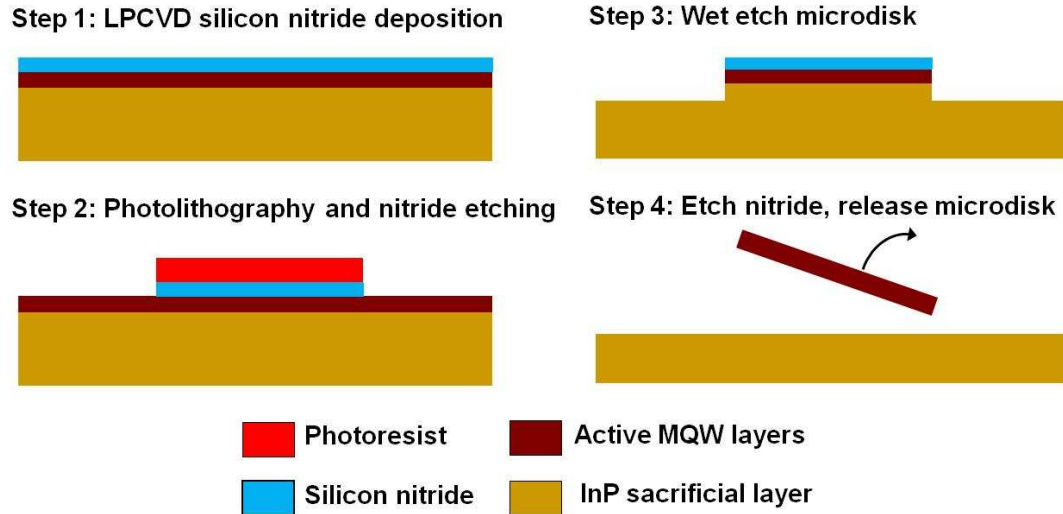


Figure 6.1 Fabrication process for InGaAs/InGaAsP multiple-quantum-well (MQW) microdisk lasers.

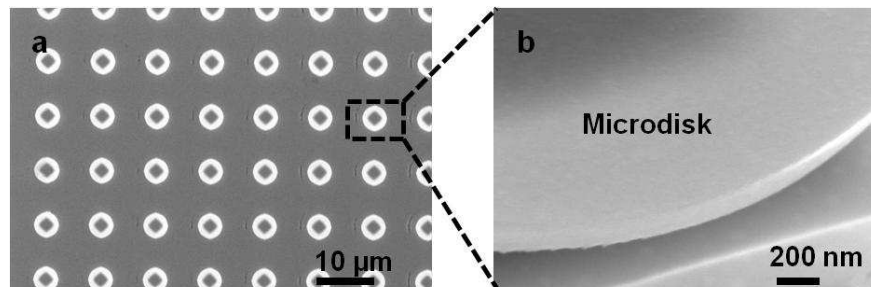


Figure 6.2 5- μm -diameter microdisks on an InP substrate. (a) The disks are wet etched by 0.5% Br_2 in methanol, followed by partial etch of the InP sacrificial layer using diluted HCl. The rhombic grey region is an InP pedestal under the active layers of the microdisk. (b) Microdisk sidewall after etching. The smooth sidewall creates a high quality factor laser cavity.

Simulations of the whispering gallery mode (WGM) of the microdisk lasers indicate that the optical mode profile is confined near the edge of disks (Figure 6.3). The fundamental transverse electric (TE) WGM mode is concentrated near the edge of the microdisk. Thus, to avoid scattering loss, the microdisks are assembled on pedestals such

that the boundary of pedestals is at least 1 μm and 1.5 μm away from the microdisk edge for 5- μm -diameter and 10- μm -diameter microdisk lasers, respectively [110].

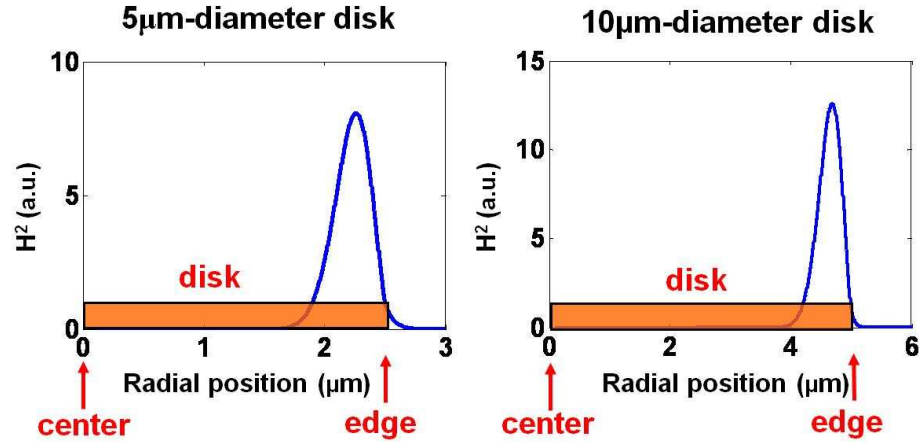


Figure 6.3 The calculated magnetic field intensity profiles of the fundamental TE whispering gallery radial mode for 5- μm -diameter and 10- μm -diameter microdisks. The origins of the figures represent the center of the disks while the orange area represents the cross-section of the microdisks.

6.3 LOET Device for Microdisk Assembly

Silicon pedestals have been integrated with the LOET device for microdisk assembly. This integrated LOET device is shown schematically in Figure 6.4. Interdigitated electrodes consisting of a 100-nm-thick aluminum layer, topped by 0.8 μm of amorphous silicon (a-Si) are deposited on a patterned Si substrate. The a-Si electrodes are 10 μm in width, and with gaps of 5 μm between adjacent electrodes. The 3- μm -diameter silicon pedestals are centered in the 5- μm gaps.

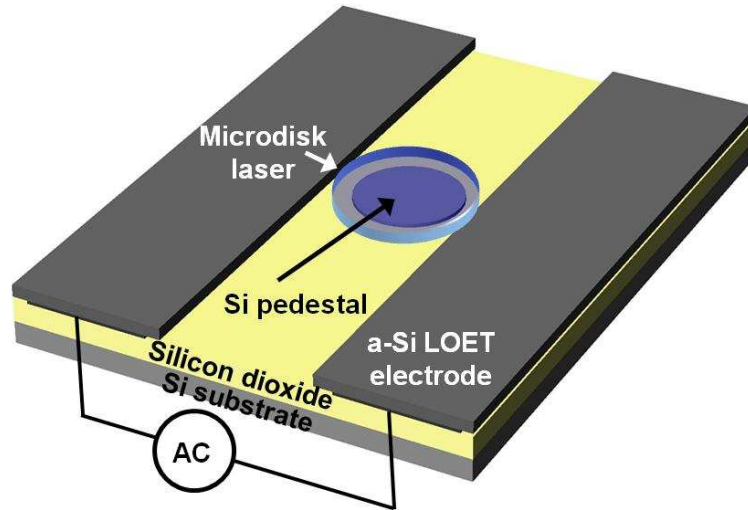


Figure 6.4 Schematic diagram of the integrated LOET device for microdisk laser assembly.

The LOET device is fabricated on a silicon-on-insulator (SOI) wafer using a two-mask process (Figure 6.5). Silicon pedestals are patterned by dry etching the top silicon layer (Step 1), followed by a 50-nm thermal oxidation to passivate the pedestals (Step 2). The 100-nm-thick aluminum and 0.8- μm -thick a-Si layers are then deposited using electron-beam evaporation and PECVD, respectively (Step 3). The a-Si is reactive-ion etched to create interdigitated electrodes, and then used as a hard mask to wet etch the aluminum layer (Step 4). At this point, the device is ready for the microdisk assembly process (Steps 5 and 6), which is further described in Chapter 6.4. After assembly, the a-Si layer is removed by XeF_2 etching at 40°C so that the a-Si does not interfere with the optical mode of the microdisk (Step 7).

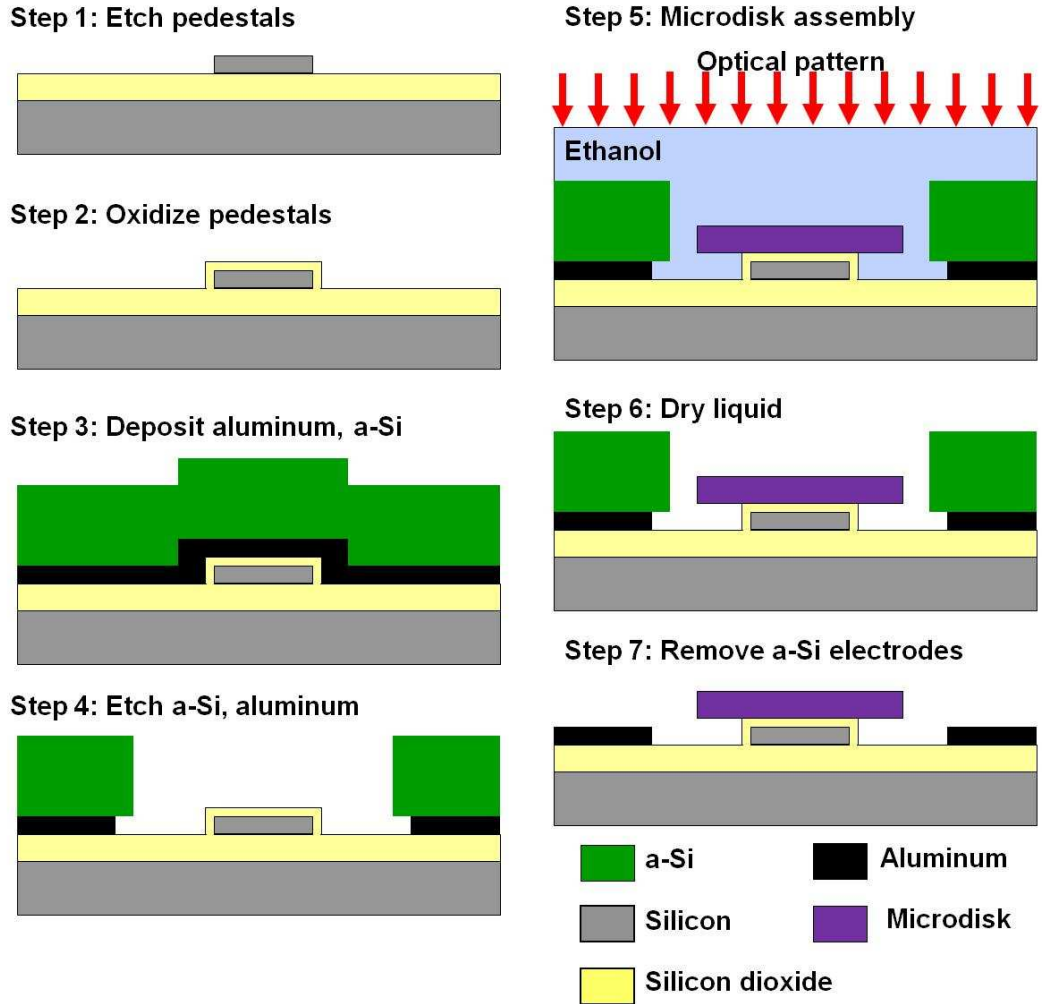


Figure 6.5 Fabrication process of integrated LOET devices.

As described in Chapter 5, the a-Si layer functions as a light-controlled virtual electrode; the illuminated area switches from a low-conductivity state to a high-conductivity state. An ac voltage is applied across the electrodes, creating an electric field. When optical patterns are projected onto the electrodes, the electrodes are switched to a high-conductivity state, switching the electric field to the liquid solution. The position of the electric field across the electrodes is controlled via the optical patterns. The electric field is non-uniform, as it is strongest only in the illuminated areas of the

electrodes. This field gradient generates an optically-induced dielectrophoretic force, which is used to attract microdisks. The highest forces are in the illuminated areas near the electrode edges (Figure 6.6), which attract and align disks in the middle of the gap between electrodes when the size of the disk is equal to or larger than the gap.

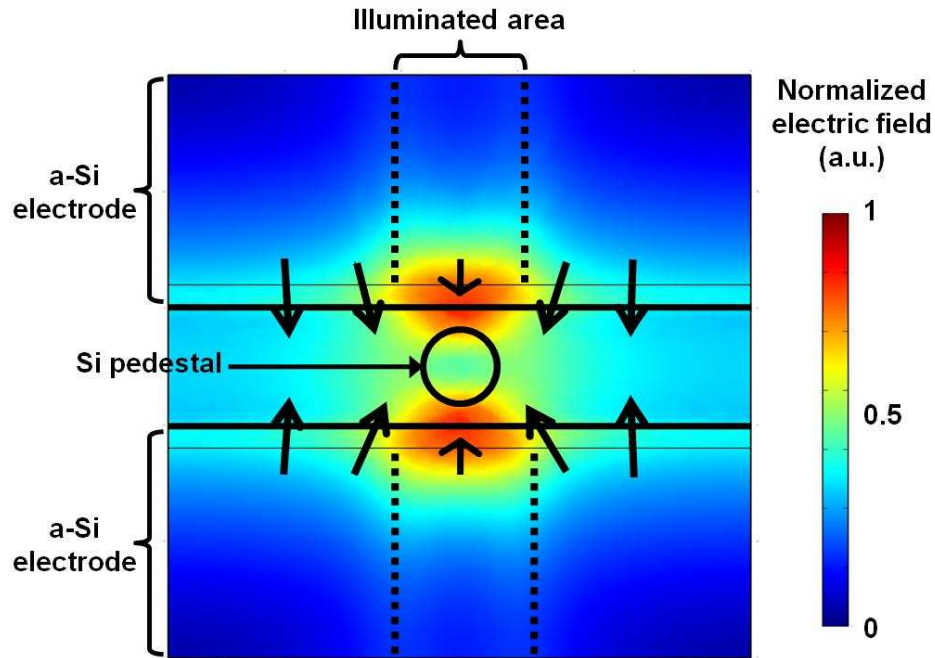


Figure 6.6 Finite-element simulation of the electric field profile across the LOET electrodes. The arrows show the direction of the optically-induced force. The strongest forces occur near the edges of electrodes with illumination.

6.4 III-V Microdisk Laser Assembly on a Silicon Platform

The fabricated InP-based microdisks, suspended in ~90% ethanol, are pipetted onto the LOET substrate. The LOET electrodes create an optically-induced DEP force which attracts the microdisks to the illuminated areas, and the microdisks self-align in the gap between the electrodes. An optical pattern is projected onto the LOET device through a 20× objective lens (Figure 6.7). A CCD camera is used to monitor the relative locations of the projected pattern, the microdisks, and the pedestals. The use of a computer

projector (Dell 2400MP) provides real-time control over the optical patterns, which allow transportation of the microdisks along the length of the electrodes using an applied AC voltage of 1 to 10 V_{pp} at 200 kHz. Once the disks are aligned over a pedestal, the applied voltage is increased to 20 V_{pp} to hold the disks in place as the solution dries. Ethanol is used to minimize surface tension forces during drying, ensuring that the disks remain in place. After drying, the a-Si layer is removed to avoid interference with the optical modes of the microdisks, as mentioned in Chapter 6.3. Figure 6.8 displays a series of microscope images showing the assembly process, as well as SEM images of assembled 5- μm -diameter (Figure 6.8c) and 10- μm -diameter microdisks (Figure 6.8f). As the gap between electrodes is 5 μm , 5- μm -diameter microdisks fit between the electrodes (Figure 6.8a, b), while 10- μm -diameter microdisks self-align in the middle of the gap (Figure 6.8d, e). Both sizes of microdisks can be moved along the length of the electrodes by controlling the optical patterns.

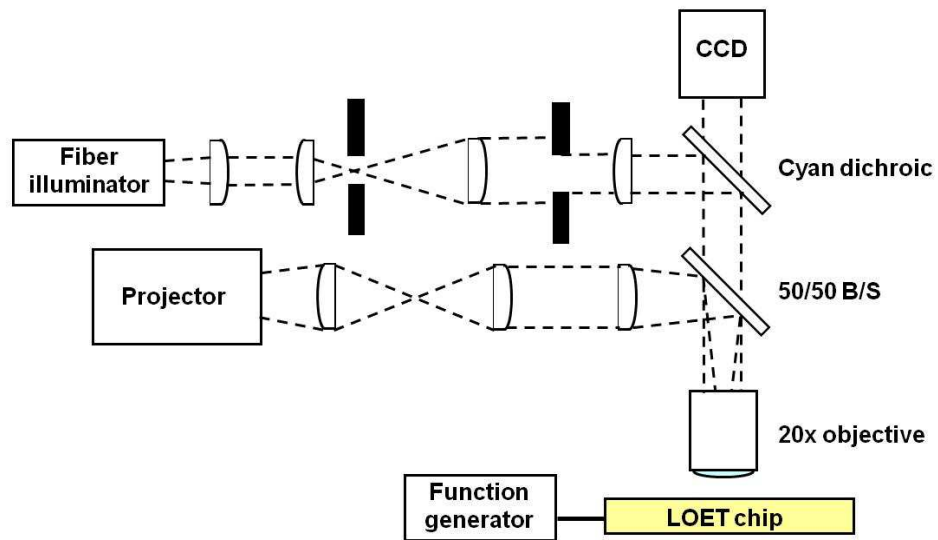


Figure 6.7 Optical setup for microdisk assembly using LOET. A computer-controlled projector is used to generate optical patterns to attract and transport microdisks to a designated position.

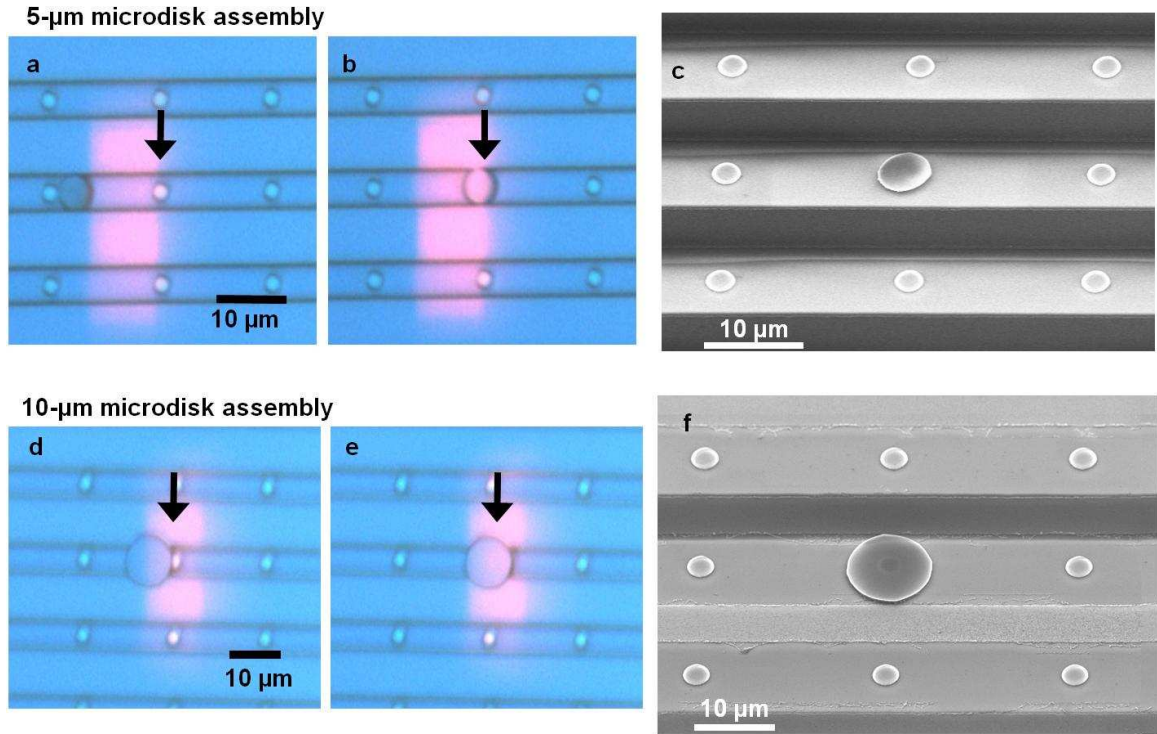


Figure 6.8 Assembly of 5- μm -diameter (a-c) and 10- μm -diameter (d-f) microdisks onto 3- μm -diameter silicon pedestals using LOET. (a, d) The initial positions of the microdisks. The optical trapping pattern, generated by a computer projector, is visible as a red rectangle. The target Si pedestal for assembly is indicated by an arrow. (b, e) The microdisks are positioned over the target Si pedestal. The trapping force is then increased to immobilize the disks on the substrates. (c, f) SEM pictures of assembled 5- and 10- μm -diameter microdisks.

The alignment accuracy of the assembled microdisks on the pedestals is critical, since the pedestals have to be far enough from the edge of microdisks to avoid the pedestal-induced scattering loss (Figure 6.9). The horizontal alignment (alignment of the microdisks between the electrodes) is a self-aligning process, as both edges of the microdisks experience identical trapping forces due to symmetry. The vertical alignment (alignment of the microdisks along the length of the electrodes) is controlled by the projected light. The resulting misalignment is $0.13 \pm 0.05 \mu\text{m}$ in the horizontal direction,

and $0.25 \pm 0.18 \mu\text{m}$ in the vertical direction. The self-aligned horizontal alignment is usually more accurate than user-controlled vertical alignment, although an image-feedback control system similar to the one described in Chapter 1.3.3 can be implemented to further improve the vertical alignment. However, the current misalignment is less than $0.25 \mu\text{m}$, which is sufficient to avoid the scattering loss due to the pedestals.

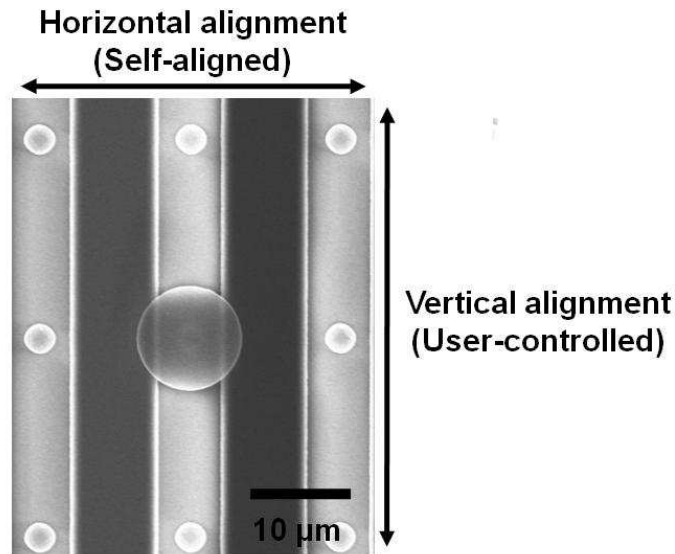


Figure 6.9 Alignment accuracy measurement of assembled microdisks. The horizontal alignment is achieved by a self-alignment of the disks across the electrode gap. Vertical alignment is achieved by user control of the optical pattern.

6.5 Optical Measurements of Assembled Microdisks

The assembled microdisk lasers are optically pumped at room temperature (18°C) by $0.5\text{-}\mu\text{s}$ pulses with a 20 kHz repetition rate (1% duty cycle) using a 780-nm diode laser. The pump beam is focused onto the disk through a $40\times$ objective, resulting in a beam size of $3 \mu\text{m}$. The emitted light is collected through the same objective and then filtered by an

optical filter to block the light from the pump laser. The filtered optical signal is coupled to a multimode fiber, and the output spectrum is measured by an optical spectrum analyzer (OSA).

Both 5- and 10- μm -diameter microdisk lasers on silicon pedestals exhibit single-mode operation under pulsed excitation, with lasing wavelengths of 1558.7 nm and 1586 nm, respectively (Figure 6.10a). The collected laser power at the lasing wavelength versus peak pump power and effective absorbed power (L-L curve) are shown in Figure 6.10b, where approximately 40% of the pump power is absorbed by the active layers of the microdisk lasers. The threshold pump powers for 5- and 10- μm microdisk lasers on silicon pedestals are 0.85 mW and 2.5 mW, which correspond to 0.34 mW and 1 mW of effective absorbed powers, respectively. The 5- μm -diameter microdisk laser has a lower threshold pump power due to a smaller optical mode volume. The threshold pump powers of the microdisk lasers before and after LOET assembly are comparable, indicating that the microdisks are not damaged during the assembly procedure (Figure 6.10b).

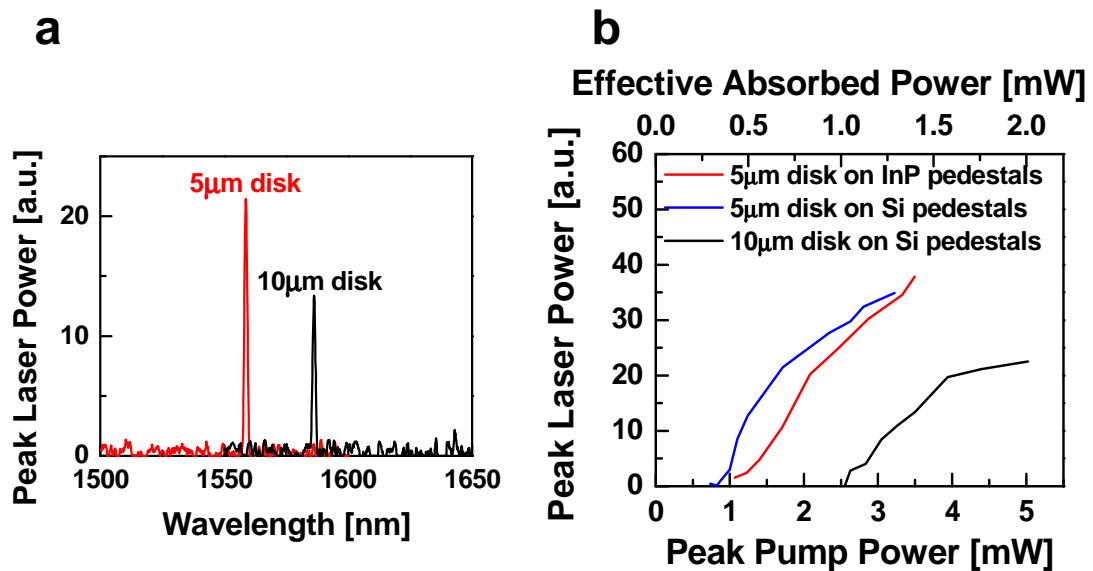


Figure 6.10 Optical measurements of assembled microdisk lasers. (a) Lasing spectra from assembled 5- and 10- μm -diameter microdisks on silicon pedestals under pulsed excitation. The pump power for these two spectra is 1.7 mW for the 5- μm disks and 3.5 mW for the 10- μm disks. (b) Collected laser power versus peak pump power (L-L curves). The threshold pump powers for 5- and 10- μm disks are 0.85 mW and 2.5 mW, corresponding to 0.34 mW and 1 mW of effective absorbed power in the active layers.

Heating of the microdisk lasers eventually limits the output power when the pump power exceeds 2 mW and 4 mW for 5- and 10- μm microdisks on Si pedestals, respectively (Figure 6.10b). There are two possibilities that could hinder heat dissipation. The first is the 3- μm -thick buried silicon dioxide layer underlying the silicon pedestals, which substantially increases the thermal resistance due to the low thermal conductivity of silicon dioxide. The second is a poor contact between the microdisk lasers and the silicon pedestals. Therefore, for microdisks on InP pedestals, before releasing and assembly, the power saturation is not as severe as those on silicon pedestals. However, thermal annealing can improve the contact between the microdisk lasers and the silicon

pedestals. After annealing, the maximum laser output power increases, indicating improved thermal conduction (Figure 6.11). However, the threshold power also increases, due to non-ideal annealing conditions, which are currently being optimized.

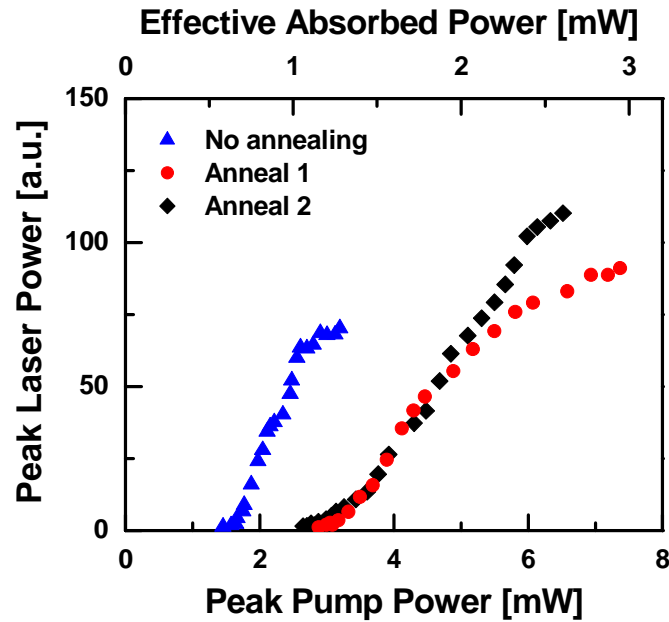


Figure 6.11 L-L curves of assembled 5- μm microdisk lasers before and after thermal annealing. The maximum output power of a 5- μm microdisk laser is improved by annealing at 300°C for 5 hours (Anneal 1), or 300°C for 5 hours, followed by another anneal at 350°C for 5 hours (Anneal 2). After annealing, the maximum output power is increased by 30% and 57% for annealing conditions 1 and 2, respectively.

Chapter 7

Nanowire Assembly Using Lateral-Field Optoelectronic Tweezers

7.1 Motivation

An ongoing challenge for the mass production of nanowire-based electronics is the controlled assembly of single nanowires. Nanowire fabrication using “bottom-up” approaches presents difficulties to integration with heterogeneous material systems. Post-synthesis integration circumvents these issues, but has its own limitations. The post-synthesis assembly of individual nanowires and carbon nanotubes has been demonstrated using mechanical manipulators [4, 5, 111] and optical tweezers [23, 24]; however, the parallel processing capabilities of these tools are limited. Single nanowires have also been assembled using the dielectrophoretic forces produced by microfabricated metal electrodes, but the trap locations and trapping patterns are static [112].

Optoelectronic tweezers has also been used to assemble single nanowires in parallel, but is limited to aligning nanowires in a direction normal to the photoconductive surface of the device [60]. In order to assemble nanowires with their long axis parallel to the

device substrate, lateral-field optoelectronic tweezers (LOET) are required. Here, nanowire trapping and assembly is demonstrated on LOET devices. This work has applications towards creating nanowire electronics and optoelectronics, such as a nanowire-based LED display.

7.2 Nanowire Trapping Using Lateral-Field Optoelectronic Tweezers

Semiconductor nanowire trapping is demonstrated using LOET [61]. As discussed in Chapter 5, although the force produced by LOET is similar to that of standard OET, the directions of the electric field lines in the LOET device are predominantly parallel to the plane of the electrodes. Thus, anisotropic particles such as nanowires that have a major axis significantly longer than the minor axis will line up with the electric field lines as a result of torque on the dipole of the particle.

Silicon nanowires of varying diameters (50 to 200 nm) and lengths (5 to 50 μm) were fabricated by etching a silicon wafer [113]. The nanowires are then suspended in deionized water by sonification of the wafer. Potassium chloride is added to the nanowire suspension to adjust the conductivity to 1.5 mS/m. A 20- μL aliquot of the nanowire solution is introduced into the LOET device. The LOET devices used in these nanowire manipulation experiments had electrodes that were 20 μm in width, separated by 2 μm gaps. The electrodes were biased at 5 V_{pp} at 50 kHz. The optical source was a 650-nm diode laser, at an intensity of 10 W/cm².

Initially, no ac bias was applied to the LOET device. Using dark-field microscopy, randomly oriented nanowires were observed near the surface of the LOET device (Figure 7.1a). Individual nanowires were identified, and the optical pattern was positioned near a

specific nanowire (Figure 7.1b). The ac bias was then applied, activating the LOET device and creating DEP force. The nanowire experiences an attractive force, and becomes trapped in the illuminated area. After the nanowire has been trapped, it can be transported across the LOET surface at a velocity of $20 \mu\text{m/s}$ (Figure 7.1c). The initial position of the nanowire trapping and the final position of the nanowire after transport are shown in Figure 7.1d.

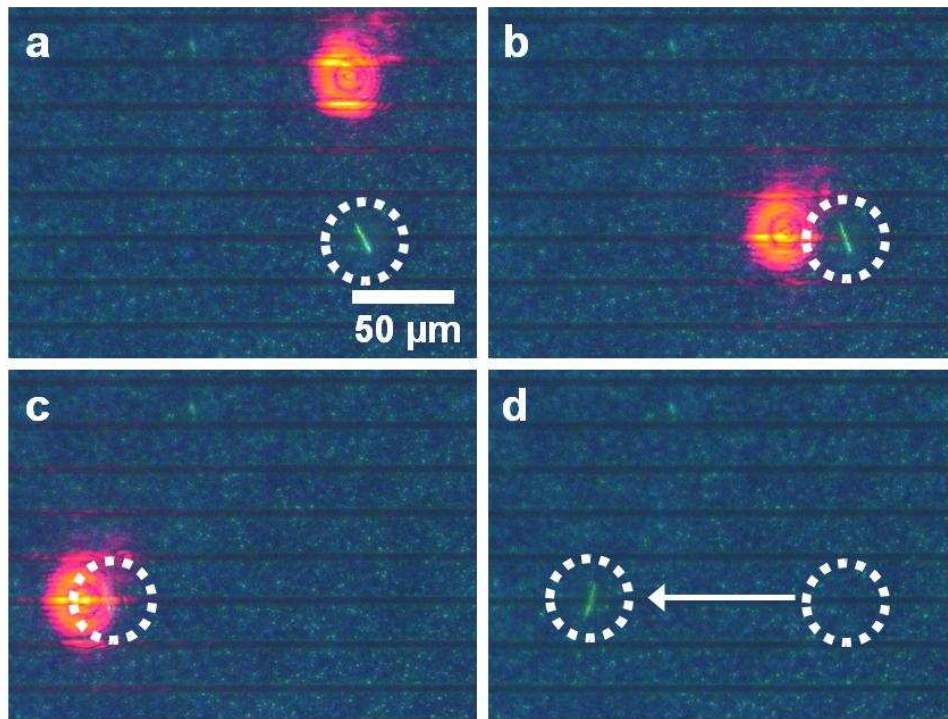


Figure 7.1 Trapping and transport of silicon nanowires using LOET [61]. (a) The initial position of a silicon nanowire, with the electric field turned off. The laser spot is visible in the upper right. (b) The laser is moved closer to the nanowire. This frame is immediately before the electric field is switched on; after the electric field is applied, the nanowire is attracted towards the laser. (c) The trapped nanowire is transported by scanning the laser spot at up to $20 \mu\text{m/s}$. (d) The laser is switched off to show the final position of the nanowire in greater clarity. The initial position is also indicated; the direction of the transport is shown by the arrow.

7.3 Nanowire Rotation and Trapping Using Planar Lateral-Field Optoelectronic Tweezers

As discussed above, LOET enables nanowire trapping and transport. However, the LOET device does not provide control over the rotational orientation of the nanowires. In order to achieve more functionality for nanowire assembly, we have developed a new version of LOET that affords control of the in-plane orientation of nanowires. This device uses a blanket deposition of a-Si, without etching electrodes into the a-Si layer. Thus, we call this device planar lateral-field optoelectronic tweezers (PLOET), referring to the unetched a-Si layer.

7.3.1 Planar Lateral-Field Optoelectronic Tweezers

The PLOET device consists of an interdigitated array of 100-nm-thick aluminum electrodes on an oxidized silicon wafer (Figure 7.2). The electrode fingers are separated by gaps of 10 or 25 μm . A 0.75- μm -thick amorphous silicon (a-Si) layer is deposited over the aluminum electrodes by PECVD. The gap between the electrodes forms the active area for nanowire assembly.

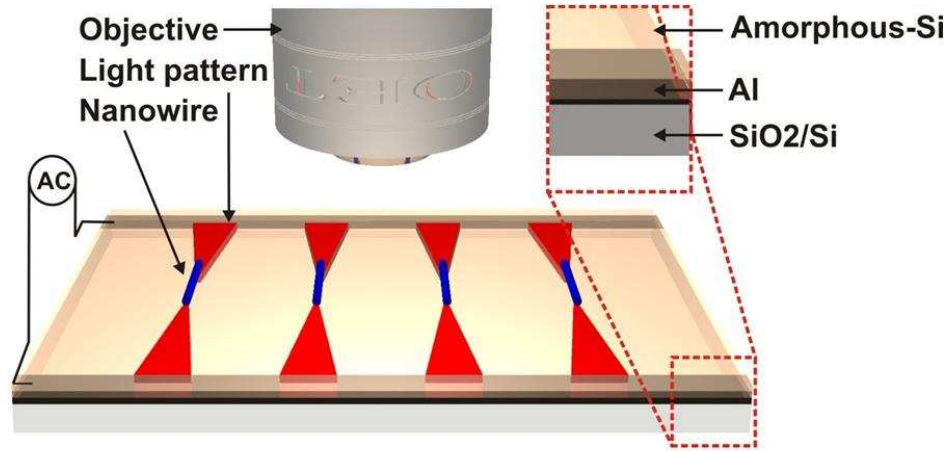


Figure 7.2 Schematic of planar lateral-field optoelectronic tweezers (PLOET) for nanowire assembly [62]. The device consists of an unpatterned amorphous silicon layer over an aluminum electrode array, fabricated on an oxidized silicon wafer. Paired triangular optical patterns create nanowire traps in between the metal electrodes.

The principle of operation of PLOET is slightly different from previous devices. Instead of the optical patterns switching electrodes on, as in the standard LOET device (see Chapter 5), the optical patterns are used to form conductive extensions of the metal electrodes. This creates high-field regions at the ends of illuminated regions.

An AC bias is placed across the electrode arrays, resulting in a uniform electric field between electrode fingers. To create a nanowire trap, optical patterns created by a DMD are projected onto the PLOET device. The optical setup is identical to the one presented in Chapter 6.4

As in the other incarnations of OET and LOET, the optical patterns act as virtual electrodes by lowering the impedance of the a-Si in the illuminated areas. However, in the case of PLOET, the optical patterns function as extensions of the metal electrodes. Paired triangular patterns extend from the metal electrodes, and create a trap that spans the tips of the triangular patterns (Figure 7.2). The simplified equivalent circuit model is

shown in Figure 7.3. The light patterns are used to modulate the conductivity of the a-Si film in the regions extending from the metal electrodes (Z_{PC1}). A section of a-Si is left unilluminated and in the high-impedance dark state (Z_{PC2}). Thus, when the optical patterns are activated, Z_{PC1} is reduced, creating low-impedance paths that act as extensions of the metal electrodes. The voltage is now dropped across the parallel network of Z_{PC2} and the liquid impedance, Z_L . This creates strong electric fields at the tips of the illuminated areas (Figure 7.4). The nanowires are attracted to these areas of strong electric field, and align between the triangular patterns. A typical triangular optical pattern has a tip diameter of 2 μm and a taper angle of 14 degrees. The gap between paired triangular patterns is adjusted to approximate the length of the trapped nanowire, which is typically 5 μm . The tips of the triangular patterns can be shifted in relation to each other, affording orientation control of the nanowires under manipulation.

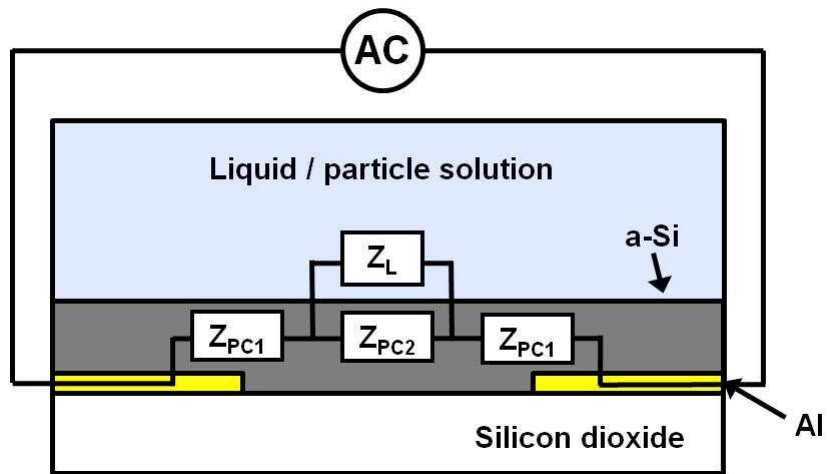


Figure 7.3 Simplified equivalent circuit model of the PLOET device.

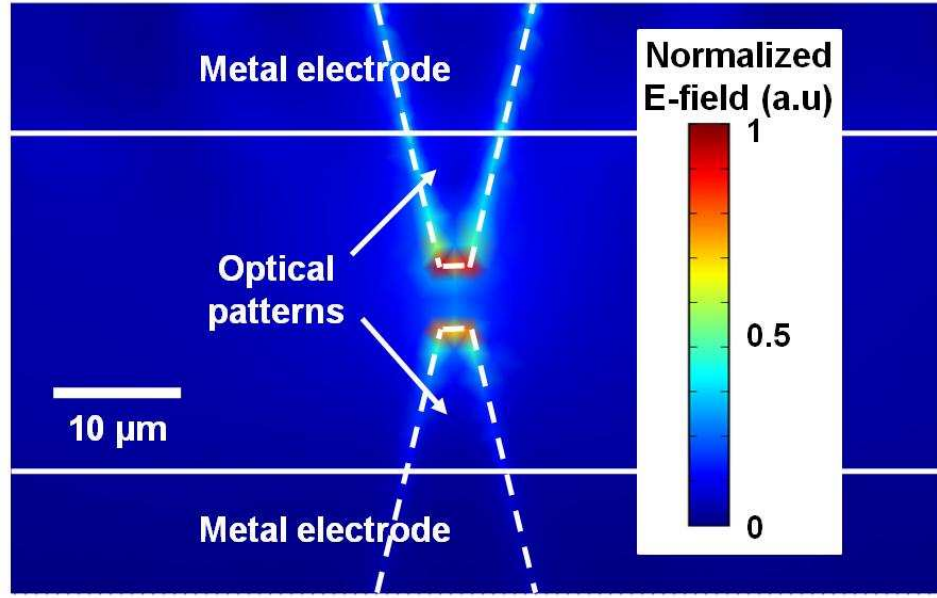


Figure 7.4 Finite-element simulation of the electric field profile across the PLOET electrodes.

7.3.2 Nanowire Rotation and Assembly

The capabilities of PLOET for nanowire orientation control and assembly are demonstrated [62]. Silver nanowires with diameters of 80 to 100 nm and lengths of 1 to 10 μm were suspended in ethanol, and introduced into the LOET device. The optical patterns can be used to transport nanowires parallel to the plane of the LOET device, and can control the nanowire orientation in both the x - and y -directions (Figure 7.5). Rotational control is achieved by adjusting the relative alignment of the triangular trapping patterns. Continuous rotation control has been performed over a range of ± 28 degrees. Further optimization should result in a larger range of orientation control.

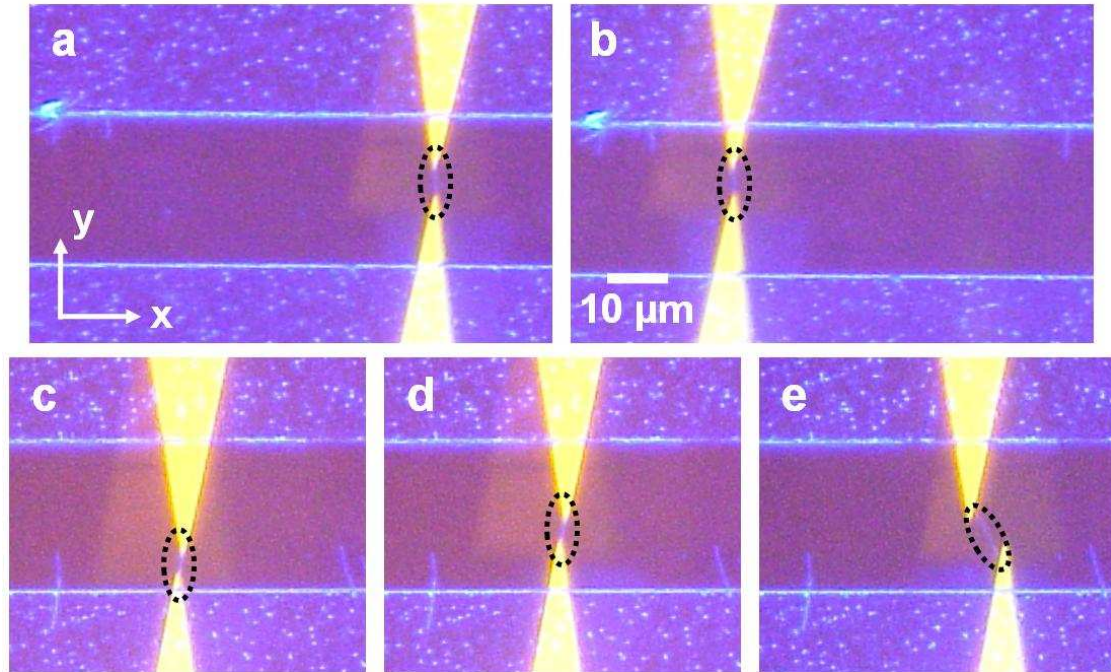


Figure 7.5 Trapping of silver nanowires using PLOET [62]. Aluminum electrodes are visible underneath the amorphous silicon layer, at the top and bottom of each image. Optical patterns, visible as the bright areas, are used to create nanowire traps. The nanowire positions are indicated by dashed circles. (a, b) Transport of a nanowire in the negative x -direction at a rate of approximately $3 \mu\text{m/s}$. (c, d) Transport of a nanowire in the positive y -direction. Other nanowires are weakly trapped at the edges of the electrodes, but can be moved by the LOET trap patterns. (e) Rotational control of a nanowire is achieved by moving the tips of the optical patterns relative to each other.

Orientation-controlled nanowire assembly can be combined with another advantage of PLOET: parallel manipulation. The goal of parallel nanowire assembly is to create a nanowire-based electronic or optoelectronic device. Our target is the creation of a red-green-blue (RGB) nanowire display. Nanowire LEDs have been demonstrated [114], but arrays have yet to be assembled.

Semiconductor nanowires that can be used to form the red, green, and blue pixels include cadmium selenide (CdSe), cadmium sulfide (CdS), and zinc oxide (ZnO) nanowires, respectively. The measured photoluminescence of the three types of

nanowires is shown in Figure 7.6. Currently, the ZnO and CdS nanowires both exhibit photoluminescence in the green wavelengths; however, tuning of the composition of the ZnO nanowires can result in a blue-shift of the photoluminescence peak [115]. Alternatively, it is possible to obtain blue wavelengths using other semiconductor nanowire materials [116].

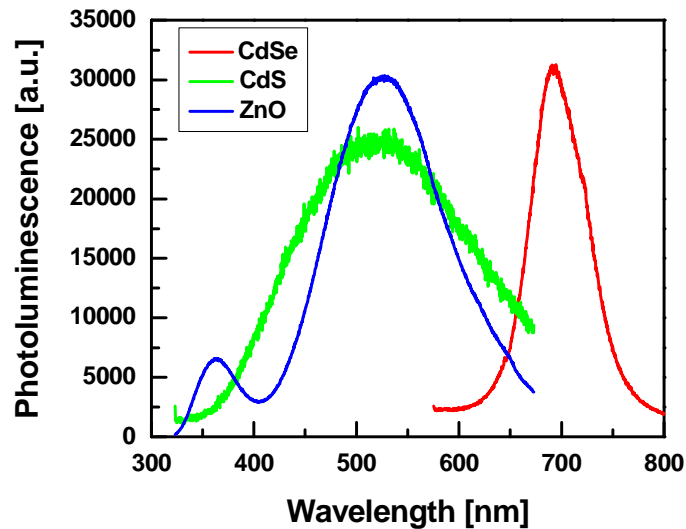


Figure 7.6 Measured photoluminescence of semiconductor nanowires for a red-green-blue nanowire LED display.

The proof-of-concept of the nanowire array assembly is demonstrated here with the assembly of four individual nanowires into a regularly-spaced array (Figure 7.7). In this experiment, silver nanowires are used, as the grown CdSe nanowire samples were not as pure. However, manipulation of all types of semiconductor nanowires is possible using PLOET.

Each nanowire of the array is trapped in parallel by a pair of optical patterns. The nanowires are positioned at with a 200-kHz AC signal at a voltage of 300 mVpp. Once

the nanowires are trapped in the desired locations, the voltage is increased to 2.8 V_{pp} to anchor the nanowires to the surface. After the suspension solution dries, the nanowires remain assembled in a regular array on the substrate (Figure 7.7e).

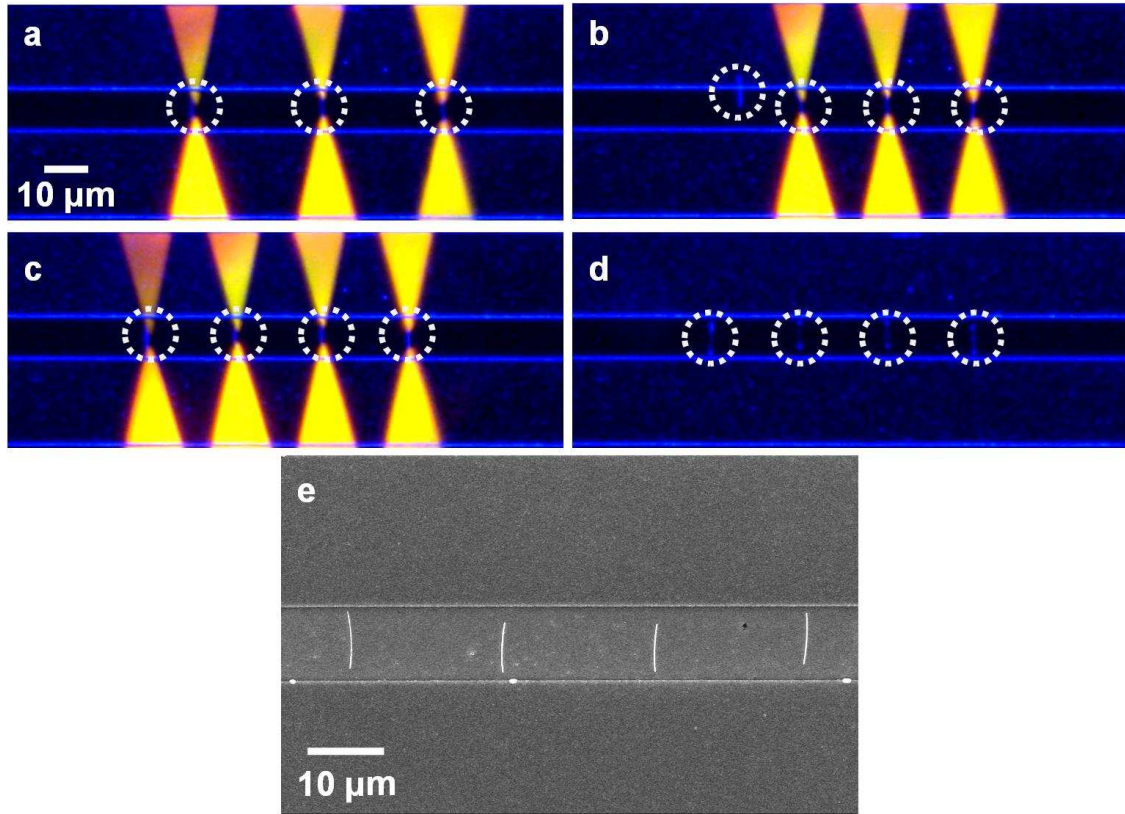


Figure 7.7 Fabrication of a silver nanowire array [62]. (a) Three nanowires have been trapped in parallel. (b) The nanowires are arranged in a closer, more regular spacing. Another nanowire can be seen to the left of the array. (c) The fourth nanowire is trapped by another set of optical patterns. The applied voltage is increased to assemble the nanowires on the surface of the device. (d) An SEM image of the nanowire array.

Chapter 8

Integration of Optoelectronic Tweezers and Electrowetting-on-Dielectric Devices

8.1 Motivation

Single-cell studies often require subjecting individual cells to varying environmental conditions and stimuli to study their response to different concentrations of nutrients and chemicals. However, controlling the environmental conditions at the single-cell level in the same continuous microfluidic device is inherently difficult. Cellular response to a single or small number of stimuli has been demonstrated [11, 117, 118], but there have been few attempts to conduct multiplexed assays [119, 120], since this involves a complex network of pumps, microvalves, latches, and interconnected channels [121].

The isolation of environments for individual cells is an inherent feature of droplet microfluidics [122], where fluids are handled in the form of discrete droplets as opposed to continuous flow through channels. Droplet microfluidics driven by electrowetting-on-dielectric (EWOD) is an attractive lab-on-a-chip platform, due to its simple design, low power consumption, and reprogrammable fluid paths [123-125]. Fluids are handled in the

form of droplets driven by electrically controlling the wetting property of a dielectric surface. The driving force is a combination of electrowetting (Laplace forces generated by an asymmetric contact angle change) and dielectrophoresis [126, 127]. Multiple droplet paths can be simultaneously controlled by properly sequencing the application of voltage to an underlying electrode array. Operations such as creating, merging, moving and splitting droplets can be performed on the EWOD platform [128, 129], which allows precise spatial and temporal control over the reagents in each droplet. Cross-contamination during droplet movement is avoided by appropriately choosing the paths for various reagents. Unlike continuous flow microfluidic channels, the droplets are isolated from their surroundings, and can act as microreactors supplied with independent, multiplexed stimuli.

Cell separation is a key function for lab-on-a-chip platforms. EWOD-based systems can use differences in particle properties between the target and non-target particles to segregate a mixed population, followed by target particle isolation by splitting the droplet. Mechanisms explored for target separation and concentration inside a droplet include electrophoresis [130], dielectrophoresis [64, 131] and magnetism [132, 133]. Although some biochemical applications of EWOD have been shown [134-136], very few have dealt with cell studies [136]. Furthermore, EWOD actuation has not been demonstrated at the single-cell level.

A device that combines the single-particle manipulation capabilities of OET and the droplet handling of EWOD would be an extremely valuable tool for research in cellular biology. Here, we demonstrate the integration of OET and EWOD to create a powerful lab-on-a-chip platform.

8.2 Electrowetting-on-Dielectric (EWOD)

Electrowetting-on-dielectric (EWOD) uses electric charge to change the free energy on a dielectric surface [124]. As a result, the wettability of the surface is altered, and liquid droplets at the surface experience a change in contact angle, θ (Figure 8.1). The change of the contact angle as a function of applied voltage, V , can be derived from Lippmann's equation and Young's equation (see [124] for derivation), and is given by [124]:

$$\cos\theta(V) - \cos\theta_0 = \frac{\epsilon_0\epsilon}{2\gamma_{LV}t} V^2 \quad (8.1)$$

where θ_0 is the equilibrium contact angle at $V = 0$ V, ϵ_0 is the vacuum permittivity, ϵ is the permittivity of the dielectric layer, γ_{LV} is the liquid/vapor interfacial tension, and t is the thickness of the dielectric layer. EWOD devices employ a hydrophobic dielectric layers or dielectrics coated with an additional hydrophobic layer, creating a large θ_0 . Applied voltages create a reduced contact angle. If the contact angle is reduced only on one side of the droplet, the droplet will move in towards the region the reduced contact angle. Droplet movement on a typical EWOD device is shown in Figure 8.2 [124].

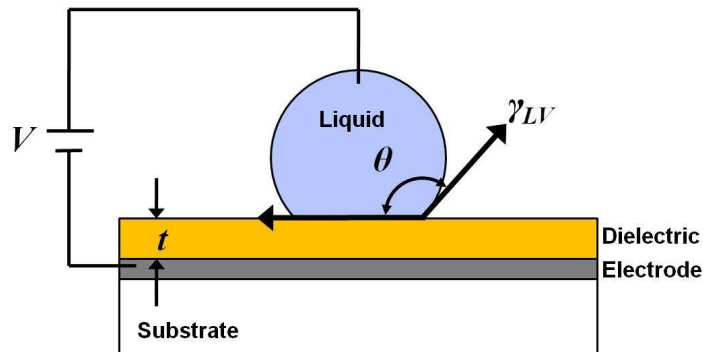


Figure 8.1 Principle of electrowetting-on-dielectric. An applied voltage changes the contact angle at the liquid/dielectric interface.

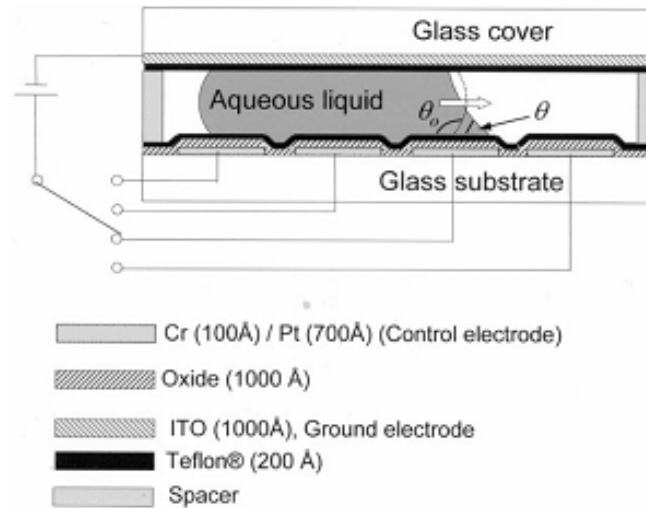


Figure 8.2 Typical EWOD device [124].

8.3 Integrated OET / EWOD Device

The easiest method to create an integrated device that retains the functionality of both OET and EWOD is to use a two-substrate device, where one substrate consists of the photosensitive OET electrode, and the other consists of EWOD electrodes (Figure 8.3) [64]. However, EWOD devices require a relatively thick dielectric layer (typically 0.5 to 1.5 μm of silicon dioxide or parylene) over the actuation electrodes to prevent electric breakdown and current leakage across the droplet. The presence of the thick dielectric layer precludes the use of the EWOD electrodes as the opposing electrode for OET operation, as the dielectric will absorb most of the applied voltage, greatly reducing the OET force in the droplet.

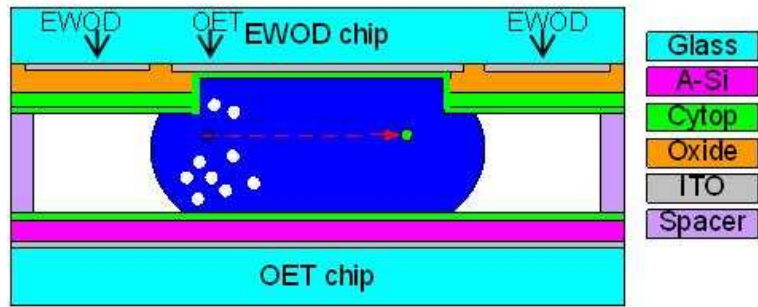


Figure 8.3 Cross-section of the integrated OET/EWOD device [64]. The top glass substrate has EWOD electrodes except for the central electrode, which is used for OET. The bottom glass substrate consists of the a-Si photosensitive OET electrode. Silicon dioxide and Cytop® are patterned on EWOD chip, except for the OET region, which only has a thin hydrophobic layer.

In order to circumvent this issue, a region of the EWOD device has no dielectric layer. This corresponds to an area in which OET manipulation can be performed, but not EWOD actuation. Conversely, OET manipulation is ineffective in the other regions of the EWOD device. Moving the droplet of interest into and out of the OET region must be performed using EWOD electrodes surrounding the region. Once the droplet is in the OET region, manipulation of particles within the droplet can be performed. Thus, there is a design trade-off between relative sizes of the OET electrode and the EWOD side-electrodes. Larger side-electrodes make droplet manipulation easier, but reduce the area available for particle manipulation by OET. The electrode layout (Figure 8.4) was chosen as a result of this trade-off.

The operating concept of the integrated OET/EWOD device is shown in Figure 8.4 [64]. A droplet containing the cells is positioned over the OET region using the adjoining EWOD electrodes (Figure 8.4a). Using OET, all cells are swept to one side of the droplet, then individual cells are separated to the other side, based on differences in visual or

dielectric properties (Figure 8.4b). Finally, EWOD is used to create a smaller droplet containing only the selected cell(s) (Figure 8.4c).

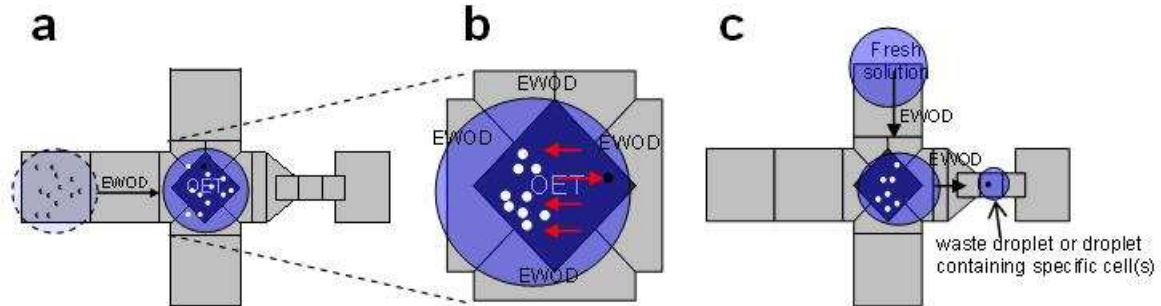


Figure 8.4 Schematic of the integrated OET/EWOD device [64]. The light gray areas represent EWOD electrodes, and the dark gray represents the OET manipulation area. (a) A droplet containing cells is transported to the OET area using EWOD. (b) Using OET, cells are swept to left and individual cells are selected based on dielectric properties or visual differences. The droplet position relative to the OET area can be adjusted by the EWOD side-electrodes. (c) Using EWOD, desired cells are removed by generating a droplet, or waste medium is removed as droplets. A fresh droplet can be added from other directions to replenish cell medium.

Another operating mode can be used to culture cells on chip. Maintaining a viable cell environment requires replenishing the cell culture medium. Using EWOD operations, wastes and toxins can be removed, and replaced by fresh media while the cells are held by OET.

The integrated EWOD device was fabricated by patterning electrodes in a 140-nm-thick ITO layer. A 700-nm-thick layer of SiO₂ was deposited by PECVD over the electrodes, followed by the spin-coating of a 200-nm-layer of Cytop[®] (Asahi Inc.). Both the SiO₂ and Cytop[®] layers were removed in the area reserved for OET manipulation, although a 20-nm-thick layer of Cytop[®] was spin-coated over the OET manipulation region to maintain hydrophobicity.

The integrated OET device consists of a standard a-Si electrode, as discussed in Chapter 2.7. However, the surface of the a-Si must be rendered hydrophobic, so a 20-nm-thick Teflon AF[®] layer was spin-coated on the a-Si layer.

8.3.2 Experimental Setup

The experimental setup of the integrated OET/ EWOD system is the same as described in Chapter 1.3.3. A liquid-crystal spatial light modulator and a 635-nm laser were used to generate image patterns for optical manipulation. The optical patterns are focused onto the OET device through a 5× objective lens. Image processing software was used to determine the particle characteristics, and generate the corresponding optical manipulation patterns to separate particles.

8.3.3 Experimental Results

A droplet containing 20- μm -diameter polystyrene beads was moved into the OET region using the EWOD side-electrodes (Figure 8.5a, b) [64]. The side-electrodes can also be used to pull the droplet in different directions, so that particles initially outside the OET region can be “captured” with OET. Cutting of the droplet was also demonstrated (Figure 8.5c, d) using the adjoining EWOD electrodes.

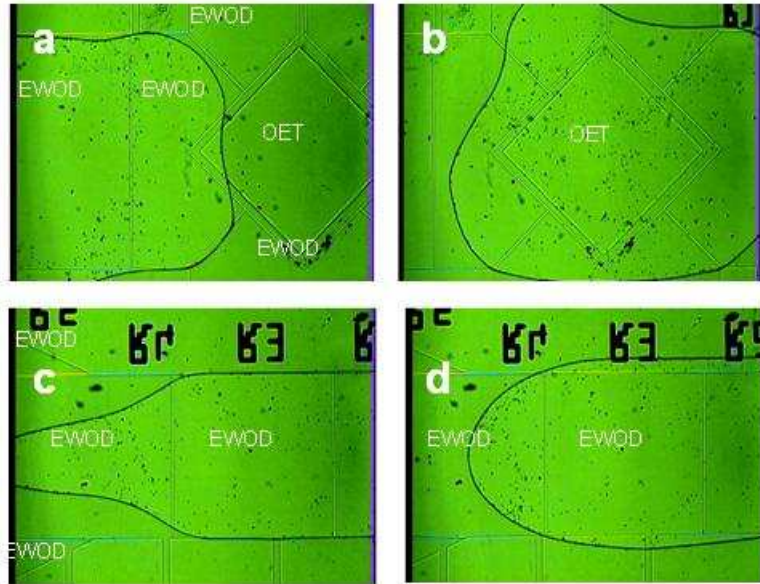


Figure 8.5 Droplet manipulation by EWOD [64]. (a, b) EWOD is used to transport a droplet with beads into OET manipulation region. (c, d) EWOD cuts a droplet out of the OET region as in Fig. 2(c). The dielectric pattern inside the OET electrode (rotated square) marks active OET region. Surrounding EWOD electrodes are used to move droplets into, out of and around OET region.

Once the droplet is moved into the OET region, an image-feedback-controlled optical pattern was used to manipulate individual particles in the droplet. Particles were identified by the image-processing software and swept to the left (Figure 8.6a) [64]. A user-controlled optical pattern can also be used to sweep particles in OET manipulation area (Figure 8.6b). Nearly all particles responded to OET manipulation, although two particles were adhered to the surface of the OET substrate (Figure 8.6c). A single particle from the group that was swept to the left was selected by the user, and an optical pattern was generated to move only this particle to the right edge of the droplet (Figure 8.7) [64].

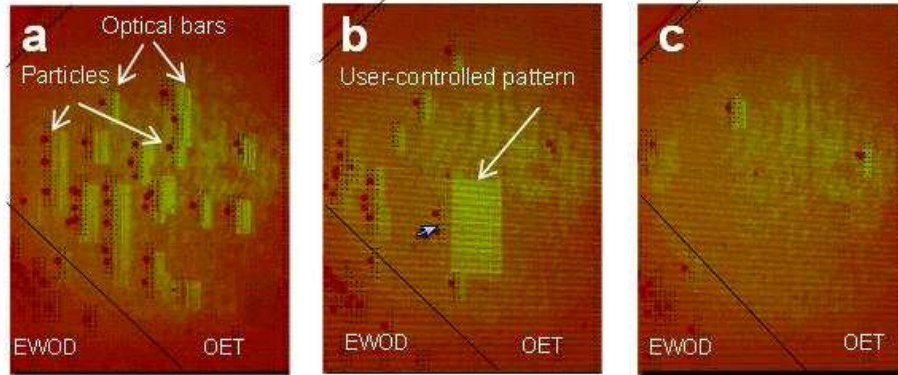


Figure 8.6 Particles swept to the left side of the image using OET [64]. (a) Each particle (dark dot) is pushed to left by an optical line pattern. (b) User-controlled optical patterns can also be used to sweep particles. (c) Nearly all particles in the OET region have been swept to the left (most are out of the field-of-view). The edges of the OET manipulation region are added for clarity.

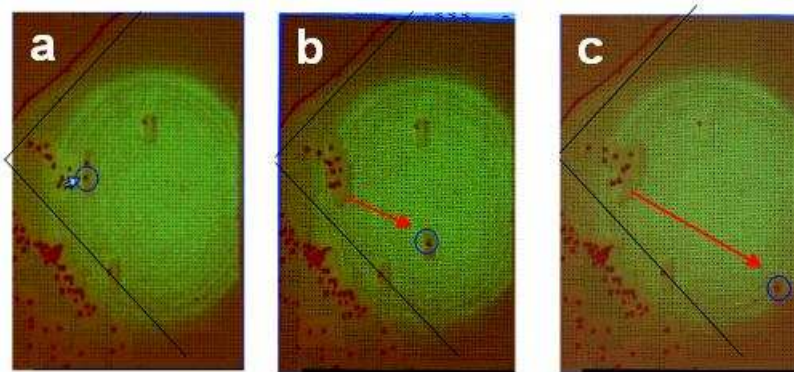


Figure 8.7 Individual particle control using OET [64]. (a) A specific particle (circled) is chosen by the user, and transported to the right. (b, c) The selected particle is moved away from the others, as indicated by the arrow. The edges of the OET manipulation region are added for clarity.

8.3.4 Design Issues

While the functions of both EWOD and OET were individually demonstrated the integrated device, the mutually exclusive nature of the OET and EWOD operational areas led to difficulties in demonstrating a complete sequence of EWOD-OET operations. The lack of OET manipulation in the EWOD region restricts particle manipulation to the

relatively small OET region, while the lack of EWOD actuation over the OET region presents difficulties for sustaining the particle distribution against microfluidic flow (Figure 8.8).

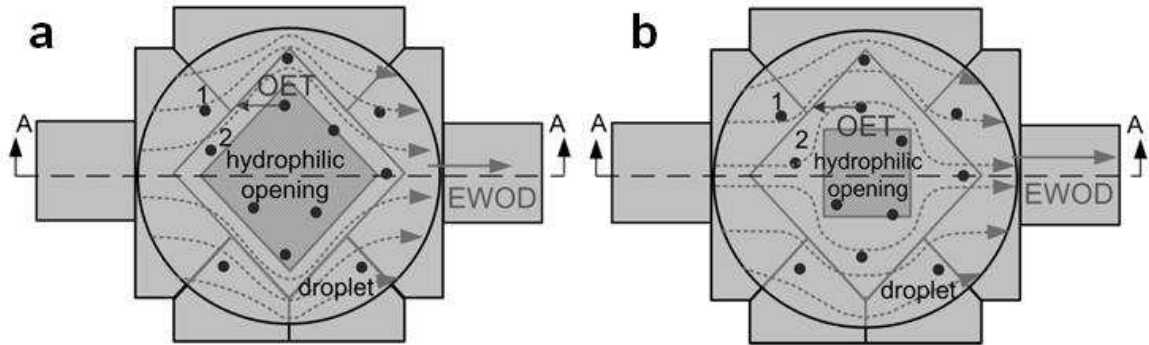


Figure 8.8 EWOD electrode arrangements around the OET manipulation region with two alternative shapes for the hydrophilic opening. During EWOD droplet actuation, the fluid in the hydrophilic region remains stagnant (indicated by the flow lines), while causing flow near the meniscus to grow stronger. This creates strong viscous forces on particles outside the hydrophilic region, such as those labeled 1 and 2.

Since the manipulation of wetting properties is not possible in the OET region, the droplet size is chosen to be bigger than the OET region, and microfluidic operations are performed with the help of the EWOD electrodes surrounding the OET region. Moreover, the hydrophobicity of the OET region must be chosen carefully. Three possibilities may be considered, based on the size of the hydrophilic opening in Figure 8.8.

Case 1 – the entire OET region is hydrophilic. When a droplet enters the OET region, it readily wets and fills the entire OET region, and overflows onto the EWOD electrodes outside the OET region. While OET manipulation can be performed on particles inside the OET region, manipulation on particles in the droplet that lie outside the OET region is problematic. One possibility is to manipulate the droplet so that particles outside the OET region are introduced into the OET manipulation area. However, when more fluid is

pulled in by EWOD towards the hydrophilic OET region, it is unable to displace the fluid already present. Thus, the hydrophilic site presents a stagnant zone that flow lines circumvent, preventing new particles from being introduced into the OET region.

Case 2 – the entire OET region is hydrophobic. A hydrophobic OET region allows the free exchange of fluids and hence particles between the OET and EWOD regions, and the appropriate surrounding electrodes can be employed to introduce droplets into the OET region. However, subsequent microfluidic movements may tend to dry the OET region, causing the droplet meniscus to sweep across it. OET force is too weak to oppose particle movement against the interfacial force of the meniscus, and thus the OET-generated particle distribution is disturbed.

Case 3 – the OET region is part hydrophilic and part hydrophobic. The two cases considered thus far suffer from either no fluidic movement or too much fluidic movement in the OET region as a result of EWOD actuation. A solution to this issue was sought by making only part of the OET region hydrophilic, leaving the rest covered with a thin hydrophobic layer (Figure 8.8). Fluid exchange between the hydrophobic OET region and the EWOD region would enable particles originally outside the OET region to enter the OET manipulation area. At the same time, the hydrophilic site does not allow the droplet meniscus to sweep across the entire OET region, preventing the complete disturbance of OET-driven particle re-arrangement.

Theoretically, this design could allow combined EWOD and OET operations. However, in practice it is rather difficult to capture all the particles in the droplet (including those initially outside the OET region) for OET manipulation. The presence of the central hydrophilic region tends to push the flow lines away from the center (and

hence the OET region) towards the meniscus (Figure 8.8). As a result, many particles are still excluded from the OET region (particle 1 in Figure 8.8).

It is also difficult to keep the OET-generated particle distribution undisturbed during EWOD operations such as droplet cutting. Although the hydrophilic opening prevents the meniscus from completely sweeping across the OET region, there is still significant fluidic movement during EWOD actuation. OET cannot maintain the particle distribution against this movement, particularly in the hydrophobic part of the OET region (particle 2 in Figure 8.8).

8.4 Integrated Planar LOET / EWOD Device

In order to solve the issues discussed in Chapter 8.3.4, a second-generation device was designed and tested. This device uses a PLOET device (discussed in Chapter 7.3) instead of the standard OET device, and a typical EWOD device, with no special OET actuation area.

The PLOET device no longer needs an opposing electrode, so the EWOD device can be left unmodified, with no patterning of the dielectric or hydrophobic layers. This eliminates the “OET only” region of the first-generation device, and also expands the OET region into the previously “EWOD-only” regions. Since the EWOD and OET regions are no longer mutually exclusive, the problems described above for the first-generation device are no longer encountered.

8.4.1 Fabrication

The EWOD electrodes are each 1 mm², and were defined in a 140-nm-thick ITO layer on a 700- μ m-thick glass substrate (TechGophers Inc.). A chromium/gold layer (10

nm/100 nm) was deposited and patterned to define the contact pads and electrode labels for easier visualization. Next, a 1- μm -thick silicon nitride layer was deposited using PECVD, and patterned to define the dielectric layer. A 1- μm -thick Cytop[®] layer was spin-coated and annealed at 200°C to make the surface hydrophobic.

The LOET devices were fabricated as described in Chapter 7.3.1. A 20-nm-thick layer of Teflon AF[®] was spin-coated on the a-Si and annealed at 150°C, rendering the surface hydrophobic. Since OET force is strongest near the PLOET device, and since particles and cells settle due to gravity, the LOET device was placed on the bottom. A 100- μm -thick spacer is used between the two substrates.

8.4.2 Experimental Setup

The integrated PLOET/EWOD device used the optical setup described in Chapter 6.4. Briefly, the output of a computer projector (Dell 2400MP) was collimated and focused onto the LOET substrate through a 10 \times objective lens, which also serves as the observation objective. A fiber illumination is used to provide the background illumination necessary to view the microparticles, and a CCD camera is used to capture the microscope images.

The PLOET was biased at 3 to 5 V_{rms} at 200 kHz, while the EWOD device used 120 V_{rms} at 20 kHz. During the PLOET manipulation, one of the electrode arrays was connected to the LOET voltage supply, while the other was grounded. During EWOD actuation, the PLOET electrodes act as the ground electrode. Grounding one array of PLOET electrodes is sufficient, although EWOD actuation was found to be better when both the arrays were grounded, particularly during droplet cutting.

Live HeLa cells were suspended in an isotonic buffer containing 8.5% sucrose and 0.3% dextrose ($\sigma = 5$ mS/m). Under these conditions, the cells experience positive OET, and are attracted to the regions illuminated by the optical patterns. Unfortunately, the hydrophobic surface required for EWOD actuation is prone to fouling from the cells, and the hydrophobic requirement excludes the use of PEG coating. However, the addition of small quantities of surfactant prevents cell adhesion, allowing the actuation of cell samples using EWOD [137]. Therefore, 0.2% Pluronic surfactant F68 (Sigma-Aldrich) was added to the solution.

8.4.3 Experimental Results

The sequence of EWOD and PLOET functions is shown in Figure 8.9. The droplet position prior to PLOET manipulation was experimentally determined to minimize the collected cells from being re-distributed by the droplet movement during a subsequent cut. The droplet is positioned accordingly using EWOD (Figure 8.9a, b).

Next, PLOET operations are performed on the cells, in this case moving the cells from the lower (“depleted”) to the upper (“collected”) region of the droplet (Figure 8.9b, c). Since the field-of-view of the microscope is small with respect to the EWOD electrode dimensions, multiple sweeps may have to be performed to cover the entire droplet area (Figure 8.9c, d). After the PLOET manipulation is completed, the droplet is split using EWOD (Figure 8.9e), and separated into the “collected” droplet that contains most of the collected cells, and the “depleted” droplet with a few cells of interest (Figure 8.9f).

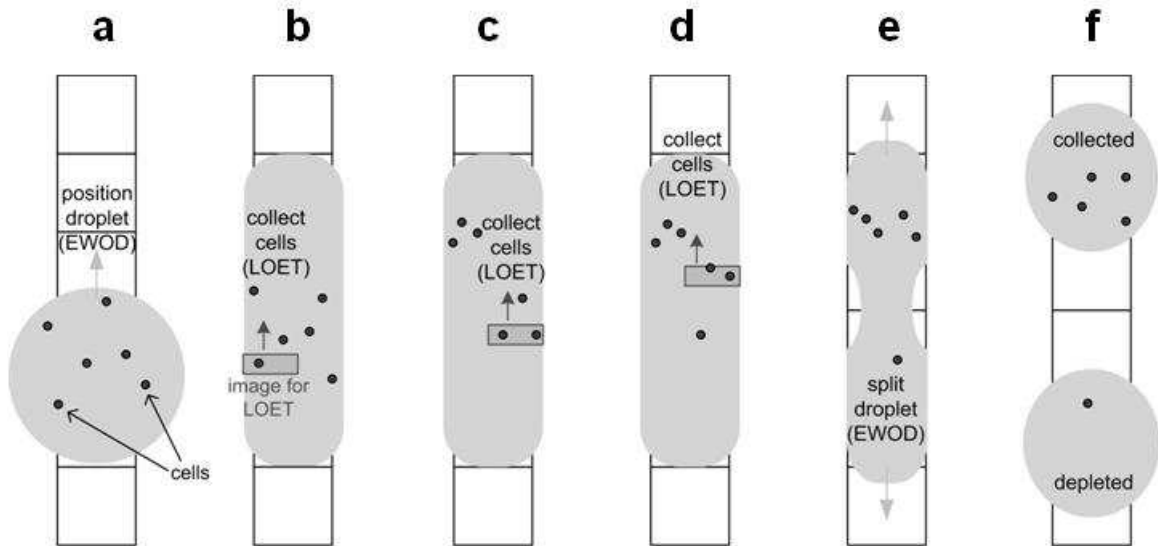


Figure 8.9 Schematic of the operations performed on the integrated PLOET/EWOD device. The light arrows indicate droplet movement by EWOD while the dark arrow indicates the movement of the PLOET optical pattern. (a) A droplet containing cells is placed on the device. (b) To avoid disturbing the PLOET-generated particle distribution due to fluidic movements during the droplet cutting step, the droplet is positioned properly by EWOD prior to PLOET operations. The PLOET image pattern is then projected and moved across the droplet, transporting the cells upwards. (c) Since the droplet dimensions are larger than the PLOET image area, cell manipulation may be repeated over multiple regions to cover the entire droplet. (d) All but a few cells have been concentrated in one region. (e) The droplet is subsequently split using EWOD. (f) Cells have been separated into the collected droplet and the depleted droplet.

A 350-nL droplet containing live HeLa cells at a concentration of 6×10^4 cells/mL is placed on the integrated device (Figure 8.10a). The droplet is stretched by EWOD, and positioned for the subsequent steps (Figure 8.10b). Next, cell manipulation is performed using PLOET; cells are collected upwards by sweeping a computer-generated optical pattern from the bottom-to-top across the field of view (Figure 8.10b, c). The bright spot in Figure 8.10b-d shows the entire illuminated area; the optical pattern within the illuminated area can be seen more clearly in Figure 8.11.

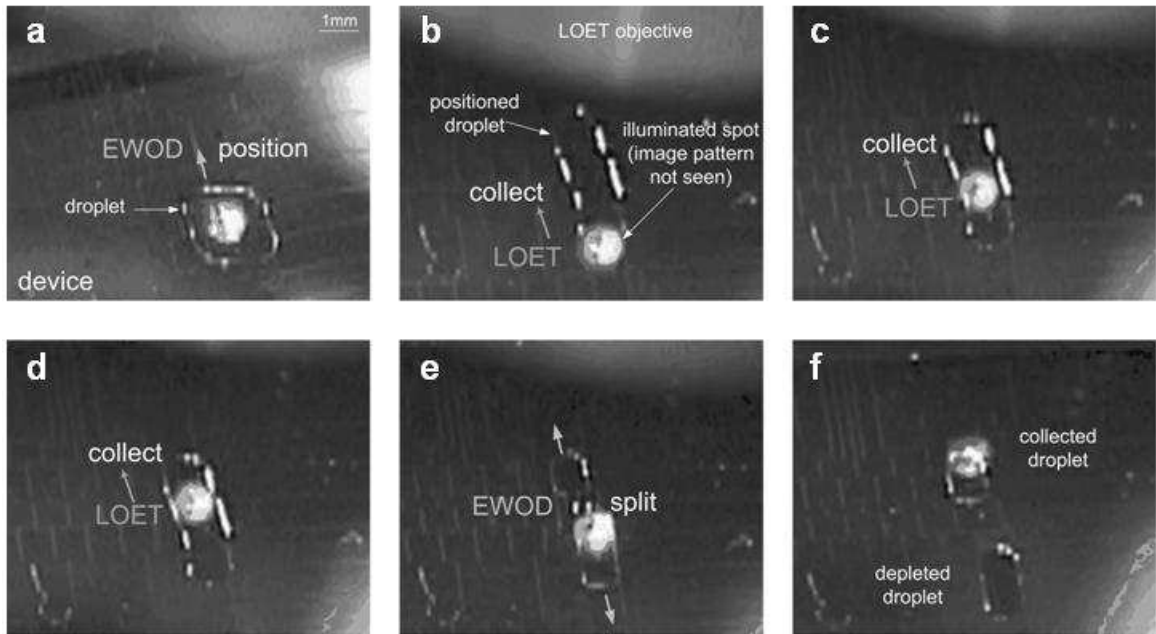


Figure 8.10 EWOD functions during the operation of the integrated PLOET/EWOD device. (a) A 350-nL droplet containing HeLa cells is placed on the integrated device. (b) The droplet is positioned so the PLOET-generated cell distribution is not disturbed during the droplet cutting. PLOET manipulation is performed starting from the bottom of the stretched droplet. (c) Collection of the cells from the lower (“depleted”) region into the upper (“collected”) region of the droplet. (d) The cell collection is performed across the width of the droplet to move most of the cells into the collected region. (e, f) After collection, the droplet is split into the “collected” (top) and “depleted” (bottom) droplets.

The EWOD electrode features (outlined) can be used as reference to see the movement of cells by PLOET. Since the cells experience positive DEP, they are attracted to the optical pattern (Figure 8.11a). As the pattern moves upwards, the cells are transported (Figure 8.11b, c). More cells are collected the pattern moves upwards towards the collection area (Figure 8.11d to f). As the droplet is larger than the microscope field-of-view, multiple sweeps are performed, each time transporting the cells to the collected region. After the PLOET operations are completed, the droplet is split using EWOD by

stretching it in both directions (Figure 8.10e), resulting in “collected” (top) and “depleted” (bottom) droplets (Figure 8.10f).

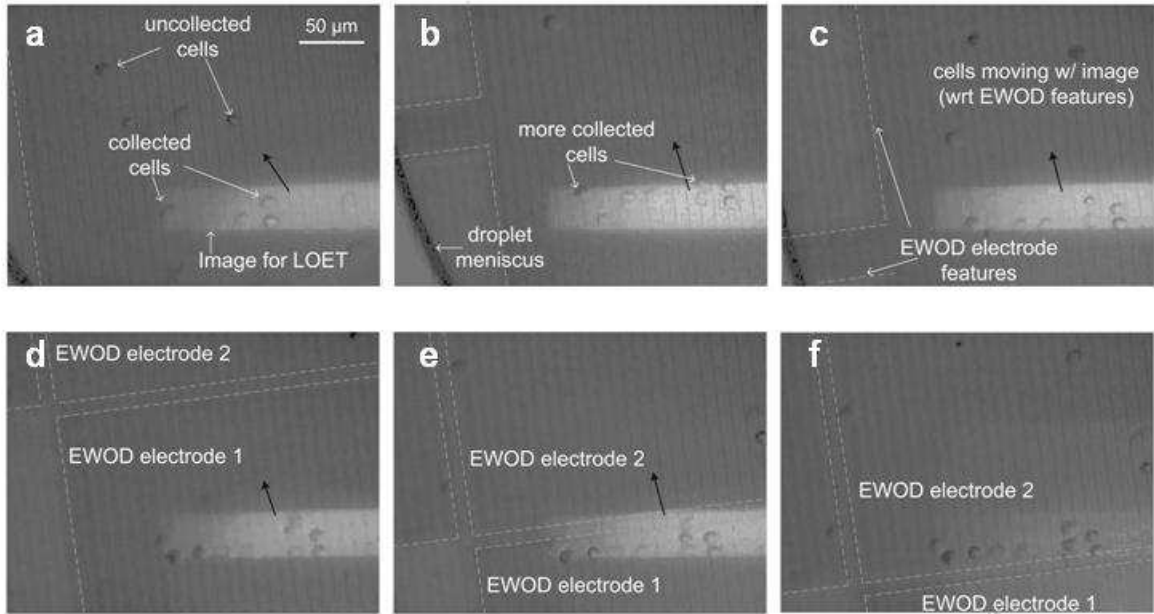


Figure 8.11 PLOET manipulation of HeLa cells within a droplet. The dark arrows indicate the movement direction of the optical pattern. (a) Since the cells experience positive OET, they are attracted to the pattern. (b) As the pattern moves up, the pattern more cells are collected. (c) The movement of the cells can be seen with respect to the EWOD features. (d to f) The pattern sweeps across multiple EWOD electrodes starting from the bottom of the droplet, collecting all the cells in the upper (“collected”) region.

In this experiment, ~19 live cells were present in the original droplet. Subsequently, 13 cells were concentrated into the collected droplet, while 6 cells remained in the depleted droplet. A few of the cells that remained in the depleted droplet were unintentional, as cells tend to stick the PLOET surface over the relatively long distance of manipulation. In order for the cells to be separated into discrete droplets, they must be transported approximately 2 to 3 mm due to the EWOD electrode dimensions.

Furthermore, dirt particles present in the droplet or on the device surface can also block cells from being transported.

8.4.4 Future Improvements

The demonstration of sequential EWOD and OET operations for cell handling on an integrated device is a significant development. However, some obstacles remain. One of the issues is cell adhesion in the device, which is exacerbated by the large 1 mm x 1 mm EWOD electrodes. Cells must be manipulated by PLOET over a distance of 2 to 3 mm, which was successful for many cells, but not all. One solution is to scale down the EWOD dimensions, requiring PLOET manipulation to occur over much shorter distances.

Chapter 9

Optically-Actuated Thermocapillary Forces in Optoelectronic Tweezers Devices

9.1 Motivation

Another notable phenomenon that can occur in the optoelectronic tweezers device is the creation of a thermal gradient due to laser absorption in the a-Si electrode. However, unlike the electrothermal effects described in Chapter 2.9.2, this does not depend on the electric field within the OET device, and can occur in the complete absence of an electric field. This optically-induced thermal effect can be used to transport gas bubbles within an OET device, or in a microfluidic device with an a-Si layer similar to the OET structure.

Gas bubbles in microfluidic devices can serve many functions, including acting as pumps [138], valves [139], mixers [140], and switches [141], and performing Boolean logic operations [142]. Typically, the bubbles are carried passively by fluid flow in microfluidic channels. To achieve the active positioning of gas bubbles or liquid droplets, many different methods may be used, such as dielectrophoresis [143], electrowetting

[144, 145], optoelectrowetting [146], and evaporation [147]. Another method is to use thermal gradients to drive the motion of gas bubbles in liquids (or liquid droplets in air or other immiscible liquids) by altering the surface tension. Surface tension is dependent on several factors, including temperature; thus, a thermal gradient creates a surface temperature gradient, which drives a fluid motion, known as thermocapillary force or the thermal Marangoni effect [148]. As a result, sufficient thermal gradients can drive the motion of bubbles [138, 141, 148], droplets [149-152], or thin films of fluids [153, 154].

Typically, thermocapillary forces are created by integrated resistive heating elements [149, 152, 155]. However, recent work has shown that the thermal gradients necessary to generate thermocapillary-driven bubble or droplet movement can be created by the absorption of a laser beam in a liquid [156-159]. Such optically-controlled actuation has advantages over conventional dielectrophoresis, electrowetting, and resistive heating methods, as it is easier to address a large array of bubbles using optical patterns. Furthermore, optically-controlled actuation is more flexible and more easily reconfigurable than resistive heating elements. However, the properties and chemistry of the liquids compatible with this method are limited, since an optically-absorbing liquid is required.

Here, we demonstrate the trapping and transport of air bubbles, driven by an optically-actuated thermocapillary force arising from the laser heating of an absorbing substrate (the a-Si electrode of the OET device) [160]. The use of an absorbing substrate creates more flexibility than using absorbing liquids, as it makes optically-actuated thermocapillary forces independent of the optical properties of the liquids or gases. Furthermore, as mentioned earlier, the a-Si electrode of the OET device is inexpensive,

allowing it to act as a disposable surface to minimize the cross contamination of sensitive samples. Other work that relies on the heating of a substrate produces Marangoni forces via surface plasmon heating of a thin gold film on a quartz substrate, which is more expensive to produce [161].

9.2 Theory

The optically-induced heating of the absorbing substrate creates a thermal gradient in the substrate and the liquid media. This thermal gradient affects the surface tension of the liquid media, as most liquids have a constant, negative value of $\partial\sigma/\partial T$, where σ is the surface tension and T is the temperature. The change in surface tension is directly proportional to the change in temperature:

$$\nabla\sigma = \frac{\partial\sigma}{\partial T}\nabla T \quad (9.1)$$

Thus, the presence of a temperature gradient will decrease the surface tension in the warmer region, creating a flow toward the colder region as the liquid attempts to minimize the total surface energy. As a result of this thermally-induced liquid movement, bubbles in the liquid move toward the high-temperature regions, such as those created by optically-induced heating. Once a bubble is centered above a radially-symmetric thermal gradient, it is stably trapped, as the thermally-induced forces balance.

9.3 Experimental Setup

In order to create the optically-actuated thermocapillary forces, we utilize the a-Si electrode of an OET device, consisting of a 0.85-mm-thick glass slide coated with a 100-nm-thick layer of indium tin oxide, followed by a 1- μm -thick layer of hydrogenated amorphous silicon (a-Si:H), which absorbs light in the visible and UV wavelengths

(Figure 9.1) [160]. A 100- μm -high fluidic chamber was formed between the absorbing substrate and a 1.1-mm-thick glass slide and filled with approximately 20 μL of silicone oil (Dow Corning 200[®] fluid). Air bubbles are trapped during the loading of the fluidic chamber, with volumes ranging from approximately 85 pL to 23 nL. Contact angle measurements at the oil/air/substrate interface show that the silicone oil completely wets the a-Si:H surface. The laser source that provides the optically induced heating is a 10-mW, 635-nm semiconductor laser. At this wavelength, it was empirically determined that the a-Si:H-coated substrate absorbs 94% of the incident light, not accounting for reflections at the air/substrate and substrate/liquid interfaces. The output of the semiconductor laser is expanded to fill the aperture of a 20 \times microscope objective, which focuses the beam to a 6- μm -diameter spot on the surface of the absorbing substrate. The laser intensity is controlled with a variable attenuator, and the laser power is monitored using an optical power meter (Hewlett-Packard 8153A).

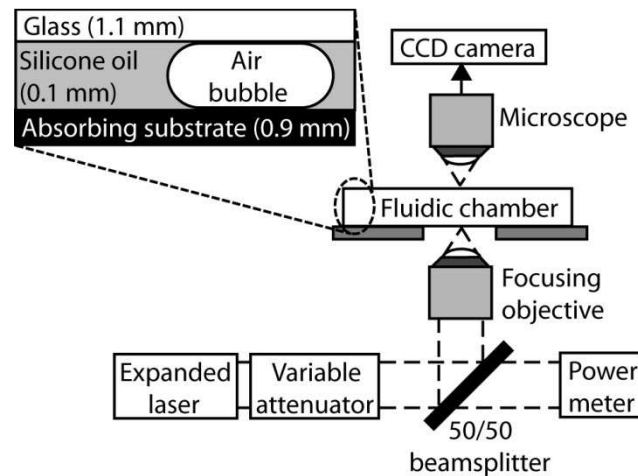


Figure 9.1 Experimental setup for the optically actuated thermocapillary movement of air bubbles [160]. A 10 mW, 635 nm laser is focused onto the absorbing substrate of a fluidic chamber by a 20 \times objective lens. Air bubbles in the silicone oil have a contact angle of approximately 180 $^\circ$, as the oil completely wets the surface of the substrate.

9.4 Experimental Results

The optically-actuated thermocapillary movement of a 114- μm -diameter air bubble in silicone oil is shown in Figure 9.2 [160]. The air bubble is initially positioned directly over the area illuminated by the laser (Figure 9.2a). The laser illumination position is subsequently scanned across the substrate by manually adjusting the position of the focusing objective relative to the fluidic chamber. From the original location, the laser spot is translated in the positive y -direction (Figure 9.2b), then in the positive x -direction (Figure 9.2c), and then in the negative y - and negative x -directions (Figure 9.2d). The dashed circle in Figure 9.2d indicates the initial position of the bubble, and the dashed line indicates the approximate trajectory. The silicone oil/air meniscus is visible in the upper-left corner of each image as a reference. The image sequence in Figure 9.2 spans 6.2 s, during which the bubble attains velocities of approximately 800 $\mu\text{m/s}$.

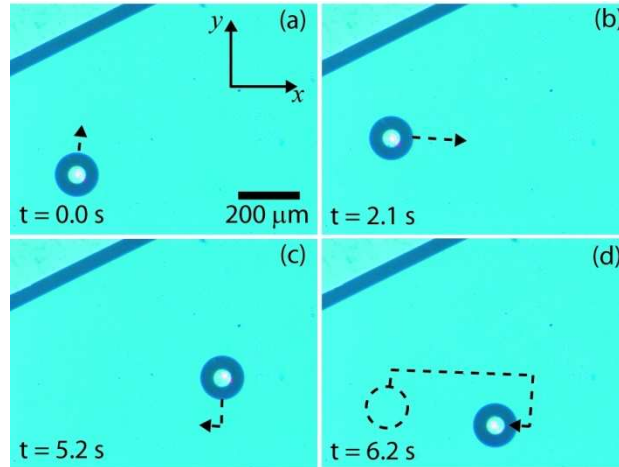


Figure 9.2 Optically-actuated thermocapillary movement of an air bubble in silicone oil [160]. A 114- μm -diameter (1.0 nL) bubble is trapped in the thermal trap created by a laser focused on the absorbing substrate (a). The oil/air meniscus can be seen at the top left. The bubble follows the position of the laser spot, as it is scanned in the positive y -direction (b) and then in the positive x -direction (c). The bubble is then moved in the negative y - and negative x -directions (d). The initial bubble position is indicated by a dashed circle, and the approximate trajectory of the bubble is indicated by a dashed line.

We have been able to reproducibly transport air bubbles with diameters ranging from 33 to 329 μm , which correspond to a volume range of 19 pL to 23 nL. (A spherical volume is assumed for bubbles with diameters smaller than the chamber height of 100 μm ; for larger bubbles, the cylindrical volume formula is used.) The maximum velocity at which these bubbles can be transported is linearly dependent on the intensity of the laser source (Figure 9.3) [160]. This is expected, as the laser intensity is directly proportional to induced thermal gradient produced by the optical absorption. The measured velocities are the maximum translation rates of the bubbles across the surface of the absorbing substrate, as the optical pattern is fixed and the substrate is moved by a motorized stage. The maximum translation rate of the motorized stage is 1 mm/s, limiting the maximum velocity that can be measured with this method. Bubbles with diameters of approximately

100 μm or less (volumes of 0.5 nL or less) easily exceed the maximum velocity of 1 mm/s, especially at the higher laser intensities. However, analysis of video captured during the bubble transport allows us to approximate the maximum velocity of bubbles less than 0.5 nL in volume to be approximately 1.5 mm/s at the lowest measured light intensity, 2 kW/cm^2 .

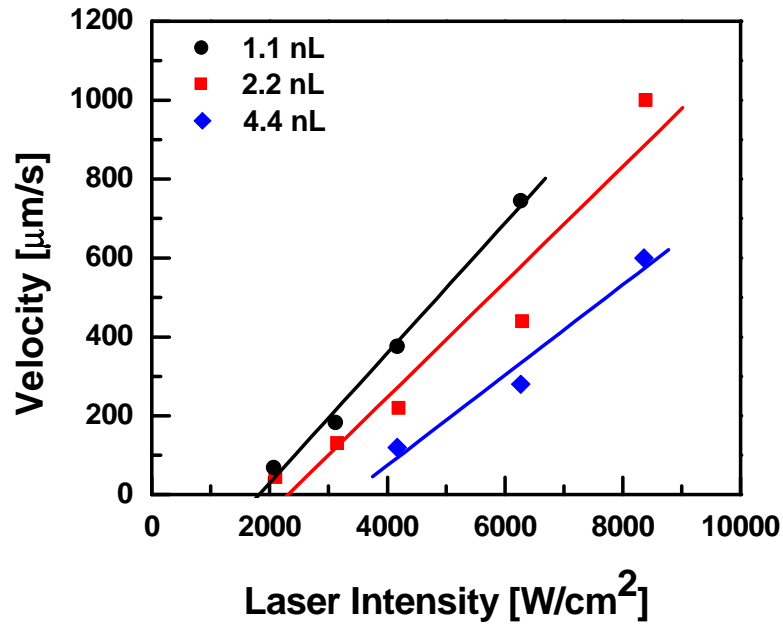


Figure 9.3 Optically-actuated thermocapillary movement-induced velocities of air bubbles as a function of laser intensity. The solid lines are linear fits to the data points.

The optically-induced temperature gradient can be determined using the temperature-dependent surface tension equation (Equation 9.1) and the Navier-Stokes equation. The calculated temperature gradient required to move a bubble at 1.5 mm/s is approximately 4000 K/m, given the viscosity of the silicone oil [161], $\mu = 4.56 \times 10^{-3}$ Pa·s, and the temperature coefficient of the surface tension [19, 50], $\gamma_T = -\partial\sigma/\partial T = 7.2 \times 10^{-5}$

$\text{N}\cdot\text{m}^{-1}\cdot\text{K}^{-1}$. In the geometry of the optically-actuated thermocapillary device, this corresponds to a temperature rise of approximately $0.5\text{ }^{\circ}\text{C}$ at the oil/a-Si:H interface. This value was verified experimentally using a $50\text{-}\mu\text{m}$ -thick thermocouple (Omega Engineering, type T; resolution = $0.1\text{ }^{\circ}\text{C}$) affixed to the a-Si:H substrate. The temperature measurements were taken with the fluidic system on an aluminum microscope stage, surrounded by a room temperature environment.

9.5 Discussion

Further possibilities of optically-actuated thermocapillary movement include the usage of spatial light modulators to simultaneously create multiple bubble traps, a technique that has widespread usage in the optical trapping community [142]. In addition, this technique is not limited to excitation by a coherent source; incoherent sources can be used, as long as a sufficient thermal gradient is generated.

Furthermore, the absorbing substrate used in these experiments has not been optimized for the generation of a thermal gradient, as it was originally designed for use as an electrode for OET. Thus, improvements may be made to the absorbing substrate to create higher thermal gradients. This may include alternate materials that have suitable optical absorption coefficients and low thermal conductivities. Optically-actuated thermocapillary bubble movement on an absorbing substrate enables the actuation of bubbles in a variety of liquids, independent of the optical properties of the liquid. This capability can be used in microfluidic applications as a way to optically control fluid pumping or switching [142]. The optical addressing of this technique is also amenable to the creation of dense arrays of optically-controlled bubbles.

Chapter 10 Conclusion

Optoelectronic tweezers has been demonstrated to be a flexible, powerful platform for micro- and nanoparticle manipulation. As OET utilizes optically-induced dielectrophoresis, it is more flexible and more easily reconfigured as compared to conventional dielectrophoresis. OET adds the control functionality of optical tweezers to dielectrophoresis; enabling parallel manipulation of *specific* single particles. However, as the underlying force mechanism is dielectrophoresis, optically-controlled manipulation is achieved using significantly lower optical intensities than optical tweezers, making OET manipulation much less harmful to live cells and optically-absorbing particles. In addition, OET is capable of trapping particles over a larger area than optical tweezers, resulting in improved parallel manipulation capabilities, especially for larger particles such as mammalian cells.

The usefulness of the OET device has been presented in the context of two main application fields: biology and engineering. In biology, OET can be used as a tool for single-cell studies, or to sort samples of cells. OET is capable of sorting between different

cell types, or between live and dead cells. We have used this capability to distinguish live viable non-motile sperm from dead sperm to aid in viable sperm selection for *in vitro* fertilization procedures. Furthermore, unlike traditional toxic chemical assays, OET manipulation introduces no detectable DNA fragmentation in the sorted sperm. Thus, OET sorting has the potential to increase the yield of intracytoplasmic sperm injection procedures, increasing efficacy while reducing cost. Medical costs associated with ICSI can exceed \$15,000 per procedure, with no guarantee of the outcome. Thus, improving ICSI would benefit more infertile couples by increasing the accessibility of this procedure.

A variant of the standard optoelectronic tweezers device, lateral-field optoelectronic tweezers, has been demonstrated. The LOET device is capable of manipulating anisotropic objects with their major axis parallel to the LOET substrate. This is useful for the assembly of anisotropic objects, such as nanowires, and for the heterogeneous integration of III-V material microdisk lasers on a silicon platform. This room-temperature, post-CMOS assembly technique provides an alternative to wafer-bonding processes, and is well-suited for the integration of a small number of optical sources with many CMOS devices, as in a transceiver chip. In addition, the parallel integration of multiple materials to achieve lasing at multiple wavelengths is possible using LOET assembly. This has the potential to facilitate the creation of silicon photonic devices, enabling optical communication from board-to-board, chip-to-chip, and even intrachip. The removal of the data bandwidth limitation presented by the current copper interconnects will transform the computer industry.

A variant of the LOET device is created with a blanket deposition of a-Si, with no subsequent electrode etching, to form a planar lateral-field optoelectronic tweezers device. This planar surface enables orientation control in the assembly of anisotropic objects such as nanowires. We are currently exploring the use of this device for the creation of a nanowire-based LED display. Other applications include the assembly of nanowires as interconnects or components in electronic devices. As this technique is capable of manipulating nanowires in parallel, it offers improved throughput over existing techniques such as placement using AFM tips.

The PLOET device is also self-contained on a single substrate, facilitating integration with other microelectromechanical systems, such as electrowetting-on-dielectric devices. Furthermore, the planar surface avoids pinning the meniscus of droplets on the surface of the device, unlike the standard LOET device. This made it possible to integrate the PLOET device with an EWOD device. The resulting platform is promising for cell purification and culturing. Cells of interest can be isolated from a larger population, and exposed to reagents contained in additional droplets. In this manner, single-cell behavior can be accurately studied and quantified, allowing biologists new insights into cellular behavior.

We have also demonstrated other useful effects in OET devices, such as optically-actuated thermocapillary forces using the OET substrate. This technique is capable of flexibly and dynamically controlling bubbles in microfluidic devices. Bubbles can be used to perform microfluidic-based logic operations, and can act as pumps and switches in microfluidic devices. This makes it possible to realize a true lab-on-a-chip device, with no external pumps required. Instead, optofluidic control will be used to pump and route

samples through the chip, greatly simplifying many current microfluidic setups, which can have a large number of fluidic connections and pumps.

The OET device enables many exciting experiments and applications, many more of which have yet to be discovered.

Appendix 1 Fabrication Process of Optoelectronic Tweezers

A1.1 UCLA Fabrication Process

Early OET devices, used in the experiments described in Chapter 1, were fabricated at the UCLA Nanoelectronics Research Facility (Nanolab) using commercially-available ITO-coated glass wafers (Delta Technologies, Ltd.). The fabrication process is outlined in Table A1.1 and Figure A1.1.

The fabrication process begins with a 1.1-mm-thick glass substrate, coated on one side with 100 nm of ITO. The substrate is diced into pieces measuring approximately 3.5 cm × 2.5 cm. The pieces are then cleaned in acetone, methanol, and isopropanol, rinsed with deionized (DI) water, and dried with a jet of nitrogen (N₂) gas (Step 1). The substrates are dried on a hotplate for 15 minutes at a temperature of 150°C (Step 2). An aluminum film is deposited onto the ITO-coated glass by an electron-beam (e-beam) evaporation process, using either the Sloan SL 1800 or the CHA Mark 40 e-beam evaporators (Step 3). The aluminum layer creates a more ohmic contact to the

amorphous silicon (a-Si) layer. To avoid the buildup of an oxide on the aluminum, intrinsic a-Si was deposited immediately following the aluminum deposition by plasma-enhanced chemical vapor deposition (PECVD) by the Plasmatherm 790 PECVD machine (Step 4). The a-Si layer has a thickness of 1 to 1.5 μm . Immediately after the a-Si deposition step, 20 nm of silicon nitride is deposited by PECVD, also in the Plasmatherm 790 (Step 5). The film quality of the a-Si layers fabricated in the Nanolab was relatively poor, making the silicon nitride essential as a passivation layer. If the nitride layer is not present, the a-Si film cracks and flakes off upon exposure to liquid. Low-tack tape is used to temporarily mask one edge of each piece (an area of approximately $2.5\text{ cm} \times 0.5\text{ cm}$), which will be used for electrical contact when applying ac bias to the device. Photoresist (AZ 5214E) is then spun over the device, using a spin speed of 2000 rpm for 30 seconds (Step 6). The low-tack tape is removed, exposing the area that will be etched. Reactive-ion etching (RIE) is used to etch through the nitride and a-Si layers, exposing the aluminum surface (Step 7). To perform this etch, the Technics Fluorine RIE 800 machine is used, with a 5:1 $\text{CF}_4:\text{O}_2$ gas ratio at a pressure of 200 mtorr. The RF power used to create the plasma is set at 150 W, allowing etch completion in approximately 6 minutes. The photoresist is removed using acetone, and the pieces are rinsed with isopropanol and DI water (Step 8). After drying the pieces with N_2 gas, the electrical contact pads are created with a silver conductive epoxy (Step 9).

Table A1.1 OET fabrication process overview (UCLA process)

Step	Process	Parameters
1	Clean substrate; N ₂ dry	Start with 1.1-mm-thick ITO-coated glass substrate
2	Dehydration bake	150°C for 15 min
3	Electron-beam evaporation of aluminum	10 nm film thickness Equipment: Sloan SL 1800 e-beam evaporator or CHA Mark 40 e-beam evaporator
4	Plasma-enhanced chemical vapor deposition (PECVD) of a-Si	1 to 1.5 μm film thickness Equipment: Plasmatherm 790 Recipe: a-Si2
5	PECVD deposition of silicon nitride	20 nm film thickness Equipment: Plasmatherm 790 Recipe: Initride
6	Spin on photoresist (AZ 5214E), leave electrical contact area unprotected	500 rpm spread for 5 s, 2000 rpm for 30 s Equipment: Headway spin coater
7	Reactive-ion etch (RIE) electrical contact area to aluminum layer	5:1 CF ₄ :O ₂ , 200 mtorr, 150 W for ~6 min. Equipment: Technics Fluorine RIE 800
8	Remove photoresist	Acetone clean
9	Electrical contact pads	Silver conductive epoxy (Epotek E2101) Recipe: 3:1 part A to part B, cure @ 150°C for 1 hr.

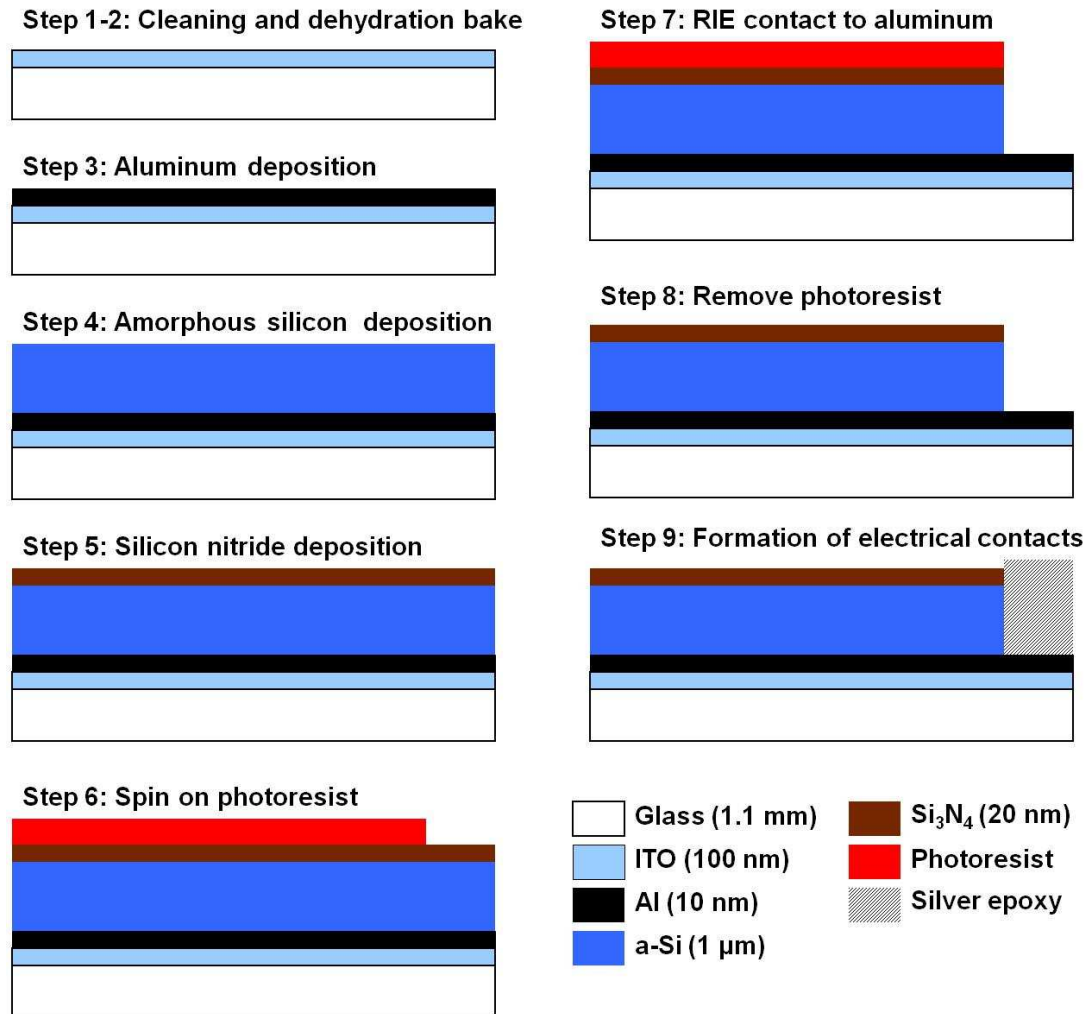


Figure A1.1 Fabrication process of OET devices fabricated at UCLA.

A1.2 Silicon Display Technologies Fabrication Process

A foundry service (Silicon Display Technology, Seoul, Korea) was used to fabricate the OET devices used in the experiments of Chapter 1, 3, 5, and 9. These devices utilized a slightly different device structure, as the a-Si could now be doped. In addition, hydrogen could be incorporated into the a-Si to reduce the number of defect states, resulting in hydrogenated amorphous silicon (a-Si:H). The fabrication process for the alternate variation of the OET device is shown below in Table A1.2 and Figure A1.2. All

steps are performed in the UCLA Nanolab or UC Berkeley Microfabrication Laboratory (Microlab), although the starting device layers are fabricated by Silicon Display Technology.

Table A1.2 Alternate fabrication process overview

Step	Process	Parameters
1	Clean substrate; N ₂ dry	Start with 0.85-mm-thick ITO-coated glass substrate, with 50 nm n+ a-Si:H / 1 μm a-Si:H
2	Dehydration bake	150°C for 15 min
3	Spin on photoresist (AZ 5214E), leave electrical contact area unprotected	500 rpm spread for 5 s, 2000 rpm for 30 s Equipment: Headway spin coater
4	RIE electrical contact area to ITO layer	5:1 CF ₄ :O ₂ , 100 mtorr, 150 W for ~6 min. Equipment: Technics Fluorine RIE 800 9:1 SF ₆ :O ₂ , 100 mtorr, 100 W for ~2 min. Equipment: Plasmatherm PK-12 RIE
5	Remove photoresist	Acetone clean
6	Electrical contact pads	Silver conductive epoxy (Epotek E2101) Recipe: 3:1 part A to part B, cure @ 150°C for 1 hr.

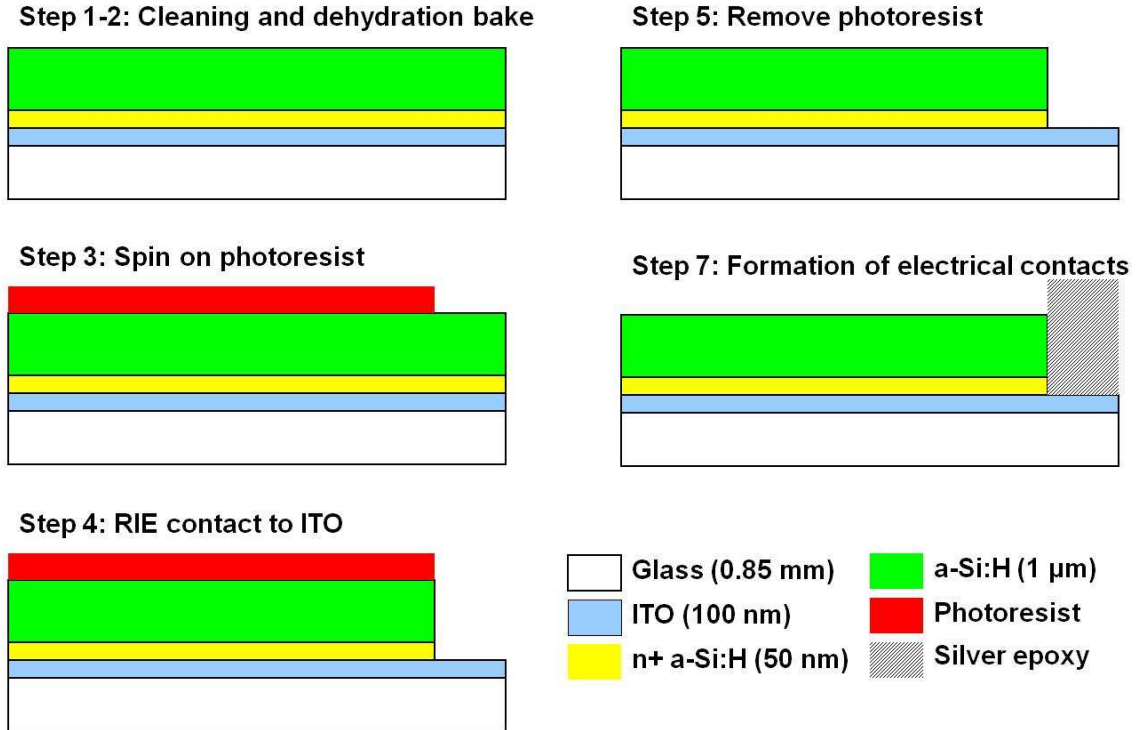


Figure A1.2 Fabrication process of OET devices with ITO and a-Si:H layers deposited by Silicon Display Technology.

The fabrication process for the devices from Silicon Display Technology begins with the shipped glass wafers, which consist of a 0.85-mm-thick glass substrate, coated on one side with 100 nm of ITO, 50 nm of n+ doped a-Si:H, and 1 μm of intrinsic a-Si:H. The n+ doped a-Si:H layer provides an ohmic contact between the ITO and the intrinsic a-Si:H. The wafers are diced, cleaned, and dried (Step 1), followed by a dehydration bake (Step 2). The deposited a-Si:H layers of these devices are of much higher quality than those produced in UCLA's Nanolab. Even upon repeated exposure to liquid, the a-Si:H layers are not damaged. Thus, passivating the silicon surface with a nitride layer is not required for these devices. As in the previous fabrication process, photoresist (AZ 5214E) is then spun over the device, leaving the area to be used for electrical contact exposed (Step 3).

An RIE step is performed to gain access to the ITO layer (Step 4). The photoresist is stripped (Step 5), and the electrical contact pads are created (Step 6).

A1.3 UC Berkeley Fabrication Process

The fabrication of all types of OET devices can also be done entirely in UC Berkeley's Microlab. The quality of the a-Si films deposited in the Microlab are of a quality similar to the films from Silicon Display Technology, although hydrogenation and doping are currently unavailable. The fabrication process is shown in Table A1.3 and Figure A1.3.

Table A1.3 OET fabrication process overview (UC Berkeley process)

Step	Process	Parameters
1	Clean substrate; N ₂ dry	Start with 1.1-mm-thick ITO-coated glass substrate
2	Dehydration bake	150°C for 15 min
3	Plasma-enhanced chemical vapor deposition (PECVD) of a-Si	0.75 to 1.5 μm film thickness Equipment: Oxford Plasmalab 80plus PECVD Recipe: 400 sccm Ar, 100 sccm 10% SiH ₄ / Ar 900 mtorr, 350°C, 10 to 300 W RF power
4	Spin on photoresist, leave electrical contact area unprotected	500 rpm spread for 5 s, 2000 rpm for 30 s Equipment: Headway spin coater
5	Reactive-ion etch (RIE) electrical contact area to ITO layer	9:1 SF ₆ :O ₂ , 100 mtorr, 100 W for ~2 min. Equipment: Plasmatherm PK-12 RIE
6	Remove photoresist	Acetone clean
7	Electrical contact pads	Silver conductive epoxy (Epotek E2101) Recipe: 3:1 part A to part B, cure @ 150°C for 1 hr.

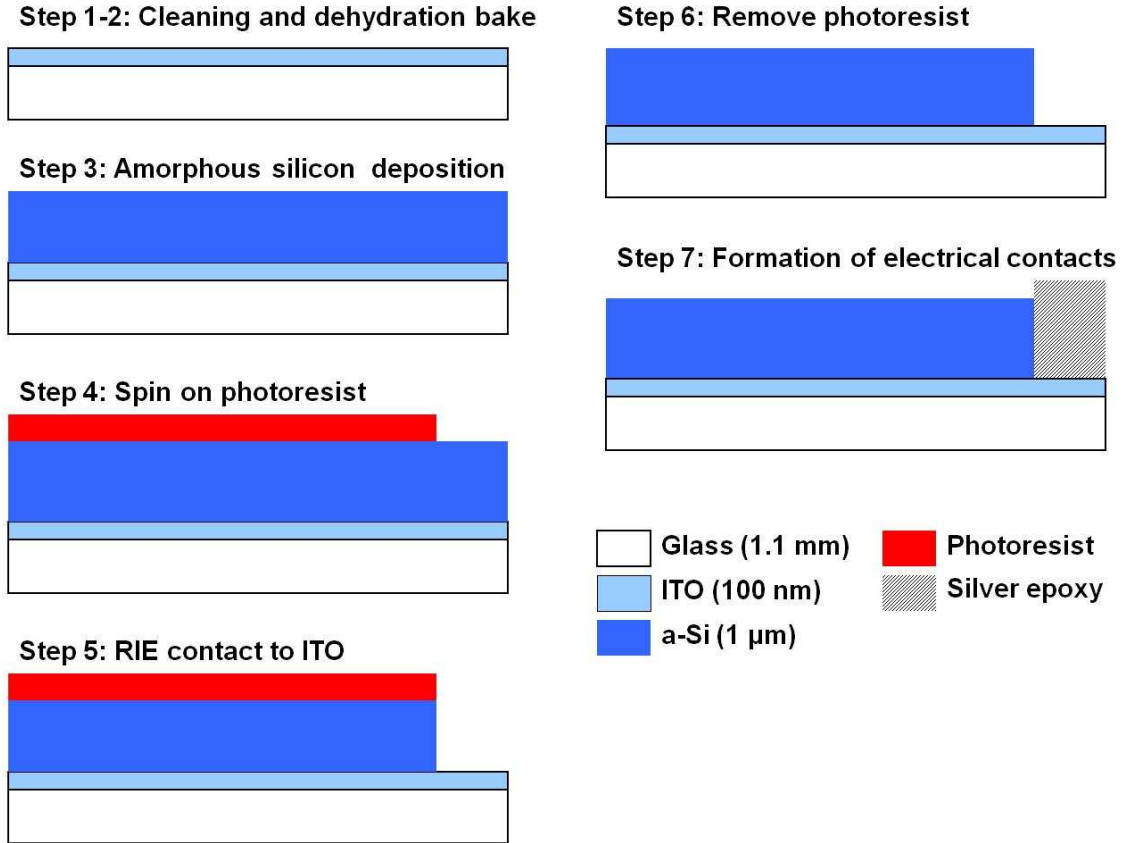


Figure A1.3 Fabrication process of OET devices fabricated at UC Berkeley.

Like the UCLA process, fabrication begins with a 1.1-mm-thick glass substrate, coated on one side with 100 nm of ITO. Steps 1 and 2 are identical to the UCLA process. However, the aluminum layer is eliminated, as its absence does not affect the OET device performance. Undoped a-Si is deposited directly on the ITO layer using PECVD. Steps 4 to 7 describe the creation of the electrical contact pads, which is the same as in the other fabrication processes.

Appendix 2 PEG Coating Process

A2.1 PEG Coating on a-Si Electrodes

The PEG coating process begins with an a-Si OET electrode, just before the electrical contact pads are created with silver conductive epoxy. (The fabrication of the a-Si electrodes is described in Appendix 1.) The complete PEG coating process is outlined in Table A2.1.

Table A2.1 PEG coating process on a-Si electrodes

Step	Process	Parameters
1	Deposit 10-nm-thick SiO ₂ on a-Si	Equipment: Oxford Plasmalab 80plus PECVD
2	Rinse	Rinse with ethanol, dry with N ₂
3	Bake	110°C for 30 min. in convection oven
4	Electrical contact pads	Silver conductive epoxy (Epotek E2101) Recipe: 3:1 part A to part B, cure @ 150°C for 1 hr.
5	Chemical wash	1:1:4 volume ratio of 29% NH ₄ OH, 30% H ₂ O ₂ , DI water for 90 min. Rinse with DI water
6	Chemical wash	1:1:4 volume ratio of 38% HCl, 30% H ₂ O ₂ , DI water for 90 min. Rinse with DI water, dry with N ₂
7	Bake	110°C for 30 min. in convection oven
8	PEG coating	Place ~10 mg of PEG-silane on OET chip 65°C for 24 hours on hotplate
9	Rinse	DI water, dry with N ₂
10	Anneal	110°C for 10 min. in convection oven

First, a 10-nm-thick SiO₂ layer is deposited over the a-Si layer using PECVD. The a-Si electrodes are then rinsed, and baked in a convection oven. Following this, the electrical bias pads are created using silver epoxy. The a-Si chips then undergo a series of chemical washes to silanize the surface, enhancing PEG attachment. First, the devices are bathed in a 1:1:4 volume ratio of 29% NH₄OH, 30% H₂O₂, and DI water for 90 min, then rinsed with DI water. This is followed by another bath in a 1:1:4 volume ratio of 38% HCl, 30% H₂O₂, and DI water for 90 min. The chips are again rinsed with DI water, dried, and baked to remove all moisture. A solid PEG-silane of 2-[methoxy(polyethyleneoxy)propyl]trimethoxysilane (Nektar) is placed on the surface of the a-Si electrodes, and melted using a hotplate at 65°C for 24 hours. The PEG-coated chips are then rinsed and annealed at 110°C in a convection oven.

A2.2 PEG Coating on ITO-coated Electrodes

The PEG coating process begins with an ITO OET electrode. (The fabrication of the ITO electrodes is described in Chapter 2.7.) The complete PEG coating process is outlined in Table A2.2.

Table A2.2 PEG coating process on ITO electrodes

Step	Process	Parameters
1	Rinse	DI water, methanol, acetone, methanol, DI water, dry with N ₂
2	Bake	110°C for 10 min. in convection oven
3	Chemical wash	1:1:4 volume ratio of 29% NH ₄ OH, 30% H ₂ O ₂ , DI water for 90 min. Rinse with DI water, dry with N ₂
4	Bake	110°C for 10 min. in convection oven
8	PEG coating	Place ~10 mg of PEG-silane on OET chip 65°C for 24 hours on hotplate
9	Rinse	DI water, N ₂ dry
10	Anneal	110°C for 10 min. in convection oven

First, the ITO electrodes are rinsed, and baked in a convection oven. The ITO chips then undergo a chemical wash to silanize the surface, enhancing PEG attachment. The devices are bathed in a 1:1:4 volume ratio of 29% NH₄OH, 30% H₂O₂, and DI water for 90 min. Next, they are rinsed with DI water, dried with nitrogen, then baked to remove all moisture. The solid PEG-silane is placed on the surface of the ITO electrodes, and melted using a hotplate at 65°C for 24 hours. The PEG-coated chips are then rinsed and annealed at 110°C in a convection oven.

BIBLIOGRAPHY

- [1] C. J. Kim, A. P. Pisano, and R. S. Muller, "Silicon-Processed Overhanging Microgripper," *IEEE Journal of Microelectromechanical Systems*, vol. 1, pp. 31-36, 1992.
- [2] C. G. Keller and R. T. Howe, "Hexsil tweezers for teleoperated micro-assembly," in *Tenth Annual IEEE International Workshop on Micro Electro Mechanical Systems (MEMS)*, 1997, pp. 72-77.
- [3] N. Chronis and L. P. Lee, "Electrothermally activated SU-8 microgripper for single cell manipulation in solution," *IEEE Journal of Microelectromechanical Systems*, vol. 14, pp. 857-863, 2005.
- [4] P. Avouris, T. Hertel, R. Martel, T. Schmidt, H. R. Shea, et al., "Carbon nanotubes: nanomechanics, manipulation, and electronic devices," *Applied Surface Science*, vol. 141, pp. 201-209, 1999.
- [5] C. Thelander and L. Samuelson, "AFM manipulation of carbon nanotubes: realization of ultra-fine nanoelectrodes," *Nanotechnology*, vol. 13, pp. 108-113, 2002.
- [6] A. K. Bentley, J. S. Trethewey, A. B. Ellis, and W. C. Crone, "Magnetic manipulation of copper-tin nanowires capped with nickel ends," *Nano Letters*, vol. 4, pp. 487-490, 2004.
- [7] K. H. Han and A. B. Frazier, "Continuous magnetophoretic separation of blood cells in microdevice format," *Journal of Applied Physics*, vol. 96, pp. 5797-5802, 2004.
- [8] D. W. Inglis, R. Riehn, R. H. Austin, and J. C. Sturm, "Continuous microfluidic immunomagnetic cell separation," *Applied Physics Letters*, vol. 85, pp. 5093-5095, 2004.
- [9] H. Lee, A. M. Purdon, and R. M. Westervelt, "Manipulation of biological cells using a microelectromagnet matrix," *Applied Physics Letters*, vol. 85, pp. 1063-1065, 2004.
- [10] C. Q. Yi, C. W. Li, S. L. Ji, and M. S. Yang, "Microfluidics technology for manipulation and analysis of biological cells," *Analytica Chimica Acta*, vol. 560, pp. 1-23, 2006.
- [11] A. R. Wheeler, W. R. Throdset, R. J. Whelan, A. M. Leach, R. N. Zare, et al., "Microfluidic device for single-cell analysis," *Analytical Chemistry*, vol. 75, pp. 3581-3586, 2003.

- [12] D. Di Carlo, L. Y. Wu, and L. P. Lee, "Dynamic single cell culture array," *Lab on a Chip*, vol. 6, pp. 1445-1449, 2006.
- [13] A. Y. Fu, H. P. Chou, C. Spence, F. H. Arnold, and S. R. Quake, "An integrated microfabricated cell sorter," *Analytical Chemistry*, vol. 74, pp. 2451-2457, 2002.
- [14] A. Wolff, I. R. Perch-Nielsen, U. D. Larsen, P. Friis, G. Goranovic, et al., "Integrating advanced functionality in a microfabricated high-throughput fluorescent-activated cell sorter," *Lab on a Chip*, vol. 3, pp. 22-27, 2003.
- [15] J. T. Keane, D. Ryan, and P. P. Gray, "Effect of shear stress on expression of a recombinant protein by Chinese hamster ovary cells," *Biotechnology and Bioengineering*, vol. 81, pp. 211-220, 2003.
- [16] A. Ashkin, "Acceleration and trapping of particles by radiation pressure," *Physical Review Letters*, vol. 24, pp. 156-9, 1970.
- [17] A. Ashkin, J. M. Dziedzic, J. E. Bjorkholm, and S. Chu, "Observation of a single-beam gradient force optical trap for dielectric particles," *Optics Letters*, vol. 11, pp. 288-90, 1986.
- [18] E. R. Dufresne and D. G. Grier, "Optical tweezer arrays and optical substrates created with diffractive optics," *Review of Scientific Instruments*, vol. 69, pp. 1974-7, 1998.
- [19] D. G. Grier, "A revolution in optical manipulation," *Nature*, vol. 424, pp. 810-816, 2003.
- [20] B. Maier, M. Koomey, and M. P. Sheetz, "A force-dependent switch reverses type IV pilus retraction," *Proceedings Of The National Academy Of Sciences Of The United States Of America*, vol. 101, pp. 10961-10966, 2004.
- [21] M. P. MacDonald, G. C. Spalding, and K. Dholakia, "Microfluidic sorting in an optical lattice," *Nature*, vol. 426, pp. 421-4, 2003.
- [22] L. Paterson, E. Papagiakoumou, G. Milne, V. Garces-Chavez, S. A. Tatarkova, et al., "Light-induced cell separation in a tailored optical landscape," *Applied Physics Letters*, vol. 87, 2005.
- [23] R. Agarwal, K. Ladavac, Y. Roichman, G. H. Yu, C. M. Lieber, et al., "Manipulation and assembly of nanowires with holographic optical traps," *Optics Express*, vol. 13, pp. 8906-8912, 2005.
- [24] P. J. Pauzauskie, A. Radenovic, E. Trepagnier, H. Shroff, P. Yang, et al., "Optical trapping and integration of semiconductor nanowire assemblies in water," *Nat Mater*, vol. 5, pp. 97-101, 2006.

- [25] K. C. Neuman, E. H. Chadd, G. F. Liou, K. Bergman, and S. M. Block, "Characterization of photodamage to *Escherichia coli* in optical traps," *Biophysical Journal*, vol. 77, pp. 2856-2863, 1999.
- [26] A. Ashkin, J. M. Dziedzic, and T. Yamane, "Optical trapping and manipulation of single cells using infrared laser beams," *Nature*, vol. 330, pp. 769-771, 1987.
- [27] S. K. Mohanty, A. Rapp, S. Monajembashi, P. K. Gupta, and K. O. Greulich, "Comet assay measurements of DNA damage in cells by laser microbeams and trapping beams with wavelengths spanning a range of 308 nm to 1064 nm," *Radiation Research*, vol. 157, pp. 378-385, 2002.
- [28] K. Konig, H. Liang, M. W. Berns, and B. J. Tromberg, "Cell damage in near-infrared multimode optical traps as a result of multiphoton absorption," *Optics Letters*, vol. 21, pp. 1090-1092, 1996.
- [29] M. Gu, J. B. Haumonte, Y. Micheau, J. W. M. Chon, and X. S. Gan, "Laser trapping and manipulation under focused evanescent wave illumination," *Applied Physics Letters*, vol. 84, pp. 4236-4238, 2004.
- [30] V. Garces-Chavez, K. Dholakia, and G. C. Spalding, "Extended-area optically induced organization of microparticles on a surface," *Applied Physics Letters*, vol. 86, 2005.
- [31] X. Miao and L. Y. Lin, "Trapping and manipulation of biological particles through a plasmonic platform," *IEEE Journal of Selected Topics in Quantum Electronics*, vol. 13, pp. 1655-1662, 2007.
- [32] A. N. Grigorenko, N. W. Roberts, M. R. Dickinson, and Y. Zhang, "Nanometric optical tweezers based on nanostructured substrates," *Nature Photonics*, vol. 2, pp. 365-370, 2008.
- [33] H. A. Pohl, "Some Effects of Nonuniform Fields on Dielectrics," *Journal of Applied Physics*, vol. 29, pp. 1182-1188, 1958.
- [34] R. Pethig, M. S. Talary, and R. S. Lee, "Enhancing traveling-wave dielectrophoresis with signal superposition," *IEEE Engineering In Medicine And Biology Magazine*, vol. 22, pp. 43-50, 2003.
- [35] P. R. C. Gascoyne and J. V. Vykoukal, "Dielectrophoresis-based sample handling in general-purpose programmable diagnostic instruments," *Proceedings Of The IEEE*, vol. 92, pp. 22-42, 2004.
- [36] J. Voldman, "Electrical forces for microscale cell manipulation," *Annual Review of Biomedical Engineering*, vol. 8, pp. 425-454, 2006.

- [37] P. R. C. Gascoyne, X.-B. Wang, Y. Huang, and F. F. Becker, "Dielectrophoretic separation of cancer cells from blood," *IEEE Transactions on Industry Applications*, vol. 33, pp. 670-8, 1997.
- [38] J. Cheng, E. L. Sheldon, L. Wu, M. J. Heller, and J. P. O'Connell, "Isolation of cultured cervical carcinoma cells mixed with peripheral blood cells on a bioelectronic chip," *Analytical Chemistry*, vol. 70, pp. 2321-2326, 1998.
- [39] Y. Huang, J. Yang, X. B. Wang, F. F. Becker, and P. R. C. Gascoyne, "The removal of human breast cancer cells from hematopoietic CD34(+) stem cells by dielectrophoretic field-flow-fractionation," *Journal of Hematotherapy & Stem Cell Research*, vol. 8, pp. 481-490, 1999.
- [40] Y. Huang, J. M. Yang, P. J. Hopkins, S. Kassegne, M. Tirado, et al., "Separation of simulants of biological warfare agents from blood by a miniaturized dielectrophoresis device," *Biomedical Microdevices*, vol. 5, pp. 217-225, 2003.
- [41] R. Krupke, F. Hennrich, H. v Lohneysen, and M. M. Kappes, "Separation of metallic from semiconducting single-walled carbon nanotubes," *Science*, vol. 301, pp. 344-7, 2003.
- [42] S. Evoy, N. DiLello, V. Deshpande, A. Narayanan, H. Liu, et al., "Dielectrophoretic assembly and integration of nanowire devices with functional CMOS operating circuitry," *Microelectronic Engineering*, vol. 75, pp. 31-42, 2004.
- [43] S. Evoy, M. A. Riegelman, N. Naguib, H. H. Ye, P. Jaroenapibal, et al., "Dielectrophoretic assembly of carbon nanofiber nanoelectromechanical devices," *IEEE Transactions On Nanotechnology*, vol. 4, pp. 570-575, 2005.
- [44] N. Manaresi, A. Romani, G. Medoro, L. Altomare, A. Leonardi, et al., "A CMOS chip for individual cell manipulation and detection," *IEEE Journal of Solid-State Circuits*, vol. 38, pp. 2297-305, 2003.
- [45] A. B. Fuchs, A. Romani, D. Freida, G. Medoro, M. Abonnenc, et al., "Electronic sorting and recovery of single live cells from microlitre sized samples," *Lab on a Chip*, vol. 6, pp. 121-126, 2006.
- [46] C. R. Cabrera and P. Yager, "Continuous concentration of bacteria in a microfluidic flow cell using electrokinetic techniques," *Electrophoresis*, vol. 22, pp. 355-362, 2001.
- [47] A. Y. Fu, C. Spence, A. Scherer, F. H. Arnold, and S. R. Quake, "A microfabricated fluorescence-activated cell sorter," *Nature Biotechnology*, vol. 17, pp. 1109-1111, 1999.

- [48] R. C. Hayward, D. A. Saville, and I. A. Aksay, "Electrophoretic assembly of colloidal crystals with optically tunable micropatterns," *Nature*, vol. 404, pp. 56-59, 2000.
- [49] P. Y. Chiou, Z. Chang, and M. C. Wu, "A Novel Optoelectronic Tweezer Using Light Induced Dielectrophoresis," in *IEEE/LEOS International Conference on Optical MEMS*, Kona, Hawaii, USA, 2003, pp. 8-9.
- [50] P. Y. Chiou, A. T. Ohta, and M. C. Wu, "Massively parallel manipulation of single cells and microparticles using optical images," *Nature*, vol. 436, pp. 370-372, 2005.
- [51] A. T. Ohta, P. Y. Chiou, T. H. Han, J. C. Liao, U. Bhardwaj, et al., "Dynamic Cell and Microparticle Control via Optoelectronic Tweezers," *Journal of Microelectromechanical Systems*, vol. 16, pp. 491-499, 2007.
- [52] A. T. Ohta, P.-Y. Chiou, H. L. Phan, S. W. Sherwood, J. M. Yang, et al., "Optically Controlled Cell Discrimination and Trapping Using Optoelectronic Tweezers," *IEEE Journal of Selected Topics in Quantum Electronics*, vol. 13, pp. 235-243, 2007.
- [53] Y.-S. Lu, Y.-P. Huang, J. A. Yeh, C. Lee, and Y.-H. Chang, "Controllability of non-contact cell manipulation by image dielectrophoresis (iDEP)," *Optical and Quantum Electronics*, vol. 37, pp. 1385-95, 2005.
- [54] S. L. Neale, M. Mazilu, J. I. B. Wilson, K. Dholakia, and T. F. Krauss, "The resolution of optical traps created by light induced dielectrophoresis (LIDEP)," *Optics Express*, vol. 15, pp. 12619-12626, 2007.
- [55] W. Choi, S. H. Kim, J. Jang, and J. K. Park, "Lab-on-a-display: a new microparticle manipulation platform using a liquid crystal display (LCD)," *Microfluidics and Nanofluidics*, vol. 3, pp. 217-225, 2007.
- [56] H. Hwang, Y. J. Choi, W. Choi, S. H. Kim, J. Jang, et al., "Interactive manipulation of blood cells using a lens-integrated liquid crystal display based optoelectronic tweezers system," *Electrophoresis*, vol. 29, pp. 1203-1212, 2008.
- [57] M.-C. Tien, A. T. Ohta, K. Yu, L. C. Chuang, A. Jamshidi, et al., "Hybrid Microdisk Laser on a Silicon Platform Using Lateral-Field Optoelectronic Tweezers Assembly," in *Conference on Lasers and Electro-Optics (CLEO)* San Jose, CA, 2008.
- [58] P. Y. Chiou, W. Wong, J. C. Liao, and M. C. Wu, "Cell Addressing and Trapping Using Novel Optoelectronic Tweezers," in *17th IEEE International Conference on Micro Electro Mechanical Systems (MEMS)*, Maastricht, Netherlands, 2004, pp. 21-24.

- [59] H. Y. Hsu, A. T. Ohta, P. Y. Chiou, A. Jamshidi, and M. C. Wu, "Phototransistor-based optoelectronic tweezers for cell manipulation in highly conductive solution," in *Transducers '07 & Eurosensors XXI: 14th International Conference on Solid-State Sensors, Actuators and Microsystems*, Lyon, France, 2007, pp. 477-480.
- [60] A. Jamshidi, P. J. Pauzauskie, P. J. Schuck, A. T. Ohta, P. Y. Chiou, et al., "Dynamic manipulation and separation of individual semiconducting and metallic nanowires," *Nature Photonics*, vol. 2, pp. 85-89, 2008.
- [61] A. T. Ohta, A. Jamshidi, P. J. Pauzauskie, H.-Y. Hsu, P. Yang, et al., "Trapping and transport of silicon nanowires using lateral-field optoelectronic tweezers," in *Conference on Lasers and Electro-Optics (CLEO)*, Baltimore, MD, 2007, pp. 828-829.
- [62] A. T. Ohta, S. L. Neale, H. Y. Hsu, J. K. Valley, and M. C. Wu, "Parallel Assembly of Nanowires Using Lateral-Field Optoelectronic Tweezers," in *International Conference on Optical MEMS & Nanophotonics*, Freiburg, Germany, 2008, pp. 7-8.
- [63] H. Hwang, Y. Oh, J. J. Kim, W. Choi, J. K. Park, et al., "Reduction of nonspecific surface-particle interactions in optoelectronic tweezers," *Applied Physics Letters*, vol. 92, p. 3, 2008.
- [64] G. J. Shah, P. Y. Chiou, J. Gong, A. T. Ohta, J. B. Chou, et al., "Integrating Optoelectronic Tweezers for Individual Particle Manipulation with Digital Microfluidics Using Electrowetting-On-Dielectric (EWOD)," in *19th IEEE International Conference on Micro Electro Mechanical Systems (MEMS)*, Istanbul, Turkey, 2006, pp. 130-133.
- [65] S. Park, C. Pan, T.-H. Wu, C. Kloss, S. Kalim, et al., "Floating electrode optoelectronic tweezers: light-driven dielectrophoretic droplet manipulation in electrically insulating oil medium," *Applied Physics Letters*, vol. 92, pp. 151101-1-3, 2008.
- [66] P. Y. Chiou, A. T. Ohta, and M. C. Wu, "Continuous Optical Sorting of HeLa Cells and Microparticles Using Optoelectronic Tweezers," in *IEEE/LEOS International Conference on Optical MEMS and Their Applications*, Oulu, Finland, 2005, pp. 83-84.
- [67] B. Fry and C. Reas, Processing.org: Open source programming language, website address: <http://processing.org/>.
- [68] R. Schwarz, F. Wang, and M. Reissner, "Fermi level dependence of the ambipolar diffusion length in silicon thin film transistors," *Applied Physics Letters*, vol. 63, pp. 1083-5, 1993.

- [69] T. B. Jones, *Electromechanics of Particles*. Cambridge: Cambridge University Press, 1995.
- [70] P. R. C. Gascoyne, F. F. Becker, and X. B. Wang, "Numerical-analysis of the influence of experimental conditions on the accuracy of dielectric parameters derived from electrorotation measurements," *Bioelectrochemistry and Bioenergetics*, vol. 36, pp. 115-125, 1995.
- [71] J. Gimsa and D. Wachner, "A unified resistor-capacitor model for impedance, dielectrophoresis, electrorotation, and induced transmembrane potential," *Biophysical Journal*, vol. 75, pp. 1107-1116, 1998.
- [72] J. Yang, Y. Huang, X. J. Wang, X. B. Wang, F. F. Becker, et al., "Dielectric properties of human leukocyte subpopulations determined by electrorotation as a cell separation criterion," *Biophysical Journal*, vol. 76, pp. 3307-3314, 1999.
- [73] V. Raicu, G. Raicu, and G. Turcu, "Dielectric properties of yeast cells as simulated by the two-shell model," *Biochimica Et Biophysica Acta-Bioenergetics*, vol. 1274, pp. 143-148, 1996.
- [74] M. C. Lopez, F. J. Iglesias, C. Santamaria, and A. Dominguez, "Dielectrophoretic behavior of yeast cells - Effect of growth sources and cell-wall and a comparison with fungal spores," *Journal of Bacteriology*, vol. 162, pp. 790-793, 1985.
- [75] S. Adachi, *Optical properties of crystalline and amorphous semiconductors: materials and fundamental principles*. Boston: Kluwer Academic Publishers, 1999.
- [76] Y. Higuchi, T. Kusakabe, T. Tanemura, K. Sugano, T. Tsuchiya, et al., "Manipulation system for nano/micro components integration via transportation and self-assembly," in *2008 21st IEEE International Conference on Micro Electro Mechanical Systems*, Tucson, AZ, 2008.
- [77] J. K. Valley, A. Jamshidi, A. T. Ohta, H.-Y. Hsu, and M. C. Wu, "Operational regimes and physics present in optoelectronic tweezers," *Journal of Microelectromechanical Systems*, vol. 17, pp. 342-50, 2008.
- [78] P. Y. Chiou, A. T. Ohta, A. Jamshidi, H. Y. Hsu, and M. C. Wu, "Light-actuated ac electroosmosis for nanoparticle manipulation," *Journal of Microelectromechanical Systems*, vol. 17, pp. 525-531, 2008.
- [79] J. Lyklema, *Fundamentals of Interface and Colloid Science* vol. 2. London, U.K.: Academic, 1991.
- [80] R. B. M. Schasfoort, S. Schlautmann, L. Hendrikse, and A. van den Berg, "Field-effect flow control for microfabricated fluidic networks," *Science*, vol. 286, pp. 942-945, 1999.

- [81] H. Daiguji, P. D. Yang, and A. Majumdar, "Ion transport in nanofluidic channels," *Nano Letters*, vol. 4, pp. 137-142, 2004.
- [82] J. P. Urbanski, T. Thorsen, J. A. Levitan, and M. Z. Bazant, "Fast AC electro-osmotic micropumps with nonplanar electrodes," *Applied Physics Letters*, vol. 89, p. 3, 2006.
- [83] P. Kingshott and H. J. Griesser, "Surfaces that resist bioadhesion," *Current Opinion In Solid State & Materials Science*, vol. 4, pp. 403-412, 1999.
- [84] I. Szleifer, "Protein adsorption on surfaces with grafted polymers: A theoretical approach," *Biophysical Journal*, vol. 72, pp. 595-612, 1997.
- [85] R. L. C. Wang, H. J. Kreuzer, and M. Grunze, "Molecular conformation and solvation of oligo(ethylene glycol)-terminated self-assembled monolayers and their resistance to protein adsorption," *Journal of Physical Chemistry B*, vol. 101, pp. 9767-9773, 1997.
- [86] S. J. Sofia, V. Premnath, and E. W. Merrill, "Poly(ethylene oxide) grafted to silicon surfaces: Grafting density and protein adsorption," *Macromolecules*, vol. 31, pp. 5059-5070, 1998.
- [87] R. M. Schultz and C. J. Williams, "The science of ART," *Science*, vol. 296, pp. 2188-2190, 2002.
- [88] U.S. Department of Health and Human Services: Centers for Disease Control and Prevention, 2005 Assisted Reproductive Technology Success Rates, website address: <http://www.cdc.gov/ART/>.
- [89] D. J. Lamb and L. I. Lipshultz, "Male infertility: recent advances and a look towards the future," *Current Opinion in Urology*, vol. 10, pp. 359-362, 2000.
- [90] S. Oehninger, "Clinical and laboratory management of male infertility: An opinion on its current status," *Journal of Andrology*, vol. 21, pp. 814-821, 2000.
- [91] G. Palermo, H. Joris, P. Devroey, and A. C. Vansteirteghem, "Pregnancies after intracytoplasmic injection of single spermatozoon into an oocyte," *Lancet*, vol. 340, pp. 17-18, 1992.
- [92] B. S. Cho, T. G. Schuster, X. Y. Zhu, D. Chang, G. D. Smith, et al., "Passively driven integrated microfluidic system for separation of motile sperm," *Analytical Chemistry*, vol. 75, pp. 1671-1675, 2003.
- [93] T. G. Schuster, B. Cho, L. M. Keller, S. Takayama, and G. D. Smith, "Isolation of motile spermatozoa from semen samples using microfluidics," *Reproductive Biomedicine Online*, vol. 7, pp. 75-81, 2003.

- [94] R. F. Casper, L. Cowan, J. S. Meriano, M. L. Lucato, and K. A. Jarvi, "The hypo-osmotic swelling test for selection of viable sperm for intracytoplasmic sperm injection in men with complete asthenozoospermia," *Fertility and Sterility*, vol. 65, pp. 972-976, 1996.
- [95] W. M. Buckett, "Predictive value of hypo-osmotic swelling test to identify viable non-motile sperm," *Asian Journal of Andrology*, vol. 5, pp. 209-212, 2003.
- [96] L. Bjorndahl, I. Soderlund, and U. Kvist, "Evaluation of the one-step eosin-nigrosin staining technique for human sperm vitality assessment," *Human Reproduction*, vol. 18, pp. 813-816, 2003.
- [97] C. B. Smikle and P. J. Turek, "Hypo-osmotic swelling can accurately assess the viability of nonmotile sperm," *Molecular Reproduction and Development*, vol. 47, pp. 200-203, 1997.
- [98] R. S. Jeyendran, H. H. Vanderven, M. Perezpelaez, B. G. Crabo, and L. J. D. Zaneveld, "Development of an assay to assess the functional integrity of the human-sperm membrane and its relationship to other semen characteristics," *Journal of Reproduction and Fertility*, vol. 70, pp. 219-&, 1984.
- [99] S. Ved, M. Montag, A. Schmutzler, G. Prietl, G. Haidl, et al., "Pregnancy following intracytoplasmic sperm injection of immotile spermatozoa selected by the hypo-osmotic swelling-test: a case report," *Andrologia*, vol. 29, pp. 241-242, 1997.
- [100] A. S. Liu, R. Jones, L. Liao, D. Samara-Rubio, D. Rubin, et al., "A high-speed silicon optical modulator based on a metal-oxide-semiconductor capacitor," *Nature*, vol. 427, pp. 615-618, 2004.
- [101] Y. A. Vlasov and S. J. McNab, "Losses in single-mode silicon-on-insulator strip waveguides and bends," *Optics Express*, vol. 12, pp. 1622-1631, 2004.
- [102] O. Boyraz and B. Jalali, "Demonstration of a silicon Raman laser," *Optics Express*, vol. 12, pp. 5269-5273, 2004.
- [103] H. S. Rong, R. Jones, A. S. Liu, O. Cohen, D. Hak, et al., "A continuous-wave Raman silicon laser," *Nature*, vol. 433, pp. 725-728, 2005.
- [104] G. Balakrishnan, A. Jallipalli, P. Rotella, S. H. Huang, A. Khoshakhlagh, et al., "Room-temperature optically pumped (Al)GaSb vertical-cavity surface-emitting laser monolithically grown on an Si(100) substrate," *IEEE Journal of Selected Topics in Quantum Electronics*, vol. 12, pp. 1636-1641, 2006.
- [105] D. Pasquariello and K. Hjort, "Plasma-assisted InP-to-Si low temperature wafer bonding," *IEEE Journal of Selected Topics in Quantum Electronics*, vol. 8, pp. 118-131, 2002.

- [106] G. Roelkens, J. Brouckaert, D. Van Thourhout, R. Baets, R. Notzel, et al., "Adhesive bonding of InP/InGaAsP dies to processed silicon-on-insulator wafers using DVS-bis-benzocyclobutene," *Journal of the Electrochemical Society*, vol. 153, pp. G1015-G1019, 2006.
- [107] A. W. Fang, H. Park, O. Cohen, R. Jones, M. J. Paniccia, et al., "Electrically pumped hybrid AlGaInAs-silicon evanescent laser," *Optics Express*, vol. 14, pp. 9203-9210, 2006.
- [108] J. Van Campenhout, P. Rojo-Romeo, P. Regreny, C. Seassal, D. Van Thourhout, et al., "Electrically pumped InP-based microdisk lasers integrated with a nanophotonic silicon-on-insulator waveguide circuit," *Optics Express*, vol. 15, pp. 6744-6749, 2007.
- [109] H. T. Hattori, C. Seassal, E. Touraille, P. Rojo-Romeo, X. Letartre, et al., "Heterogeneous integration of microdisk lasers on silicon strip waveguides for optical interconnects," *IEEE Photonics Technology Letters*, vol. 18, pp. 223-225, 2006.
- [110] M. Fujita, A. Sakai, and T. Baba, "Ultrasmall and ultralow threshold GaInAsP-InP microdisk injection lasers: Design, fabrication, lasing characteristics, and spontaneous emission factor," *IEEE Journal of Selected Topics in Quantum Electronics*, vol. 5, pp. 673-681, 1999.
- [111] D. J. Sirbuly, M. Law, P. Pauzauskie, H. Q. Yan, A. V. Maslov, et al., "Optical routing and sensing with nanowire assemblies," *Proceedings of the National Academy of Sciences of the United States of America*, vol. 102, pp. 7800-7805, 2005.
- [112] H. W. Seo, C. S. Han, S. O. Hwang, and J. Park, "Dielectrophoretic assembly and characterization of individually suspended Ag, GaN, SnO₂ and Ga₂O₃ nanowires," *Nanotechnology*, vol. 17, pp. 3388-3393, 2006.
- [113] K. Q. Peng, Y. J. Yan, S. P. Gao, and J. Zhu, "Synthesis of large-area silicon nanowire arrays via self-assembling nanoelectrochemistry," *Advanced Materials*, vol. 14, pp. 1164-1167, 2002.
- [114] Y. Huang, X. F. Duan, and C. M. Lieber, "Nanowires for integrated multicolor nanophotonics," *Small*, vol. 1, pp. 142-147, 2005.
- [115] S. P. Anthony, J. I. Lee, and J. K. Kim, "Tuning optical band gap of vertically aligned ZnO nanowire arrays grown by homoepitaxial electrodeposition," *Applied Physics Letters*, vol. 90, p. 3, 2007.
- [116] T. Kuykendall, P. Ulrich, S. Aloni, and P. Yang, "Complete composition tunability of InGaN nanowires using a combinatorial approach," *Nature Materials*, vol. 6, pp. 951-956, 2007.

- [117] J. Kruger, K. Singh, A. O'Neill, C. Jackson, A. Morrison, et al., "Development of a microfluidic device for fluorescence activated cell sorting," *Journal of Micromechanics and Microengineering*, vol. 12, pp. 486-494, 2002.
- [118] N. L. Jeon, H. Baskaran, S. K. W. Dertinger, G. M. Whitesides, L. Van de Water, et al., "Neutrophil chemotaxis in linear and complex gradients of interleukin-8 formed in a microfabricated device," *Nature Biotechnology*, vol. 20, pp. 826-830, 2002.
- [119] T. Thorsen, S. J. Maerkl, and S. R. Quake, "Microfluidic large-scale integration," *Science*, vol. 298, pp. 580-584, 2002.
- [120] B. G. Chung, L. A. Flanagan, S. W. Rhee, P. H. Schwartz, A. P. Lee, et al., "Human neural stem cell growth and differentiation in a gradient-generating microfluidic device," *Lab on a Chip*, vol. 5, pp. 401-406, 2005.
- [121] J. Melin and S. R. Quake, "Microfluidic large-scale integration: The evolution of design rules for biological automation," *Annual Review of Biophysics and Biomolecular Structure*, vol. 36, pp. 213-231, 2007.
- [122] S. Y. Teh, R. Lin, L. H. Hung, and A. P. Lee, "Droplet microfluidics," *Lab on a Chip*, vol. 8, pp. 198-220, 2008.
- [123] S. Pennathur, C. D. Meinhart, and H. T. Soh, "How to exploit the features of microfluidics technology," *Lab on a Chip*, vol. 8, pp. 20-22, 2008.
- [124] S. K. Cho, H. J. Moon, and C. J. Kim, "Creating, transporting, cutting, and merging liquid droplets by electrowetting-based actuation for digital microfluidic circuits," *Journal of Microelectromechanical Systems*, vol. 12, pp. 70-80, 2003.
- [125] V. Srinivasan, V. K. Pamula, and R. B. Fair, "An integrated digital microfluidic lab-on-a-chip for clinical diagnostics on human physiological fluids," *Lab on a Chip*, vol. 4, pp. 310-315, 2004.
- [126] T. B. Jones, "On the relationship of dielectrophoresis and electrowetting," *Langmuir*, vol. 18, pp. 4437-4443, 2002.
- [127] T. B. Jones, K. L. Wang, and D. J. Yao, "Frequency-dependent electromechanics of aqueous liquids: Electrowetting and dielectrophoresis," *Langmuir*, vol. 20, pp. 2813-2818, 2004.
- [128] M. G. Pollack, R. B. Fair, and A. D. Shenderov, "Electrowetting-based actuation of liquid droplets for microfluidic applications," *Applied Physics Letters*, vol. 77, pp. 1725-1726, 2000.

- [129] J. Lee, H. Moon, J. Fowler, T. Schoellhammer, and C. J. Kim, "Electrowetting and electrowetting-on-dielectric for microscale liquid handling," *Sensors and Actuators A-Physical*, vol. 95, pp. 259-268, 2002.
- [130] S. K. Cho, Y. J. Zhao, and C. J. Kim, "Concentration and binary separation of micro particles for droplet-based digital microfluidics," *Lab on a Chip*, vol. 7, pp. 490-498, 2007.
- [131] Y. J. Zhao, U. C. Yi, and S. K. Cho, "Microparticle concentration and separation by traveling-wave dielectrophoresis (twDEP) for digital microfluidics," *Journal of Microelectromechanical Systems*, vol. 16, pp. 1472-1481, 2007.
- [132] G. J. Shah, E. Pierstorff, H. Dean, and K. Chang-Jin, "Meniscus-assisted magnetic bead trapping on EWOD-based digital microfluidics for specific protein localization," in *TRANSDUCERS '07 & Eurosensors XXI 2007: 14th International Conference on Solid-State Sensors, Actuators and Microsystems.*, Lyon, France, 2007.
- [133] Y. Wang, Y. Zhao, and S. K. Cho, "Efficient in-droplet separation of magnetic particles for digital microfluidics," *Journal of Micromechanics and Microengineering*, vol. 17, pp. 2148-2156, 2007.
- [134] H. Moon, A. R. Wheeler, R. L. Garrell, J. A. Loo, and C. J. Kim, "An integrated digital microfluidic chip for multiplexed proteomic sample preparation and analysis by MALDI-MS," *Lab on a Chip*, vol. 6, pp. 1213-1219, 2006.
- [135] R. B. Fair, A. Khlystov, T. D. Taylor, V. Ivanov, R. D. Evans, et al., "Chemical and biological applications of digital-microfluidic devices," *IEEE Design & Test of Computers*, vol. 24, pp. 10-24, 2007.
- [136] D. Chatterjee, B. Hetayothin, A. R. Wheeler, D. J. King, and R. L. Garrell, "Droplet-based microfluidics with nonaqueous solvents and solutions," *Lab on a Chip*, vol. 6, pp. 199-206, 2006.
- [137] I. Barbulovic-Nad, H. Yang, P. S. Park, and A. R. Wheeler, "Digital microfluidics for cell-based assays," *Lab on a Chip*, vol. 8, pp. 519-526, 2008.
- [138] T. K. Jun and C. J. Kim, "Valveless pumping using traversing vapor bubbles in microchannels," *Journal of Applied Physics*, vol. 83, pp. 5658-5664, 1998.
- [139] S. Z. Hua, F. Sachs, D. X. Yang, and H. D. Chopra, "Microfluidic actuation using electrochemically generated bubbles," *Analytical Chemistry*, vol. 74, pp. 6392-6396, 2002.
- [140] P. Garstecki, M. J. Fuerstman, M. A. Fischbach, S. K. Sia, and G. M. Whitesides, "Mixing with bubbles: a practical technology for use with portable microfluidic devices," *Lab on a Chip*, vol. 6, pp. 207-212, 2006.

- [141] T. Sakata, H. Togo, M. Makihara, F. Shimokawa, and K. Kaneko, "Improvement of switching time in a thermocapillarity optical switch," *Journal of Lightwave Technology*, vol. 19, pp. 1023-7, 2001.
- [142] M. Prakash and N. Gershenfeld, "Microfluidic Bubble Logic," *Science*, vol. 315, pp. 832-835, 2007.
- [143] J. A. Schwartz, J. V. Vykoukal, and P. R. C. Gascoyne, "Droplet-based chemistry on a programmable micro-chip," *Lab on a Chip*, vol. 4, pp. 11-17, 2004.
- [144] J. Lee and C. J. Kim, "Surface-tension-driven microactuation based on continuous electrowetting," *Journal of Microelectromechanical Systems*, vol. 9, pp. 171-180, 2000.
- [145] M. G. Pollack, A. D. Shenderov, and R. B. Fair, "Electrowetting-based actuation of droplets for integrated microfluidics," *Lab on a Chip*, vol. 2, pp. 96-101, 2002.
- [146] P. Y. Chiou, H. Moon, H. Toshiyoshi, C. J. Kim, and M. C. Wu, "Light actuation of liquid by optoelectrowetting," *Sensors and Actuators A-Physical*, vol. 104, pp. 222-228, 2003.
- [147] G. L. Liu, J. Kim, Y. Lu, and L. P. Lee, "Optofluidic control using photothermal nanoparticles," *Nature Materials*, vol. 5, pp. 27-32, 2006.
- [148] N. O. Young, J. S. Goldstein, and M. J. Block, "The motion of bubbles in a vertical temperature gradient," *Journal of Fluid Mechanics*, vol. 6, pp. 350-356, 1959.
- [149] B. A. Bezuglyi and N. A. Ivanova, "Creation, transportation, and coalescence of liquid drops by means of a light beam," *Fluid Dynamics*, vol. 41, pp. 278-285, 2006.
- [150] A. A. Darhuber, J. P. Valentino, J. M. Davis, S. M. Troian, and S. Wagner, "Microfluidic actuation by modulation of surface stresses," *Applied Physics Letters*, vol. 82, pp. 657-659, 2003.
- [151] R. H. Farahi, A. Passian, T. L. Ferrell, and T. Thundat, "Microfluidic manipulation via Marangoni forces," *Applied Physics Letters*, vol. 85, pp. 4237-4239, 2004.
- [152] K. T. Kotz, K. A. Noble, and G. W. Faris, "Optical microfluidics," *Applied Physics Letters*, vol. 85, pp. 2658-2660, 2004.
- [153] D. E. Kataoka and S. M. Troian, "Patterning liquid flow on the microscopic scale," *Nature*, vol. 402, pp. 794-797, 1999.

- [154] N. Garnier, R. O. Grigoriev, and M. F. Schatz, "Optical manipulation of microscale fluid flow," *Physical Review Letters*, vol. 91, 2003.
- [155] N. A. Ivanova and B. A. Bezuglyi, "Optical thermocapillary bubble trap," *Technical Physics Letters*, vol. 32, pp. 854-856, 2006.
- [156] R. H. Farahi, A. Passian, T. L. Ferrell, and T. Thundat, "Marangoni forces created by surface plasmon decay," *Optics Letters*, vol. 30, pp. 616-618, 2005.
- [157] R. H. Farahi, A. Passian, S. Zahrai, A. L. Lereu, T. L. Ferrell, et al., "Microscale Marangoni actuation: All-optical and all-electrical methods," *Ultramicroscopy*, vol. 106, pp. 815-821, 2006.
- [158] A. L. Lereu, A. Passian, R. H. Farahi, S. Zahrai, and T. Thundat, "Plasmonic Marangoni Forces," *Journal of the European Optical Society - Rapid Publications*, vol. 1, p. 06030, 2006.
- [159] A. Passian, S. Zahrai, A. L. Lereu, R. H. Farahi, T. L. Ferrell, et al., "Nonradiative surface plasmon assisted microscale Marangoni forces," *Physical Review E*, vol. 73, 2006.
- [160] A. T. Ohta, A. Jamshidi, J. K. Valley, H.-Y. Hsu, and M. C. Wu, "Optically actuated thermocapillary movement of gas bubbles on an absorbing substrate," *Applied Physics Letters*, vol. 91, pp. 074103-3, 2007.
- [161] E. Lajeunesse and G. M. Homsy, "Thermocapillary migration of long bubbles in polygonal tubes. II. Experiments," *Physics of Fluids*, vol. 15, pp. 308-314, 2003.